HILIGT, Upper Limit Servers II - Implementing the data servers

Ole König[a], Richard D. Saxton[b], Peter Kretschmar[c], Lorella Angelini[d], Guillaume Belanger[c], Phil A. Evans[e],
Michael J. Freyberg[f], Volodymyr Savchenko[g], Iris Traulsen[h], Jörn Wilms[a]

[a]*Dr. Karl-Remeis-Sternwarte and Erlangen Centre for Astroparticle Physics, Friedrich-Alexander-Universität Erlangen-Nürnberg, Sternwartstr. 7, 96049 Bamberg, Germany*
[b]*Telespazio-Vega UK for the European Space Agency (ESA), XMM-Newton SOC, European Space Astronomy Centre (ESAC), Camino Bajo del Castillo s/n, 28692 Villanueva de la Cañada, Madrid, Spain*
[c]*European Space Agency (ESA), European Space Astronomy Centre (ESAC), Camino Bajo del Castillo s/n, 28692 Villanueva de la Cañada, Madrid, Spain*
[d]*NASA, Goddard Space Flight Center, Greenbelt, Maryland, United States*
[e]*School of Physics and Astronomy, University of Leicester, Leicester, LE1 7RH, UK*
[f]*Max-Planck-Institut für extraterrestrische Physik, Giessenbachstraße, 85748 Garching, Germany*
[g]*ISDC, Department of Astronomy, University of Geneva, Chemin d'Écogia 16, 1290 Versoix, Switzerland*
[h]*Leibniz-Institut für Astrophysik Potsdam (AIP), An der Sternwarte 16, 14482 Potsdam, Germany*

Abstract

The *High-Energy Lightcurve Generator* (HILIGT) is a new web-based[*] tool which allows the user to generate long-term lightcurves of X-ray sources. It provides historical data and calculates upper limits from image data in real-time. HILIGT utilizes data from twelve satellites, both modern missions such as *XMM-Newton* and *Swift*, and earlier facilities such as *ROSAT*, *EXOSAT*, *Einstein* or *Ariel V*. Together, this enables the user to query 50 years of X-ray data and, for instance, study outburst behavior of transient sources. In this paper we focus on the individual back-end servers for each satellite, detailing the software layout, database design, catalog calls, and image footprints. We compile all relevant calibration information of these missions and provide an in-depth summary of the details of X-ray astronomical instrumentation and data.

Keywords: Catalogs, Surveys, X-rays: general, Instrumentation: detectors, Upper limit, Aperture photometry

1. Introduction

X-ray sources can be extremely variable on times scales of fractions of a second (for instance during quasi-periodic oscillations in black hole binaries, see, e.g., Strohmayer 2001, or millisecond neutron star pulsations, see, e.g, Hartman et al. 2008) to decades (e.g., Lin et al., 2017), with the flux sometimes ranging over several orders of magnitude (for instance during thermonuclear X-ray bursts of neutron stars, see, e.g., Grindlay et al. 1976 or Kuulkers et al. 2009). Some sources, like pulsars with a Be companion star (e.g., EXO 2030+375, see Wilson et al. 2002) exhibit regular outbursts, others, like tidal disruption events (e.g., Komossa and Bade, 1999) typically show one bright flare followed by a slow decay. The lifetime of a space-based observatory is very short compared to astrophysical timescales, and usually of the order of 5–10 years. In order to resolve variability patterns which are decades-long, it is therefore necessary to combine data of several instruments. With the increasing number of X-ray missions, however, it has become difficult to get a comprehensive overview of all available data. Furthermore, old data formats, missing analysis pipelines, and incomplete documentation make the extraction of data from many missions sometimes cumbersome. Due to these complexities and the time-consuming process of compiling flux data over multiple decades, detailed studies of source
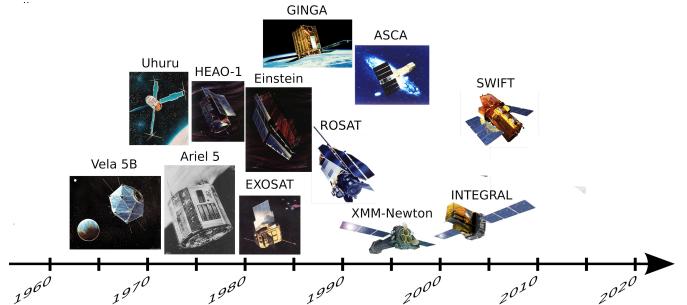

Figure 1: An overview of X-ray satellites implemented in HILIGT. The dates are approximately from the launch.

variability on these time scales are rare. Although there are services available that combine data of current and past missions (e.g., HEAVENS[1]), so far no generalized tool is available which automatically computes flux upper limits for multiple missions. For this reason, the *High-Energy Lightcurve Generator* (HILIGT) was developed. It is a web-based tool which enables quick access to the data of past and current X-ray missions, without the need to browse through several catalogs in person, or install software (see Saxton et al. 2021; hereafter Paper I, for an overview of the front-end).

Figure 1 compiles an overview of the X-ray satellites imple-

---

[*]http://xmmuls.esac.esa.int/hiligt/
Email address: ole.koenig@fau.de (Ole König)

[1]http://astroh.unige.ch/heavens/

mented in HILIGT, which span a time period of over 50 years. In order to fully exploit all the available data from these satellites, HILIGT provides a framework which either returns a catalog flux or calculates a flux upper limit at any celestial position. Adding upper limits to the lightcurve augments its diagnostic capability, for instance, in studying long-term flux variation of sources. In quiescent states (e.g., Menou et al. 1999), sources are often observed serendipitously, and upper limits provide the possibility to constrain their flux in these periods. A tool like HILIGT is especially important for sources typically studied in the X-rays, because they often show dramatic changes in luminosity (see, e.g., Remillard and McClintock 2006).

Therefore, a further major application is research into outbursts and state changes of transient sources (see, e.g., Belloni et al. 2011 or Hasinger and van der Klis 1989), as performed for instance in recent nova studies (Sokolovsky et al., 2021), or the ongoing *eROSITA* all-sky survey (e.g., Gokus et al. 2020 or Malyali et al. 2020). As it can be used to easily query the history of a source in the X-rays, HILIGT also bridges a connection to other multi-wavelength efforts such as ASSA-SN[2], which often observe new transient phenomena.

In Paper I we give an overview of the design of HILIGT and the details of the front-end clients. In this paper we concentrate on the back-end. Section 2.1 describes the upper limit calculation and Sect. 2.2 shows how HILIGT performs the count rate to flux conversion. Catalog calls are described in Sect. 2.4, followed by the footprint computation and database implementation (Sect. 2.5). Individual mission servers are described in Sect. 3. An overview of all mission parameters can be found in Table 1. We summarize and outline future plans in Sect. 4.

2. Design

In order to achieve the goal of providing flux upper limits and catalog values of multiple missions we

- download the available data (images, lightcurves, exposure and background maps) and store the image footprints in databases,

- design a framework which queries existing catalogs and matches them against the locally stored data,

- write a tool which calculates upper limits from image data,

- provide a set of spectral models and output energy bands to perform the count rate to flux conversion, and

- design a web interface for the end user.

We describe the top level design and server interaction of HILIGT in Paper I. Briefly, a user provides a set of celestial coordinates and a spectral model appropriate to the source's spectral shape. For each mission, a local database query finds all images in which the coordinates match the image footprint. In other words, the query finds all images which contain data at
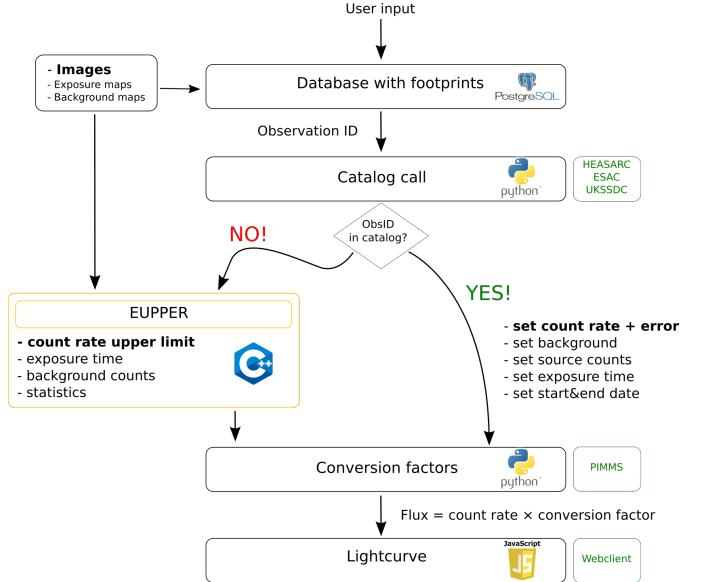
Figure 2: Basic scheme of HILIGT: The lightcurves exhibit data from catalogs in combination with upper limits, which are computed from the images.

the input position and then returns a list with the corresponding observation IDs. This list of observation IDs is reconciled with the existing catalogs: If the observation ID in the database contains a source corresponding to the input location, the count rate of that source from the mission catalog is returned. Otherwise, the image is used to compute a count rate upper limit (taking exposure, background, vignetting effects, and the point spread function into account). Finally, a conversion factor dependent on the input spectral model is used to convert the count rate into a flux. These data can be either queried from a web-interface in the browser, or using a URL query from the command line. A scheme of how HILIGT functions can be seen in Fig. 2. We refer to Paper I for the details of the front-end implementation, run-time, and a sample of possible scientific uses.

2.1. Calculation of upper limits

In the following we describe how HILIGT uses the tool "EUPPER" to calculate upper limits according to Kraft et al. (1991). Although the tool is part of the *XMM-Newton* SAS (Gabriel et al., 2004, available since SAS 16), it is designed to be mission-independent. Firstly, one needs to define an appropriate source region for the extraction of counts. Let N be the total number of counts in this source region A_S. A_S is assumed to be circular and depends on the point spread function (PSF), angular resolution and pointing accuracy of the mission.

In order to obtain the source counts S=N-B, the background counts B in background area A_B of a given position on the sky is needed. Ideally, this is done by analyzing a background map, whereby the counts of the background map in the source area ($A_B = A_S$) are summed up. If no background map is available the background counts are taken from an annulus of radius $2.5r$ and $3r$ around the source position. r is a mission-dependent source radius defined from the size of the PSF (see Table 1), such that the PSF does not overlap with the annulus.

The background counts are scaled to the source area by multiplying with the area ratio A_S/A_B. We note that this simplistic background estimation can cause errors if positions close to bright sources or at the edge of an image are evaluated. Upper limits in crowded fields or for extended sources can thus be estimated too low due to the high background counts. However, we emphasize that the annulus background estimation is only applied in the case where no background maps are available (only for *Einstein*, *EXOSAT*, and *ROSAT* PSPC, see also "bkg" column in Table 1).

To calculate the count rate, one has to divide the background subtracted counts by the exposure time. The exposure is taken from the exposure map at the specified position (which includes also the vignetting). If no exposure map is available, the exposure is taken from the header of the Flexible Image Transport System (FITS, Wells et al. 1981) image and multiplied by an off-axis dependent vignetting correction factor. In order to correct the count rate for the PSF, one also has to divide the source counts by the encircled energy fraction (EEF), given by the radius-integrated PSF normalized to the full PSF:

$$\text{EEF}(E, r, \theta) = \int_0^r \text{PSF}(E, r, \theta)\, dr \left/ \int_0^\infty \text{PSF}(E, r, \theta)\, dr \right. \quad (1)$$

HILIGT takes into account that the EEF changes as a function of source radius and off-axis angle θ, but does not account for the energy dependence of the PSF. The background subtracted count rate is therefore computed by

$$\text{CR} = \frac{N - B \cdot A_S/A_B}{\text{EEF} \cdot \text{exposure}} \quad . \quad (2)$$

The error propagation and thus the final upper limit depends on the number of counts. Gehrels (1986) shows that the application of classical Gaussian statistics is unsuitable in the case of low counts and Poisson or, best, Bayesian statistics (e.g., Kraft et al., 1991) must be used. Because such estimates are computationally more demanding, and the distribution asymptotically becomes Gaussian, we set a threshold of 80 counts to divide the two regimes.

For N>80 classical Gaussian statistics are applied and the uncertainty is computed by

$$\text{Upper limit (cts sec}^{-1}) = \frac{max(S,\ 0) + f \cdot \sqrt{N + B}}{\text{EEF} \cdot \text{exposure}} \quad (3)$$

with $\sigma_S = \sqrt{N + B}$ being the standard deviation estimated from the source counts based on Poisson statistics. These are obtained by linear Gaussian error propagation under the assumption of a Poissonian distribution on N and B. The factor f can be 1, 2, or 3 depending on the desired 1, 2 or 3-σ confidence level for a single parameter of interest (68.2%, 95.5% or 99.7%). In the case of low counts, Bayesian statistics are applied. We refer to Kraft et al. (1991) for a description of the relevant statistics.

We want to stress that EUPPER calculates upper limits (i.e., single-sided confidence limits) in most cases. Only if the value is ≥ 2 times the error it returns a data point (i.e., a two-sided

confidence limit). At this stage, HILIGT has computed count rates from the images, exposure and background maps. However, count rates cannot be directly compared between instruments. Therefore, HILIGT converts the count rate into a flux by multiplying it by an instrument- and model-specific conversion factor, as described in the next section.

2.2. Count rate to flux conversion

Photon counting detectors, such as CCDs, have counts as fundamental measurement property. In the linear regime, which is valid for low count rates, the number of source counts, S, in detector channel h within the exposure T is given by

$$S(h) = T \int_0^\infty \text{RMF}(h, E) \cdot \text{ARF}(E) \cdot F(E)\, dE \quad , \quad (4)$$

where $\text{ARF}(E)$ describes the effective area of the optics, including the detector efficiency. The detector response $\text{RMF}(h, E)$, often called the response matrix, gives the probability of detecting a photon of energy E in channel h. More details can be found, for instance, in Arnaud et al. (2011). The physically important parameter in Eq. 4 is the flux $F(E)$ of the observed source. This quantity is, however, difficult to obtain because generally Eq. 4 cannot be inverted (e.g., Lampton et al., 1976). In spectral analyses one therefore uses some kind of a forward folding process to estimate the predicted counts for a given spectral model, and then minimizes the deviation between the model predicted counts and the data using an appropriate statistical model (e.g., χ^2-statistic).

Extracting spectra and model based fitting of the data for each observation is beyond the scope of this tool. Therefore, the user selects a spectral model and HILIGT produces the flux *under the assumption* of this model. The currently available models are a power-law with photon index $\Gamma = 0.5, 1.0, 1.5, 1.7, 2.0, 2.5, 3.0,$ or 3.5, or a black body with temperature $kT = 60, 100, 300,$ or $1000\,\text{eV}$, respectively, and equivalent hydrogen column densities of $N_H = (1, 3, 10) \times 10^{20}\,\text{cm}^{-2}$. We use the PIMMS software (Mukai, 1993, version 4.11a), which solves Eq. 4 and calculates the count rate to flux conversion factors. We extract conversion factors for each filter, spectral model, and spectral index/temperature configuration (for efficiency reasons the conversion factors are hard-coded into the HILIGT code). They can be found in Table A.3 of the appendix.

The data of the different satellites can only be compared if they are given for the same flux range. Therefore, we interpolate (or extrapolate if the mission band is slightly smaller than our reference band) the energy bands of the different satellites onto three predefined energy bands. These reference bands are called *soft* for 0.2–2.0 keV, *hard* for 2.0–12.0 keV, and *total* for 0.2–12.0 keV.

It must be noted that an accurate selection of the spectral shape is of crucial importance for the correct flux determination. As an example we show the effect of a wrongly modeled spectrum for the blazar PKS 0537−286, which is known for having a hard power-law spectrum. Using *XMM-Newton* data, Reeves et al. (2001) determine a 0.2–10 keV flux

of $3.1 \times 10^{-12} \, \mathrm{erg \, cm^{-2} s^{-1}}$, assuming Galactic foreground absorption and $\Gamma = 1.3$. If we use HILIGT to reconstruct the flux for this pointed *XMM-Newton* observation[3], we obtain $(3.262 \pm 0.021) \times 10^{-12} \, \mathrm{erg \, cm^{-2} s^{-1}}$ in the 0.2–12 keV band. Given the slightly broader energy band, this is in line with the value determined by Reeves et al. (2001). Contrarily, using a very soft spectral model of $\Gamma = 3.5$ yields a flux of $(1.092 \pm 0.007) \times 10^{-12} \, \mathrm{erg \, cm^{-2} s^{-1}}$, a factor 3 off the correct flux value.

2.3. Reliability of upper limits

We address the problem of nearby bright sources by choosing the source radius according to the PSF. However, an upper limit close to a bright source (where the source region intersects with the wings of the PSF of the bright nearby source) can be estimated too high, and can possibly even cause false detections. Also straylight can result in biased upper limits. The number of bright sources is, however, relatively small, and we estimate that source confusion is relatively unlikely for the majority of observations (see Sect. 3.10.1). Furthermore, we note that for crowded fields or fields with extended emission the upper limits can be biased. This is less of a problem for older missions where the source density is lower due to lower sensitivity. We do not make an attempt to correct for bright pixels or columns and rely on the calibration data with which the images were created. Finally, we note that also chip gaps (e.g., *XMM-Newton*) or telescope features (e.g., *ROSAT* PSPC) can cause errors in the upper limit computation.

2.4. Catalog calls

In order to complement the upper limits with archival data, HILIGT performs cone searches around the specified coordinates in the available mission catalogs. If an entry is found, the catalog data is provided and no upper limit calculation is performed. This can be changed by setting a flag to ignore all catalog data. NASA's *Goddard Space Flight Center* provides most catalogs and for most missions, HILIGT uses the High Energy Astrophysics Science Archive Research Center (HEASARC) to access the data[4]. The ESA mission *XMM-Newton* is accessed via a Table Access Protocol (TAP) to the *XMM-Newton* Science Archive (Loiseau et al., 2017). *Swift* is accessed through a custom-built HTTPS interface to the 2SXPS upper limit server (Evans et al., 2020). We note that the back-end calls these servers on-the-fly, which implies issues with HILIGT in case of malfunction. The search radii for the different missions can be found in Sect. 3 and Table 1. The search radius is chosen based on the spatial resolution of the telescope and typically follows the recommendation by the HEASARC[5]. However, source confusion in the catalog is a problem in crowded fields and for old missions (large search radii), which can result in too high flux values close to bright sources.

2.5. Footprints and database implementation

Finally, we describe how HILIGT queries its databases to find the images, which match the source coordinates. The so-called footprint delineates the sky region where the image contains useful data and for which HILIGT is able to compute upper limits. HILIGT queries the database with the given world coordinates (right-ascension, declination for the epoch J2000) and looks for all images where the coordinates lie within the footprint shape. Unless a catalog count rate for this location is available, an upper limit is calculated. We note that the footprints of *XMM-Newton* slew, *XMM-Newton* stacked, *Einstein* HRI/IPC, *EXOSAT* LE, *ROSAT* HRI are computed with a custom-built algorithm (see König, 2019), however, the detailed information about the calculation can be found in the following Sect. 3.

HILIGT uses POSTGRESQL to handle the image meta data (mostly footprint shapes)[6]. In order to determine whether the input coordinates match the footprint, PGSPHERE is used[7]. It provides a fast search of spherical coordinates in a SQL database. HILIGT uses SPOLY for the representation of polygons and SCIRCLE for circular footprints. The database has the following fields:

- OBSID: The observation ID is used to link the images to the mission catalogs

- FILENAME: By using the file name the actual image can be found to parse its location to the EUPPER tool

- FOV: The polygon or circular information of the footprint in radians (for SPOLY/SCIRCLE)

- FILT/INSTRUME: If necessary, a filter or instrument column is appended, to apply the correct conversion factors (e.g. for *Einstein*)

Einstein, launched in 1978, and *EXOSAT*, launched in 1983, used the B1950 epoch (in FK4). For consistency, all footprints in HILIGT are computed in epoch J2000 (FK5). This means that a coordinate transformation (Astropy Collaboration et al., 2013) of the source position has to be done to analyze the actual B1950 FK4 images for the upper limit.

3. Description of the mission servers

In the following, we outline the implementation of each mission server.

3.1. Vela 5B (1969–1979)

Vela 5B's instruments (Whitlock et al., 1992a,b) had an energy range of 3–750 keV. We concentrate only on the scintillation X-ray detector (XC), which was an all-sky monitor and had an energy range of 3–12 keV. The collimator aperture was ~6° and the satellite had an orbital period of 56 hours. HEASARC

---

[3]ObsID 0114090101, $\Gamma = 1.5$, $N_H = 3 \times 10^{20} \, \mathrm{cm^{-2}}$

[4]https://heasarc.gsfc.nasa.gov/

[5]This value is shown above the observation table when searching for a source in the W3Browse interface and selecting the relevant catalog in the "Query Results" tab. The catalog sizes can be found at https://heasarc.gsfc.nasa.gov/cgi-bin/W3Browse/w3catindex.pl

[6]https://www.postgresql.org/

[7]https://pgsphere.github.io/

provides lightcurves of 99 sources[8], out of which 35 sources have 56 h binned lightcurves and 64 sources have 112 h binned lightcurves (see Whitlock et al. 1992b for more information about the deconvolution of crowded fields). We use a circular footprint of 30′ around the source position (converted from FK4 to FK5) to query the lightcurves. To convert count rates into fluxes, HILIGT uses the conversion factor from the COUFLU keyword, which is set to 4.5×10^{-10} erg cm^{-2}cnt^{-1} for a Crab-like spectrum in the 3–12 keV band. Because this conversion factor is applied to all sources regardless of their spectral shape, we add a systematic uncertainty of 1.5×10^{-10} erg cm^{-2}cnt^{-1}. To make the passband comparable to the other missions within HILIGT, we scale the 3–12 keV flux to 2–12 keV according to[9]

$$\mathrm{ConvFac_{HILIGT}} = \mathrm{ConvFac_{Mission\ band}} \cdot \frac{\mathrm{Flux_{HILIGT\ band}}}{\mathrm{Flux_{Mission\ band}}} \quad (5)$$

3.2. Uhuru (1970–1973)

Uhuru (Giacconi et al., 1971) was an all-sky survey mission which monitored the sky from 1970 December 12 until 1973 March 18. A total of 339 unique sources were identified and published in the Fourth Uhuru (Forman et al. 1978) catalog. HILIGT accesses the UHURU4 catalog[10] with a search radius of $1°$. HILIGT does not access the raw lightcurves but only to the time-averaged catalog data. The catalog count rate is transformed to a 2–6 keV flux using the conversion factor 1.7×10^{-11} erg cm^{-2}cnt^{-1}, given by Forman et al. (1978) for a Crab-like spectrum. A systematic uncertainty of 20% is added to the flux and the energy range extrapolated to 2–12 keV using Eq. 5. For transient and highly variable sources (see Table 5 and 8 of Forman et al. 1978) the count rate error field is not populated in the catalog. We adopt this approach and set the error to zero in these cases. The resulting error on the flux will then solely originate from the 20% flux conversion uncertainty.

3.3. Ariel V (1974–1980)

As *Uhuru*, *Ariel V* was an all-sky survey mission which scanned the sky for about 5.5 years with a spin period of $\sim$6 s. HILIGT provides the lightcurves of the All Sky Monitor (ASM, Holt 1976). In order to select the lightcurve corresponding to the query position, we define a circular footprint of 30′. The


Figure 3: The historical 1975 outburst of 1A 0535+262 covered by the all-sky monitors on *Vela 5B* and *Ariel V* (Rosenberg et al., 1975).

files[11] provide flux data in units of photons cm^{-2} s^{-1} in the 3–6 keV range. As outlined in Kaluzienski (1977, p. 106, Table A.1) we first convert the photon flux to a *Uhuru* count rate and afterwards to "Uhuru Flux Units" (UFU):

$$\textit{Ariel V}\ (3\text{–}6\,\mathrm{keV\ photons\ cm^{-2}\,s^{-1}}) = \kappa \cdot \mathrm{U}\ (\textit{Uhuru}\ \mathrm{cts\ sec^{-1}}), \quad (6)$$

where 1 *Uhuru* cts sec^{-1} equals 1.7×10^{-11} erg cm^{-2}s^{-1} in 2–6 keV. Kaluzienski (1977) state that a value of $\kappa = (1.5 \pm 0.5) \times 10^{-3}$ is reasonable for a relatively wide range of incident spectra. As for *Vela 5B* and *Uhuru* we estimate the 2–12 keV flux by Eq. 5, assuming a Crab-like spectrum. Figure 3 shows an example lightcurve of the 1975 outburst of 1A 0535+262 with *Vela 5B* and *Ariel V* all-sky monitor data combined.

In addition, HILIGT accesses the catalog of the Sky Survey Instrument (SSI, Villa et al. 1976) which were two pairs of two proportional counters (LE and HE). One LE detector failed shortly after launch. The ARIEL3A catalog[12] contains 109 X-ray sources at low Galactic latitudes ($|b| < 10°$, Warwick et al. 1981), and 142 sources at high Galactic latitudes (McHardy et al., 1981). HILIGT searches this catalog with a radius of $0.5°$. We assume a Crab-like conversion factor of $(5.3 \pm 0.8) \times 10^{-11}$ erg cm^{-2}cnt^{-1}, as outlined by Warwick et al. 1981, p. 880) and extrapolate the resulting 2–10 keV flux to HILIGT's *hard* band (2–12 keV) using Eq. 5.

3.4. HEAO-1 (1977-1979)

The payload of *HEAO-1* (Rothschild et al., 1979) consisted of four major instruments (A1–A4). HILIGT provides fluxes from the A1 catalog[13] (Wood et al., 1984), which we access with a $1°$ search radius. This catalog contains data of 842 sources from the first six months of the *HEAO-1* mission. We use a Crab-like conversion factor of 4.78×10^{-9} erg cm^{-2} cnt^{-1}

---

[8]https://heasarc.gsfc.nasa.gov/FTP/vela5b/data/

[9]The missions *Vela 5B*, *Uhuru*, *Ariel V* and *HEAO-1* are not included in PIMMS. For these missions, only conversion factors for a power-law spectrum in the missions energy band are available (ConvFac$_{\mathrm{Mission\ band}}$). Generally, this range is different from the HILIGT bands and the calculated flux cannot be directly compared. We therefore estimate a new conversion factor ConvFac$_{\mathrm{HILIGT}}$ for the HILIGT energy range through multiplying ConvFac$_{\mathrm{Mission\ band}}$ by the ratio of the fluxes in the two energy bands. This factor is hard-coded. The integrated energy flux in the HILIGT (Flux$_{\mathrm{HILIGT\ band}}$) and mission (Flux$_{\mathrm{Mission\ band}}$) band, respectively, is computed with the Interactive Spectral Interpretation System (Houck, 2002, ISIS version 1.6.2-47) with the model tbabs*powerlaw. We note that since we only have knowledge of this one conversion factor for each mission, the output spectral model will always be a power-law of fixed slope, indifferent of the user choice in HILIGT. To account for this uncertainty, we add a systematic error on the conversion factors.

[10]https://heasarc.gsfc.nasa.gov/W3Browse/uhuru/uhuru4.html

[11]https://heasarc.gsfc.nasa.gov/FTP/ariel5/asm/data/

[12]https://heasarc.gsfc.nasa.gov/W3Browse/ariel-v/ariel3a.html

[13]https://heasarc.gsfc.nasa.gov/W3Browse/heao1/a1.html

to convert the count rate to a 2–10 keV flux (Wood et al., 1984), and extrapolate to 2–12 keV using Eq. 5.

Furthermore, HILIGT gives access to data of the A2 experiment, which was divided into six proportional counters: two low energy detectors (LED, 0.15–3 keV), the medium energy detector (MED, 1.5–20 keV) and three high energy detectors (HED, 2.5–60 keV). MED and HED data is accessed through the the Piccinotti et al. (1982) catalog A2PIC, which contains 68 extra-galactic sources[14]. The data originates from two six month long scans and is confined to Galactic latitudes $|b| > 20°$, totaling 65.5% of the entire sky. The catalog also provides conversion factors depending on the spectral shape of the source. For sources without sufficient spectral information, the catalog assumes a 6 keV thermal Bremsstrahlung spectrum for clusters and a slope 1.65 powerlaw spectrum for AGN. For unidentified sources, an average conversion factor of $2.5 × 10^{-11}$ erg cm^{-2} cnt^{-1} is assumed. We extrapolate this to HILIGT's 2–12 keV *hard* band (Eq. 5). The catalog, which is queried with a 1° search radius, provides two count rates from the first and second scan, which we treat as two individual data points.

HEAO-1 surveyed over 95% of the sky to a sensitivity limit of $\sim 3 × 10^{-11}$ erg cm^{-2}s^{-1} in the 0.44–2.8 keV band. HILIGT utilizes the LED data through the A2LED catalog (Nugent et al., 1983), which contains 114 sources[15]. 32 of the 114 sources have a count rate of zero and HILIGT returns the count rate error as an upper limit in these cases. Conversion factors for a black body and powerlaw can be found in Nugent et al. (1983, Fig. 5-6). These are calculated for the "1 keV band" (0.44–2.8 keV). Again, HILIGT uses Eq. 5 to map this onto HILIGT's soft (0.2–2 keV) band. Due to the differences in energy bands of all three catalogs with respect to the HILIGT bands, a systematic uncertainty of 20% is added on the flux.

HEASARC does not provide a catalog with count rate data of the A3 experiment, which is therefore not accessed. The all-sky monitoring data of the A4 experiment in the 13–180 keV range (Levine et al., 1984) will be included in a future release of HILIGT.

3.5. Einstein (1978–1981)

A mission overview of *Einstein* is given by Giacconi et al. (1979) and the user manual can be found in D.E. Harris (1984). We concentrate on the Wolter Type I telescope with the Imaging Proportional Counter (IPC, Gorenstein et al. 1981; Harnden et al. 1984) and the High Resolution Imager (HRI, Henry et al. 1977). The data of both instruments are interpolated to HILIGT's *soft* band (0.2–2.0 keV).

3.5.1. High Resolution Imager (HRI)

The HRI was the first high-resolution X-ray camera on-board a spacecraft. It had a high spatial resolution of 3″ over the central 25′ of the focal plane, and even 2″ within 5′ of the optical axis axis. Two catalogs are available through HEASARC,

(a) LMXB 3U 1636−53 (Seq. No. 6769)

(b) 4U 0813−38 (Seq. No. 981)

(c) HMXB Cygnus X-1 (Seq. No. 3)

(d) M31 (Seq. No. 7066)
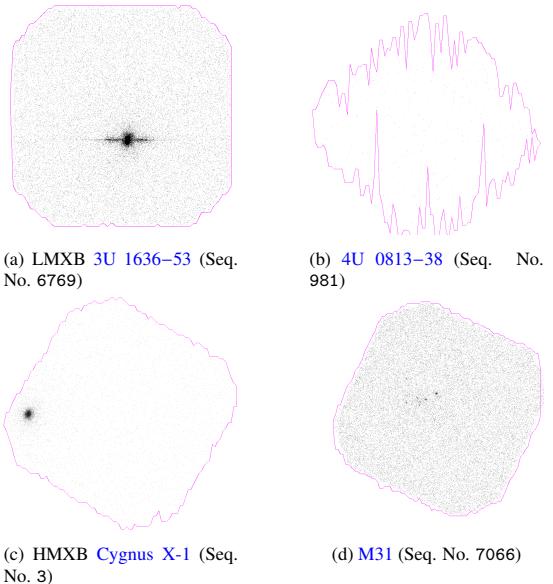
Figure 4: Example of the footprints calculated with our custom-built footprint algorithm for the *Einstein* HRI images.

HRIIMAGE [16] and HRICFA [17]. The count rates of the HRICFA catalog do not have a time stamp or exposure time but can be linked to the HRIIMAGE catalog, which provides this information, using the sequence number field. The sequence number is further used as key to link the catalog entries to the images of the database (where we usually use the observation ID, see Sect. 2). As there is no direct background information in the catalogs, HILIGT provides background counts from a constant background estimate of $5 × 10^{-3}$ cts sec^{-1}arcmin^{-2} (Giacconi et al., 1979) with a circular source radius of 3.98″ (D.E. Harris, 1984, Ch. 4, p. 10). The column `Net_Time` in HRIIMAGE is used as exposure time. Furthermore, we adopt the catalog search radii of 1′ for HRICFA, and 15′ for HRIIMAGE from the HEASARC.

In case no catalog entry is found for the requested position, we use 870 HRI images, produced by the Harvard Center for Astrophysics, to calculate upper limits. The images were taken with a 24′ FOV in the range 0.15–3.5 keV. The footprints are calculated with our custom-built algorithm (see an example in Fig. 4). About 5% of the images exhibit regions with low count rates, making an exact border distinction difficult and resulting in frayed footprints. Typically, this reduction in footprint area is acceptable (see Fig. 4b) and the image can be used for upper limit calculations. However, for 34 images the footprint becomes too distorted, or other file problems arise. These are excluded from the database, which contains a total of 836 footprints.

The PSF (D.E. Harris, 1984, Ch. 4, p. 10ff) can be approxi-

---

[14]https://heasarc.gsfc.nasa.gov/W3Browse/heao1/a2pic.html
[15]https://heasarc.gsfc.nasa.gov/W3Browse/heao1/a2led.html

[16]https://heasarc.gsfc.nasa.gov/W3Browse/einstein/hriimage.html
[17]https://heasarc.gsfc.nasa.gov/W3Browse/einstein/hricfa.html
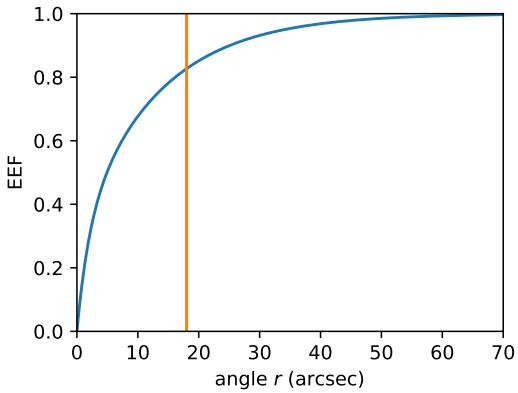
Figure 5: *Einstein* HRI encircled energy fraction, computed by integrating Eq. 7 using Eq. 1. The orange line shows the 18″ source radius.

mated by

$$
\begin{aligned}
\mathrm{PSF}(r) \;=\; & 2.885 \cdot 10^{-2} \cdot \exp\!\left(-\frac{r}{1.96''}\right) \\
& + 0.01 \cdot \exp\!\left(-\frac{r}{12.94''}\right) \mathrm{arcsec}^{-2}
\end{aligned}
\tag{7}
$$

This approximation is accurate for a 5′ circle around the field center (on-axis) at 1.5 keV and $r \leq 1'$. We were unable to find quantitative information about the off-axis behavior of the PSF outside of 5′. The source radius for upper limit calculations is set to 18″ (*Einstein*'s "standard circle"), corresponding to an EEF of 0.83 for this empirical model (see Fig. 5). No vignetting correction is available to our knowledge. This may overestimate upper limits at large off-axis angles because the vignetting effectively decreases the exposure time, which increases the count rate. Therefore the upper limits for sources detected at the edges may be too stringent.

3.5.2. Imaging Proportional Counter (IPC)

The IPC had lower 1′ spatial and spectral resolution than the HRI but a full focal plane coverage. Two identical IPC detectors (except for the entrance material) were mounted on *Einstein*. The background count rate was $\sim 10^{-2}$ cts sec^{-1} and the instruments sensitivity 1 cts sec^{-1} per 4×10^{-11} erg cm^{-2}s^{-1} (Giacconi et al., 1979).

There are two catalogs for the IPC containing 4132 images in the 0.2–3.5 keV range, IPCIMAGE [18] and IPC [19]. We use cone search radii of 2′ for the IPC catalog and 15′ for IPCIMAGE, respectively. To infer all necessary information, we merge these two catalogs by the sequence number in IPC and the object column in IPCIMAGE. We also use this sequence number as key to link the catalog entries to the images in the *Einstein* database. The following fields are queried from the IPCIMAGE catalog:

- `Object`: Same as sequence number in IPC (excluding the

(a) HMXB Cen X-3 (Seq. No. 817)

(b) 30 Dor, a cluster of stars in the LMC (Seq. No. 4559)

(c) M31 (Seq. No. 574)

(d) SNR MSH 14−63 (Seq. No. 2164)
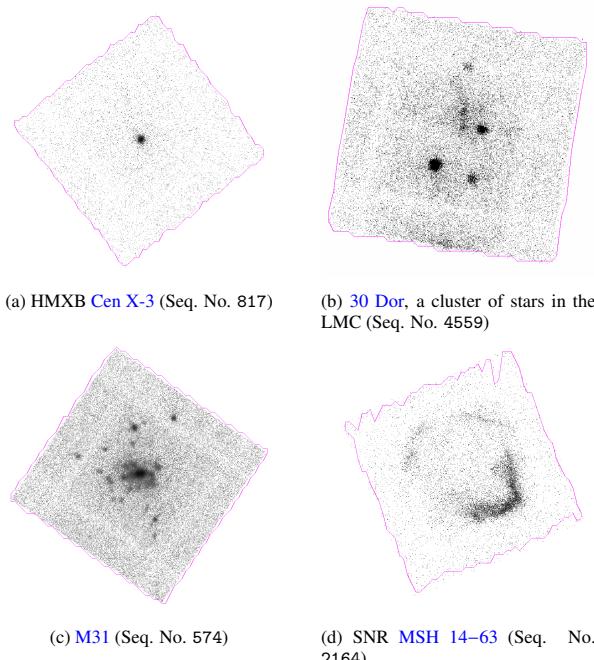
Figure 6: Example of *Einstein* IPC footprints.

first letter); links the entries to the IPC catalog and to the images in HILIGT's *Einstein* database

- `Live_Time`: Exposure time, equaling the keyword `TIME_LIV` in the images

- `Time` and `End_Time`: Start and end time of the observation

The IPC catalog gives the source and background count rates of the observations (Harris, 1990),

- `Sequence_Num`: A two to five digit number which uniquely identifies an *Einstein* observation, and which we use as link to the IPCIMAGE entry

- `Count_Rate` and `Count_Rate_Error`: Corrected count rate in the 0.2–3.5 keV band

- `Background_Count`: The total number of background counts in the 2.4′ × 2.4′ detection cell

The images available at the HEASARC have been smoothed with a $\sigma = 32''$ Gaussian and were background-subtracted, which makes the processing with EUPPER difficult because it works on uncorrected images. We therefore use the event files and create images with the SAOImageDS9 software (Joye and Mandel, 2003, Beta version 8.0rc4). Examples for the footprint calculated with our custom-built algorithm can be found in Fig. 6. In total the *Einstein* database contains 3923 footprints with the corresponding images.

The vignetting (see D.E. Harris 1984, Ch. 5, p. 18, and plotted in Fig. 7) as a function of off-axis angle θ (the difference between the optical axis and source position in arcmin) is

$$
\mathrm{Vign}(\theta \leq 12') = (-0.0003125 \cdot \theta - 0.00825) \cdot \theta + 0.997 \tag{8}
$$
$$
\mathrm{Vign}(\theta > 12') \quad\quad = 1.1049 - 0.02136 \cdot \theta \quad . \tag{9}
$$
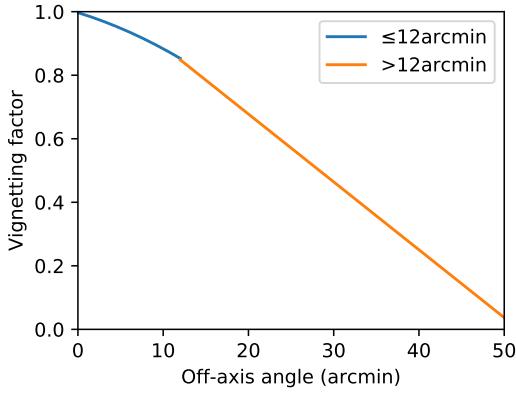
Figure 7: *Einstein* IPC vignetting function (Eq. 8–9).
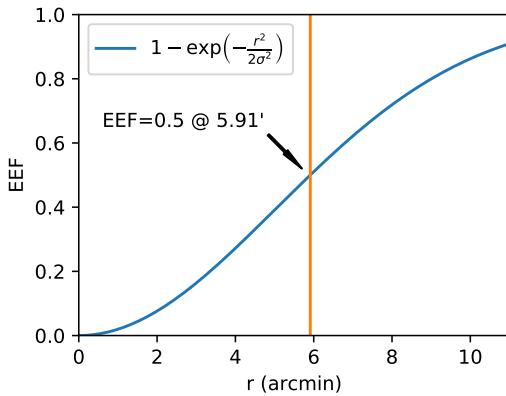
Figure 8: *Einstein* IPC EEF function (Eq. 10) with source radius at 5.91′.

Under the assumption of a circular Gaussian response with width σ, Harnden et al. (1984, p. 24) show that the fraction of total power enclosed within radius r (see Fig. 8) is given by

$$\mathrm{EEF}(r) = 1 - \exp\left(-\frac{1}{2}\frac{r^2}{\sigma^2}\right) \quad (10)$$

HILIGT uses a source radius of 5.911′, corresponding to an EEF of 0.5. This is a very large source radius, originating from the low 1′ spatial resolution of the IPC.

3.6. EXOSAT (1983–1986)

The payload of *EXOSAT* consisted of two low energy imaging telescopes (LE, de Korte et al. 1981), a medium energy proportional counter (ME, Turner et al. 1981) and a gas scintillation proportional counter (Peacock et al., 1981). A full mission overview is given by White and Peacock (1988). The *EXOSAT* LE instrument is of great importance for HILIGT, since it produced 3677 images which provide the possibility of upper limit estimates. Additionally, the *EXOSAT* ME slew and pointed catalogs are included in HILIGT.

3.6.1. EXOSAT LE

The Low Energy (LE) instrument consisted of two identical Wolter I telescopes with a focal length of 1.1 m. Each in-strument had a *channel multiplier array* (CMA1 and CMA2) assembled in the focal plane. The energy band of the instrument was determined by the effective area of the applied filter (see Fig. 4 of de Korte et al. 1981). Overall, the LE instrument had an energy range of ~0.05–2.0 keV. The CMA2 instrument failed on 1983-10-28, only five months into the three year mission. Therefore, most images were detected by CMA1. The CMA detectors were sensitive to UV radiation and bright O- and B-stars could contaminate the image quality. *EXOSAT* LE therefore used optical blocking filters. From the nine filters on the filter wheel (FW), the most attendant to the *EXOSAT* LE images used by HILIGT are: Polypropylene ("PPL" at FW Pos. 2), thick 400 nm Lexan ("4Lx" at FW Pos. 3), Aluminium-parylene ("Al/P" at FW Pos. 6), thin 300 nm Lexan ("3Lx" at FW Pos. 7), and a Boron ("Bor" at FW Pos. 8) filter. Usually, 3Lx, Bor and Al/P were used. By applying filter dependent conversion factors, HILIGT gives the flux in the *soft* 0.2–2 keV band.

HILIGT accesses the LE catalog[20] with a catalog search radius of 1′. The catalog gives the background in the field `background_per_sqpix` in units of cts pixel^{-2}. One pixel equals 4″ and the on-axis HEW of the PSF is 24″ (White and Peacock, 1988). Thus, we use a circular background region of area $\pi(12\,\mathrm{arcsec})^2$ and determine the background counts by

$$\texttt{bkg\_cts} = \texttt{background\_per\_sqpix} \cdot \pi(12\,{''})^2/(4\,{''})^2 \quad (11)$$

We download 3677 *EXOSAT* LE images from the HEASARC[21] and identify four different image shapes in the data set: CMA1 images with the 3Lx filter have a rectangular (~8%) shape, while the other CMA1 filters and CMA2 images have an octagonal (~92%) shape. The octagonal CMA1 and CMA2 images tend to have illuminated edges – likely due to stray light – with noise outside of the main shape. Some also exhibit extremely low count rates in the whole image. The latter makes an automatized footprint calculation with our footprint algorithm difficult. The footprint position on the detector plane, however, is constant for all octagonal images. Therefore, we define nine (eight for CMA2) fixed footprint points, specified in Table A.2. An example can be seen in Fig. 9a,b. The remaining rectangular images do not exhibit noise outside of the FOV, which makes them ideally suited for our footprint algorithm (Fig. 9c,d).

The observation ID is five letters long and occurs as `ORIGFILE` keyword in the FITS images. It is also contained in the filename (letter 5–9) and in the catalog as `File_Image` with an additional letter in front. Removing the letter allows us to generate a key that can be used to link the image to the corresponding catalog entry.

The point spread function of *EXOSAT* has 50% enclosed power (HEW) at 24″ on-axis, degrading to 4′ at 1° off-axis. Vignetting effects of the telescopes reduced the off-axis effective area to 45% of its peak value at 1° off-axis (White and Peacock, 1988, p. 11). In case the image is analyzed with EUPPER

(a) CMA1 PPL obs. of SNR Cas A (Obs. ID 01979)

(b) CMA2 3Lx obs. of HMXB Cyg X-3 (Obs. ID 02788)

(c) CMA1 3Lx obs. of the pulsar Her X-1 (Obs. ID 27503)

(d) CMA1 3Lx obs. of the CV VV Pup (Obs. ID 18315)

Figure 9: An example of *EXOSAT* LE images with the calculated footprints. Fig. (a) shows the most abundant (~81%) octagonal CMA1 footprint shape with nine defined footprint points. In Fig. (b) one can see an example of the CMA2 octagonal footprint shape (~11%) with eight defined points (see Table A.2). The illuminated edges are most likely stray light effects. Fig. (c–d) show the two remaining rectangular and smaller shapes of CMA1 3Lx, which were computed with our custom-built algorithm.

(i.e., no catalog entry available), HILIGT uses a source radius of 1′.

3.6.2. *EXOSAT ME*

The Medium Energy (ME) instrument of *EXOSAT* consisted of eight proportional counters, which took photometric data (lightcurves) in the 1–20 keV (Argon filled-gas cell) and 5–50 keV (Xenon filled) energy range. For more information about *EXOSAT* ME we refer to Turner et al. (1981) and Reynolds et al. (1999).

HILIGT accesses the ME catalog[22] for the pointed mission phase with a search radius of 45′. This catalog provides 2291 entries with start and end time, count rate in the 1–15 keV band, error, and exposure. The slew phase covered 98% of the sky and the EXMS catalog[23] contains 1210 detected sources (Reynolds et al., 1999). HILIGT accesses this catalog with a search radius of 60′. Next to the count rate (1–8 keV), error, and detection time, this catalog provides no processable information for HILIGT. Using PIMMS, we calculate two sets of conversion factors with an input range of 1–15 keV and 1–8 keV for the ME and EXMS catalogs, respectively. To compare the data to the other missions, both catalogs are mapped onto HILIGT's *hard* (2–12 keV) band.

3.7. *GINGA (1987-1991)*

GINGA (Makino and ASTRO-C Team, 1987) was the third Japanese X-ray mission and had a very large energy range from 1–500 keV. The main instrument was the Large Area Proportional Counter (LAC, 1.5–37 keV, Turner et al. 1989). *GINGA* LAC had no imaging capability, thus upper limit calculations from images is not possible in this case. However, we include the GINGALAC catalog[24]. The 1.5–37 keV range is interpolated to the *hard* band (2–12 keV). *GINGA* was in a low-earth orbit and regularly crossed Earth's radiation belts and a further background source is the diffuse cosmic X-ray background. Count rates of the catalog are background subtracted (see Hayashida et al., 1989). *GINGA*'s pointing stability was about 6′ (Turner et al., 1989) and we use a conservative 10′ as catalog search radius. The catalog contains 419 entries. We plan to include the ASM lightcurve data in a future HILIGT release.

3.8. *ROSAT (1990–1998)*

A position sensitive proportional counter (PSPC) and a High Resolution Imager (HRI) were located in the focal plane of *ROSAT* (Pfeffermann et al., 1987). A second telescope with a wide-field camera (Pounds et al., 1993), operating in the hard UV range (0.06–0.2 keV), is not included in HILIGT (also note that the UV instrument was very insensitive due to the Sun). Due to its long operational period, large sky coverage and high exposure times, *ROSAT* is a key mission for HILIGT, and we

---

[22]https://heasarc.gsfc.nasa.gov/W3Browse/exosat/me.html
[23]https://heasarc.gsfc.nasa.gov/W3Browse/exosat/exms.html
[24]https://heasarc.gsfc.nasa.gov/W3Browse/ginga/gingalac.html

include both images and available catalogs. For a mission overview we refer to the ROSAT User's Handbook by Briel et al. (1996).

3.8.1. Position Sensitive Proportional Counter (PSPC)

The PSPC consisted of multi-wire proportional counters and had modest energy and high spatial resolution (25″ at 1 keV) with a circular 2° diameter FOV. Two redundant units were assembled on a carousel, PSPC-B was used for the pointed phase while detector PSPC-C was used for the survey. Shadows of the wires in the detector could be suppressed by dithering, however, shadows originating from the mirror mount ("spider") remain in the images (see Fig. 10). We note that if the source or background position coincides with the spider, the resulting upper limit may be biased. We use a source radius of 100″ for the PSPC instrument and interpolate its 0.1–2.4 keV passband to HILIGT's *soft* band (0.2–2 keV). The same conversion factors are used for the RASS and pointed data.

3.8.2. PSPC Pointed

The second *ROSAT* source catalog of pointed observations (ROSPSPC/2RXP) contains 100 048 source detections with arcsecond positions from 17.3% of the sky, including 54 133 high confidence detections [25]. HILIGT accesses the ROSPSPC catalog[26] with a search radius of 30″. Furthermore, we use the 0.1–2.5 keV images[27] for the calculation of upper limits. As footprint we choose a circle of radius 0.95° around the center. Examples of the resulting footprint are shown in Fig. 10. In total, our *ROSAT* database contains 5490 footprints. Additionally, exposure and background maps are provided by the HEASARC. While the exposure maps are included into the upper limit calculation, the background maps are currently not included due to compatibility issues with the SAS.

We implement the radius and off-axis angle dependent encircled energy fraction according to (Zimmermann et al., 1998, Eq. 5.13). The 1 keV representation can be seen in Fig. 11. Note that the formula is energy dependent. This energy dependence is impossible to include into the HILIGT code because the information about photon energy is irretrievably lost in the image unless one has access to the corresponding event files. Therefore, we assume[28] a constant energy of 1 keV.

We infer the vignetting correction factor from table `vignet_pspc.fits` which is available at the Max-Planck Institute for Extraterrestrial Physics (MPE, see also Fig. 5.29 in Zimmermann et al. 1998). Due to the reasons outlined above, we only use the 1 keV values and obtain the vignetting correction function in Fig. 12.

---

[25]https://heasarc.gsfc.nasa.gov/mail_archive/rosnews/msg00131.html

[26]https://heasarc.gsfc.nasa.gov/W3Browse/rosat/rospspc.html

[27]https://heasarc.gsfc.nasa.gov/FTP/rosat/data/pspc/processed_data/

[28]This approximation has a large uncertainty of about 50% at low off-axis angles (Zimmermann et al., 1998, Fig. 5.17). The energy variation decreases at larger off-axis angles and is in the order of 5% at 30′ off-axis (Zimmermann et al., 1998, Fig. 5.18).

(a) Quasar 3C 273 (Obs. ID UK701265P.N1) (b) HMXB Vela X-1 (Obs. ID WG400313P.N1)
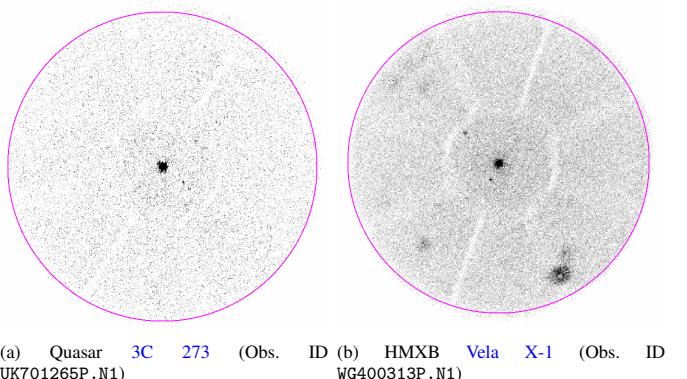
Figure 10: Examples of *ROSAT* PSPC pointed images with the circular footprint. The purple circle has a radius of 0.95°. The radial spikes are shadows of the so-called spider (the mount of the nested shells). Point sources become extended and smeared out at large off-axis angles due to the off-axis aberration that smears out the PSF.
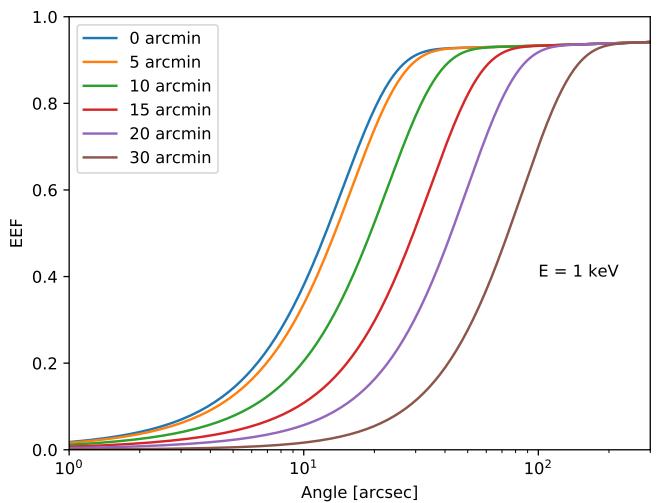
Figure 11: *ROSAT* PSPC cumulative point spread function (≡ EEF) as a function of angle with off-axis angle dependence at energy E=1 keV (Zimmermann et al., 1998, Eq. 5.13).
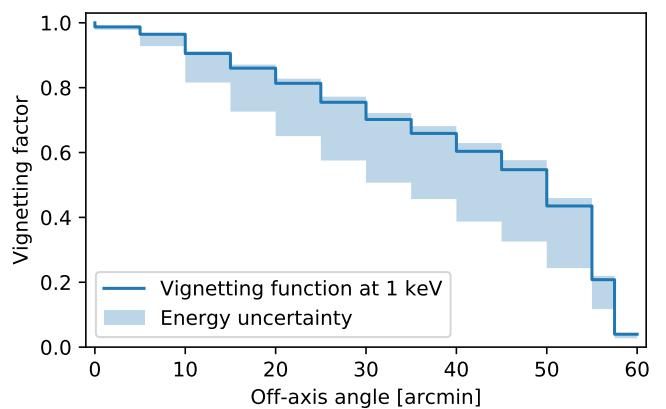
Figure 12: *ROSAT* PSPC vignetting function. The blue line represents the implemented 1 keV approximation. The shaded region shows the uncertainty originating from the energy dependence.

(a) LMXB Her X-1 (Obs. ID WG931139P_N1)   (b) HMXB Vela X-1 (Obs. ID WG932420P_N1)
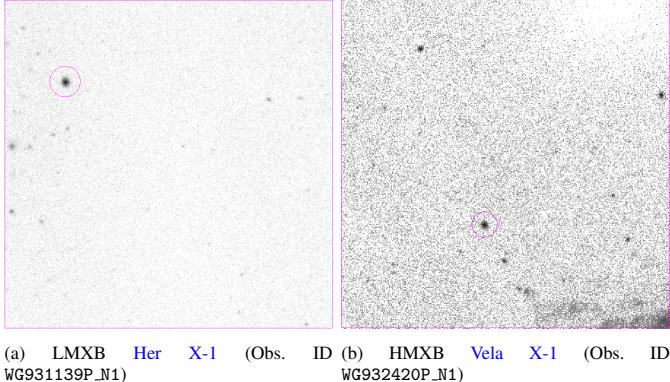
Figure 13: An example of *ROSAT* PSPC survey images from the RASS catalog with rectangular footprints. The targets are indicated by the 100″ source radius circle.

3.8.3. PSPC Survey

The Second *ROSAT* All-Sky Survey (RASS) Point Source Catalog (RASS2RXS [29]) originates from the survey phase of the mission between 1990 June and 1991 August and contains over 135 000 sources at a likelihood threshold of 6.5 (Boller et al., 2016). HILIGT uses a catalog search radius of 2′. Since the downloaded survey images are rectangular and represent the full FOV, the footprint is a simple rectangle. See Fig. 13 for two example images. Our *ROSAT* PSPC survey database contains 1378 footprints.

3.8.4. High Resolution Imager

Information about the HRI can be found in Pfeffermann et al. (1987), Briel et al. (1996), and Zimmermann et al. (1998). The ROSHRI catalog[30] contains arcsecond positions and count rates for 56 401 detected sources from 5393 *ROSAT* HRI observations. In total, 1.94% of the sky is covered with 13 452 high-confidence detections. The catalog is accessed with a search radius of 1′.

We download 5347 images from the HEASARC and use the background images for the footprint extraction with our footprint algorithm. The background images are smoothed and exhibit a clear, distinct border. We exclude negative background regions occurring in some images from the footprint. An example footprint is shown in Fig. 14. The data set includes 245 images with zero exposure and no counts, which were rejected from the database. The exposure time is inferred from the EXPOSURE keyword in the image. Overall, our database covers 5094 footprints.

The encircled energy fraction is shown in Fig. 15. HILIGT uses a source radius of 30″ for the upper limit calculation, which corresponds to an EEF of 94%. As for *ROSAT* PSPC, we fix the energy to 1 keV. This is a much better approximation (scattering < 10%) compared to the PSPC instrument (Zimmermann et al., 1998, Fig. 5.23–24). The vignetting of the HRI is
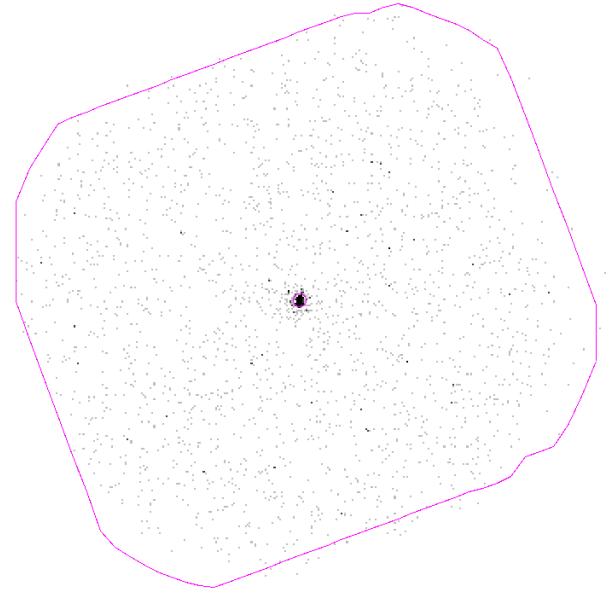
Figure 14: *ROSAT* HRI image of the quasar 3C 273 (Obs. ID CA141520H.N1). The footprint is calculated from the background image. The small circle displays the sources radius of 30″.
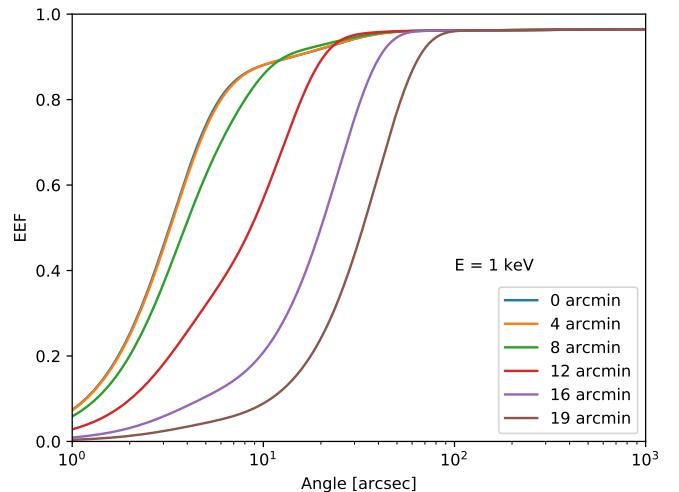
Figure 15: *ROSAT* HRI cumulative point spread function (≡ EEF) as a function of angle for various off-axis angles and fixed energy $E = 1$ keV (Zimmermann et al., 1998, Eq. 5.19).
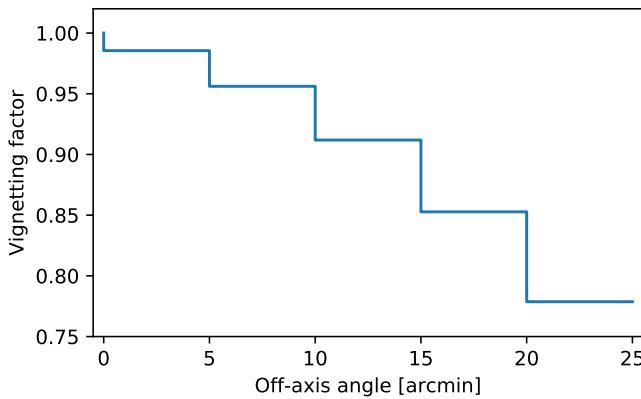
Figure 16: *ROSAT* HRI vignetting factors as a function of off-axis angle.

small compared to the PSPC instrument. It is inferred from table `vignet_hri.fits`, which is available at the MPE (see also p. 246 in Zimmermann et al., 1998), and plotted in Fig. 16.

3.9. ASCA (1993–2000)

Four X-ray telescopes (Serlemitsos et al., 1995) with two detectors were assembled on *ASCA* (Tanaka et al., 1994), a Gas Imaging Spectrometer (GIS, 0.8–12 keV, Ohashi et al. 1996; Makishima et al. 1996) and a Solid-state Imaging Spectrometer (SIS, 0.4–12 keV, Gendreau 1995). Further information can be found in Tsusaka et al. (1995) and Arida (1998).

3.9.1. ASCA GIS

The GIS consisted of two imaging gas scintillation proportional counters with a circular FOV of $50'$ and a spatial resolution of $\sim 0.5'$ at 5.9 keV. A major problem for the upper limit calculation is the intrinsic PSF of the GIS detector. Usually, the PSF is only constrained by the optics, however, the GIS detector induces additional image distortion which is heavily dependent on off-axis angle. We do not attempt to model the PSF and provide only results for the detected sources that are contained in the *ASCA* GIS catalog.

The *ASCA* Medium Sensitivity Survey (AMSS) is a serendipitous source survey for the extra-galactic sky $|b| > 10°$ and described by Ueda et al. (2001, 2005). The catalog lists a total of 2533 detected sources (5σ) from an area of $278 \deg^2$ in the bands 0.7–7 keV (*total*), 2–10 keV (*hard*) and 0.7–2 keV (*soft* band). The ASCAGIS catalog[31] consists of two sub-catalogs: AMSS-I with 1343 sources detected between 1993 May and 1996 December and AMSS-II with 1190 sources detected between 1997 January and 2000 May. The catalog gives the count rate in the three bands mentioned above. We compute the uncertainty of the count rate as (Ueda et al., 2001, p. 13)

$$\sigma_{CR} = \frac{CR}{\sigma_D} \quad , \qquad (12)$$

where CR is the count rate and where σ_D is the signal-to-noise ratio in units of sigma, given in column `SNR_Total/Hard/Soft` of the HEASARC catalog. The catalog does not provide background information. Furthermore, we use a catalog search radius of $3'$ for the *ASCA* GIS catalog cone search, the same value as the HEASARC.

3.9.2. ASCA SIS

The Solid-state Imaging Spectrometer consisted of two cameras with front-side illuminated CCD chips. It had an energy range of 0.4–10 keV and a FOV of $22' \times 22'$ with a spatial resolution of $30''$ (Gendreau, 1995). The ASCASIS catalog[32] is populated with target and serendipitous sources in the SIS FOV. The catalog was published by Gotthelf and White (1997), resulting from a search for point-like sources in the public *ASCA* data archive. The 0.5–12 keV count rate is extrapolated to the *total* band (0.2–12 keV), and we use a catalog search radius of $5'$ for the *ASCA* SIS catalog cone search. The catalog does not provide background information.

3.10. XMM-Newton (2000–2021+)

The European Space Agency's (ESA) X-ray Multi-Mirror Mission (*XMM-Newton*; Jansen et al. 2001) was launched on 1999 December 10 and is still working nominally at the time of writing. It carries three X-ray telescopes with high effective area and an optical monitor and orbits the Earth in a highly-elliptical 48 h orbit, which allows it to take long uninterrupted exposures. The telescopes have been designed to give a point spread function which is uniform as a function of photon energy and of off-axis angle. For reference, an extraction region of radius $30''$ contains 88% of 1.5 keV photons at an intermediate off-axis angle of $6'$. Three CCD cameras operate in parallel, the EPIC-pn (Strüder et al., 2001) back-illuminated detector and two EPIC-MOS front-illuminated CCDs (Turner et al., 2001), each receiving light from a nearly identical, nested Wolter I telescope. The MOS cameras share their telescope with one Reflection Grating Spectrometer each, and receive roughly half of the light. The EPIC instrumentation is sensitive to photons in the energy range 0.2–12 keV.

EPIC-pn has an energy resolution of 100 eV (FWHM) at 1 keV and a spatial resolution of $16''$ (half energy width) at 1.5 keV. It has a high quantum efficiency and has been shown to return a stable flux throughout the mission[33] It has > 2 times the throughput of the EPIC-MOS cameras and is the preferred instrument for upper limit measurements. Performance of the telescope and detector is well described in the *XMM-Newton Users Handbook* (SOC, 2020).

Each of the EPIC cameras carry a thin, medium and thick filter designed to block out optical light. They produce an increasingly important reduction in the soft X-ray (< 2 keV) photon flux and factors to convert count rates to flux are computed independently for each filter.

---

[31]https://heasarc.gsfc.nasa.gov/W3Browse/asca/ascagis.html

[32]https://heasarc.gsfc.nasa.gov/W3Browse/asca/ascasis.html

[33]"Stability of the EPIC-pn camera": http://xmmweb.esac.esa.int/docs/documents/CAL-TN-0212-1-0.pdf
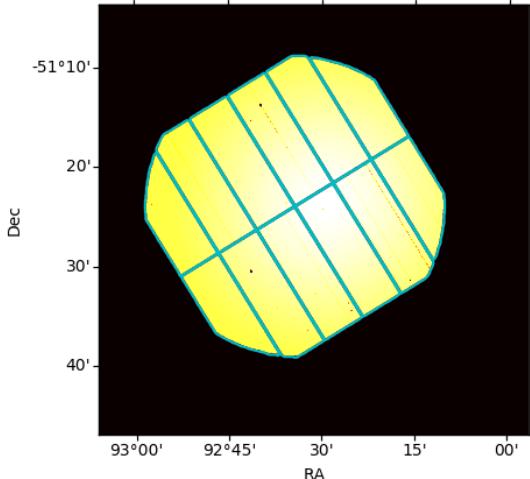
Figure 17: Example *XMM-Newton* pointed exposure map with footprint.

3.10.1. *XMM-Newton Pointed*

The products from pointed observations are stored in the (New) XMM-Newton science archive (NXSA) with a unique ten-digit identifier starting with "0". They have been made in relatively narrow bands and we combine bands 1, 2 and 3 to make the soft band (0.2–2 keV) image and exposure map and bands 4 and 5 to make the hard band (2–12 keV) products. The full band image is available directly as band 8. Lists of observations and associated images which contain a particular sky position are obtained by making TAP queries to the `public_observations`, `exposure` and `uls_exposure_image` tables within NXSA. The camera has a FOV of $27.2' \times 26.2'$. Footprints for each observation and for each slew are stored in the NXSA (see Fig. 17).

The vignetting function is energy-dependent, giving a throughput of ∼30% at the edge of the FOV for photons of 1.5 keV and ∼20% for 8 keV photons. This quantity is folded into the exposure map and is not used directly in the calculation. The *XMM-Newton* mirrors were designed to give a consistent encircled energy correction across the field of view. HILIGT uses the encircled energy correction for 1.5 keV photons located 6′ off-axis. The difference between this encircled energy correction and that of photons at 1′ or 10′ off-axis or of energy 1 keV or 6 keV is less than 5%.

The 4XMM-DR11 pointed source catalog (Webb et al., 2020) contains 602 543 unique sources from 12 210 EPIC-pn pointed observations that were public on 2020-12-31. The sky coverage is 1239 deg^2 (3% of the sky). 117 124 sources were observed multiple times[34]. Sources are located to within a median error of ∼ 1″ and are flagged to indicate issues which may potentially affect the returned count rates. HILIGT looks for sources within a radius of 10″ of the input position, which have been detected with the EPIC-pn camera and where the quality flag, `SUM_FLAG<2`. 112 084 detections are classified as extended with 34 173 marked as "clean" (`SUM_FLAG<1`).

Both pointed and slew observations have an exposure map and pointed observations also have a background map for each of the energy bands. These are used in the upper limit calculation. The background is calculated in slew observations from an annulus around the source center of inner radius 60″ and outer radius 120″. We note that HILIGT does not account for chip gaps in the EPIC-pn images and that the upper limit may be biased if the queried position falls into such a gap.

To estimate the chance of source confusion, we note that the *XMM-Newton* pointed observations exhibit about 50 sources per FOV for a deep observation. At an approximate (circular) FOV of 14′ radius and a cone search radius of 10″, the chance of randomly hitting a source in an average field would be roughly $\pi 10^2/(\pi(60 \cdot 14)^2) \cdot 50 \approx 0.1\%$. Of course in the Galactic center or very crowded regions, the source density and confusion chance is higher.

3.10.2. *XMM-Newton Slew*

XMM-Newton performs a shallow survey of the sky while slewing between pointed observation targets (Saxton et al., 2008), reaching a sensitivity of 6×10^{-13} erg cm^{-2}s^{-1} in the soft band, 4×10^{-12} erg cm^{-2}s^{-1} in the hard band, and 1×10^{-12} erg cm^{-2}s^{-1} in the total band. Pointing accuracy is limited by the ability to reconstruct the slew path and has a 1σ error of 8″.

Slew images (Fig. 18) containing a given sky position are found from TAP calls to the `slew_exposure` and `slew_exposure_image` tables. A limitation in some of the early pipeline products has led to some slew images being extremely large and impossible to process with the EUPPER task. These are excluded from the upper limit calculations. It is expected that the entire slew archive will be reprocessed in the near future to remove this limitation.

The slew catalog, XMMSL2, contains over 20 000 sources detected in 85% of the sky. Given the low sky density of sources a radius of 30″ is used in the catalog search. HILIGT dynamically links the *XMM-Newton* slew and pointed footprints and images to the NXSA, and always uses the latest catalog release.

3.10.3. *XMM-Newton Stacked*

The XMM-Newton Serendipitous Source Catalogue from overlapping observations ("stacked catalog") is a source catalog made from overlapping observations (Traulsen et al., 2019, 2020). Due to the longer effective exposure, upper limits of the stacks can provide a much deeper constraint on the flux than the pointed observations. However, the stacking also results in an averaging of the source count rate. We caution that for bright, flaring sources the averaged stacked flux can in fact be above the flux of a pointed observation, if it is in a low flux state[35]. The start and end date of the stacked data point or upper limit is given by the first and last observation of the stack, and should be interpreted as a mean over the whole time period.

---

[34] `http://xmmssc.irap.omp.eu/Catalogue/4XMM-DR11/4XMM-DR11_Catalogue_User_Guide.html` Sect. 5.1

[35] An example is 3C 273, which has a stacked 0.2–12 keV flux of $(1.330 \pm 0.001) \times 10^{-10}$ erg cm^{-2}s^{-1} but had, on 2000-06-16 (ObsID 0126700501) a flux of $(9.84 \pm 0.04) \times 10^{-11}$ erg cm^{-2}s^{-1}
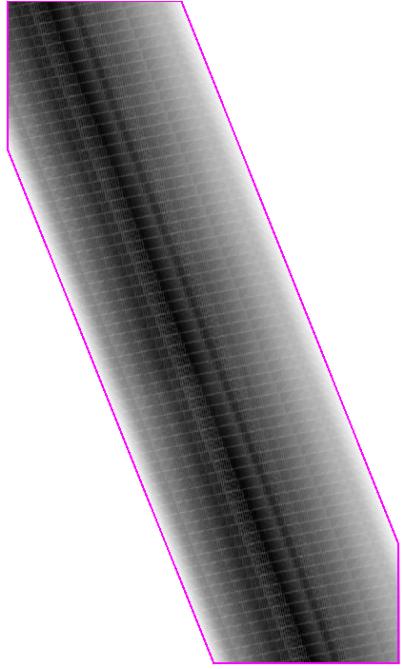
Figure 18: An example *XMM-Newton* slew exposure map with footprint.

(a) The interacting galaxies M82 (StackID 0434_009)

(b) The XMM-Large Scale Structure region (see also Pierre et al., 2007) (StackID 0072_352)

(c) Stacked PN images around position 01 19 05.14 +00 37 45.0 containing multiple faint X-ray sources (StackID 0861_045)

(d) The galaxy cluster ACO 2163 (StackID 0424_007)

Figure 19: Examples of the *XMM-Newton* stacked footprints. The footprints are calculated based on EPIC-pn coverage maps.

HILIGT currently accesses only EPIC-pn data of the 4XMM-DR11s stacked catalog. The footprints of each stack are computed based on the EPIC-pn coverage maps (Fig. 19). The HILIGT database contains 1328 footprints covering a total sky area of ~560 deg², from which 350 deg² are multiply observed. The catalog `epic_xmm_stack_cat` at the NXSA is queried with the options `pn_rate>0` (to obtain EPIC-pn data only) and `STACK_FLAG<=1` (to flag spurious entries). To connect the catalog entry to the database counterpart, we use a conversion table (Traulsen, priv. comm.) to map the `SRCID` to the `STACKID`. Finally, the upper limits are computed based on stacked images, exposure, and background maps in five energy bands. The same conversion factors, encircled energy fraction and vignetting as for *XMM-Newton* pointed is used (Sect. 3.10.1).

3.11. INTEGRAL (2002–2021+)

ESA's INTErnational Gamma-Ray Astrophysics Laboratory (*INTEGRAL*, Winkler et al. 2003) was launched on 2002 October 17 and is the only gamma-ray and coded-mask instrument included in HILIGT. The imager (IBIS, Ubertini et al. 2003) has a $8.3° \times 8.0°$ FOV with an angular resolution of $12'$ (FWHM) and total energy range of 15 keV-10 MeV. For HILIGT, we concentrate on the IBIS/ISGRI (Lebrun et al., 2003) count rates in three energy bands: 20–40, 40–60, and 60–100 keV. *INTEGRAL* observations are performed as a series of pointings called science windows (*scw*) that last between 30 and 60 minutes. Each *scw* is processed individually to produce reconstructed images (Goldwurm et al., 2003).

The count rates and variances in the three bands at each sky position are extracted from these reconstructed images and stored in a table. The values provided are based on the significance or signal-to-noise (σ) following one of three cases:

- $\sigma \geq 3$: The rate is given by the weighted mean count rate computed from the complete set of pointings that contain the given sky position, and the uncertainty is given by the error on that weighted mean.

- $3 < \sigma \leq 0$: For σ values below 3, the rate is given by twice the error on the mean divided by the average detection efficiency, and the uncertainty is given by -1.0 to indicate that the value is an upper limit. The average detection efficiencies are computed from the response files, and are 0.87, 0.64, and 0.64, respectively, for the three bands 20–40, 40–60, and 60–100 keV.

- $\sigma < 0$: This case exists because the reconstructed count rate in each sky pixel in the absence of sources is normally distributed, and the significance approximates a standard normal variable. Signal and background counts are equal and given by the error on the weighted mean rate multiplied by the exposure time and the data point is displayed as an upper limit.

In the first two cases of the estimated signal and background counts, for any value of σ above 0, the signal counts, S, are given by the rounded value of the weighted mean rate multiplied by the effective position-dependent exposure time. The background counts, B, are derived from the standard formula $\sigma = S / \sqrt{S + B}$, and thus given by $(S/\sigma)^2 - S$.

We use *INTEGRAL* data up to May 2016. We note that we
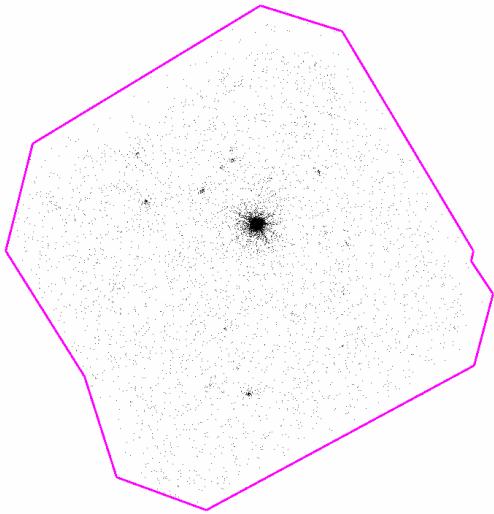
Figure 20: An example *Swift* XRT image of 3C 273 (ObsID 00035019004) with footprint.

do not include any catalog values (as available, e.g., in Krivonos et al. 2007 or at `www.isdc.unige.ch/integral/science/catalogue`). *INTEGRAL*'s FOV is $8.3° \times 8.0°$, larger than that of most X-ray missions, and each sky position is observed a large number of times. We currently provide one data point averaged over the 16 years of observation. As *INTEGRAL* is a hard X-ray/soft γ-ray mission, we provide only a powerlaw spectral model. These conversion factors are time dependent due to slow ageing of the IBIS/ISGRI detectors by cosmic radiation, changing the effective area over time. Nevertheless, we use conversion factors which are averaged over the 16 years time period and computed with the OSA 10 software (see Table A.4).

It is important to note that because IBIS/ISGRI is a coded mask instrument, the variance map from which the errors are taken, and the intensity map from which the rates are taken, are computed independently: the intensity map is reconstructed based on spatial information derived from knowledge of the mask pattern, whereas the variance map relies only on the number of photons detected on the detector plane.

3.12. Swift (2005–2021+)

The X-ray Telescope (XRT; Burrows et al. 2005) on the *Neil Gehrels Swift Observatory* (Gehrels et al., 2004) has a CCD detector with a circular field of view radius $12.3'$, and an energy range of 0.3–10 keV. A typical *Swift* XRT image is shown in Fig. 20.

HILIGT makes use of the 2SXPS catalog (Evans et al., 2020). It contains data from the end of early operations phase 2005-01-01 to 2018-08-01, and provides exposure and background maps (including the model PSF of any detected sources) for each field, and in four energy bands. HILIGT queries the 2SXPS upper limit server provided at the UK Swift Science Data Centre[36]. The majority of fields within 2SXPS have been

observed multiple times, thus multiple upper limits or count-rates can be returned.

To identify the *Swift* footprint at the requested position, initially any observation within $28'$ was found. Within each observation, and for each requested energy band, a cone search radius $20''$ identified any matching source and its count rate was extracted from 2SXPS. If no source was found, a circular region of radius $28''$ (12 image pixels) centered at the input position was created. The exposure at this position was taken from the exposure map within 2SXPS; only datasets where the mean exposure in this circle was at least 1% of the on-axis exposure were accepted. For those datasets, the number of counts in the image, the sum of the background map and average value of the exposure map in this region were returned to HILIGT. A correction factor was also calculated which accounted both for the fraction of the EEF outside the circular region and for vignetting or bad columns within the region (see Evans et al. 2020, Sect. 3.3 for details). The values from the soft (0.3–1 keV) and medium (1–2 keV) bands were combined to give values in the 0.3–2 keV band, and then the upper limits were calculated as described in Sect. 2.1-2.2.

---

[36]`https://www.swift.ac.uk/2SXPS/ulserv.php`

Table 1: Overview of parameters for each mission. The energy range of the catalog count rates is in keV with the corresponding HILIGT band in parenthesis. The source radius (r in Sect. 2.1) defines the size of the circular region for source counts estimation, and, if no background map is available, of the background annulus. The columns "UL/Bkg/Exp/P" indicate whether there is an upper limit calculation, and whether it makes use of background and exposure maps, and whether PIMMS is used to compute the conversion factors. In the "Notes" column we indicate, if available, the number of sources in the catalog, and the number of images that are included in the upper limit calculations. The reference numbers correspond to: 1:Arida (1998), 3:Aschenbach (1988), 6:Boller et al. (2016), 7:Briel et al. (1996), 8:Burrows et al. (2005), 9:D.E. Harris (1984), 10:de Korte et al. (1981), 11:Evans et al. (2020), 12:Forman et al. (1978), 15:Gehrels et al. (2004), 16:Gendreau (1995), 17:Giacconi et al. (1979), 18:Giacconi et al. (1971), 19:Gioia et al. (1990), 22:Gorenstein et al. (1981), 23:Gotthelf and White (1997), 25:Harnden et al. (1984), 26:Harris (1990), 29:Hayashida et al. (1989), 30:Henry et al. (1977), 31:Holt (1976), 33:Jansen et al. (2001), 35:Kaluzienski (1977), 42:Lebrun et al. (2003), 46:Makino and ASTRO-C Team (1987), 47:Makishima et al. (1996), 49:McHardy et al. (1981), 52:Nugent et al. (1983), 53:Ohashi et al. (1996), 55:Pfeffermann et al. (1987), 56:Piccinotti et al. (1982), 61:Reynolds et al. (1999), 63:Rothschild et al. (1979), 64:Saxton et al. (2008), 65:Serlemitsos et al. (1995), 69:Strüder et al. (2001), 70:Tanaka et al. (1994), 71:Terrell et al. (1982), 72:Traulsen et al. (2019), 73:Traulsen et al. (2020), 74:Trümper (1982), 75:Tsusaka et al. (1995), 77:Turner et al. (1981), 78:Turner et al. (1989), 79:Ubertini et al. (2003), 80:Ueda et al. (2001), 81:Ueda et al. (2005), 82:Villa et al. (1976), 83:Warwick et al. (1981), 84:Webb et al. (2020), 86:White and Peacock (1988), 87:Whitlock et al. (1992a), 88:Whitlock et al. (1992b), 90:Winkler et al. (2003), 91:Wood et al. (1984), 92:Zimmermann et al. (1998)

Mission	Energy range	FOV	Spatial res.	Source radius	Cat. name (search rad.)	Cat. size	UL	Bkg	Exp	P	Instr./Filters	References	Notes
Vela 5B	3–12 (hard)	6.1°×6.1°	6° FWHM		–	–	N	N	N	N	XC	71; 87; 88	lightcurves of 99 sources
Uhuru	2–6 (hard)	0.52°×0.52° / 5.2°×5.2°			UHURU4 (60′)	339	N	N	N	N		12; 18	only catalog, 339 sources
Ariel V SSI	2–18 (hard)	0.75°×10.6°			ARIEL3A (30′)	250	N	N	N	N		Instr.: 82; 87, Cat.: 49; 83	only catalog, 251 sources
Ariel V ASM	3–6 (hard)	0.75°×10.6°				–	N	N	N	N		31; 35	lightcurves of 249 sources
HEAO-1 A-1	0.5–25 (hard)	1.5°×3°			A1 (60′)	842	N	N	N	N		91	only catalog, 842 sources
HEAO-1 A-2	0.44–2.8 (soft)				A2LED (60′)	114	N	N	N	N		63; 52	only catalog, 114 sources
	2–10 (hard)				A2PIC (60′)	68	N	N	N	N		56	only catalog, 68 sources, $|b| > 20°$
Einstein IPC	0.2–3.5 (soft)	75′×75′	1′	5.9 / 11′ @ 0.5 EEF	IPC (2′)	6816	Y	N	Y	Y		Instr.: 17; 22; 25, Cat.: 19; 26	B1950→J2000, 3923 images
					IPCIMAGE (15′)	4132	Y	N	Y	Y			
Einstein HRI	0.15–3.5 (soft)	25′ diam.	3″	18″ @ 0.8 EEF	HRICFA (1′)	598	Y	N	Y	Y		Instr.: 9; 17; 30	B1950→J2000, 836 images
					HRIIMAGE (15′)	870	Y	N	Y	Y			
EXOSAT LE	0.05–2 (soft)	2° diam.	18″	1′	LE (1′)	2563	Y	N	N	Y	CMA	Instr.: 10; 86	B1950→J2000, 3677 imgs.
EXOSAT ME Pointed	1–15 (hard)	45′×45′			ME (45′)	2291	N	N	N	Y		Instr.: 10; 77; 86	only catalog
EXOSAT ME Slew	1–8 (hard)				EXMS (60′)	1210	Y			Y		Cat.: 61	only cat, 1210 srcs, 98% of sky
GINGA LAC	2–10 (hard)	0.8°×1.7°	6″		GINGALAC (10′)	419	N	N	N	Y	Top	Instr.: 29; 46; 78	only catalog
ASCA GIS	0.7–2 (soft) / 2–10 (hard) / 0.7–7 (total)	50′	0.5′	5′	ASCAGIS (3′)	2533	N	N	N	Y		Instr.: 1; 47; 53; 65 / 70; 75 / Cat.: 80; 81	only cat, 2533 srcs, 278 deg²
ASCA SIS	0.5–12 (total)	22′×22′	30″	3.3′ @ 0.5 EEF	ASCASIS (5′)	433	N	N	N	Y		Instr.: 16; 65; 70; 75 / Cat.: 23	only catalog
ROSAT PSPC Pointed	0.1–2.34 (soft)	2° diam.		100″	ROSPSPC (0.5′)	54133	Y	N	Y	Y	Open	Instr.: 3; 7; 55; 74; 92	5490 imgs., 100048 srcs., 17.3% of sky
ROSAT PSPC Survey	0.1–2.4 (soft)	38′ square			RASS2RXS (2′)	135118	Y	N	Y	Y	Open	Cat.: 6	1378 imgs., 135000 srcs., all-sky
ROSAT HRI Pointed	0.2–2.4 (soft)	undef.	2″ FWHM	30″ @ 0.94 EEF	ROSHRI (1′)	13452	Y	Y	N	Y	Open	Instr.: 3; 7; 55; 74; 92	5094 imgs., 56401 srcs., 1.94% of sky
XMM-Newton Pointed	0.2–2 (soft)	27.2′×26.2′	6″ FWHM	30″ @ 0.876 EEF	epic.source.cat (10″)	895415	Y	Y	Y	Y	EPIC-pn	Instr.: 33; 69, Cat.: 84	602543 srcs., 12210 imgs., 1239 deg²
XMM-Newton Slew	2–12 (hard)	undef.	8″		slew.source.cat (20″)	72352	Y	Y	Y	Y	EPIC-pn	Cat.: 64	23252 sources, 85% of sky
XMM-Newton Stacked	0.2–12 (total)	undef.			epic.xmm.stack.cat (10″)	358809	Y	Y	Y	Y	EPIC-pn	Cat.: 72; 73	1328 imgs., 358809 srcs., 560 deg²
INTEGRAL	20–40 / 40–60 / 60–100	8.3°×8.0°	12′ FWHM		–	–	Y	Y	Y	N	IBIS/ISGRI	Instr.: 42; 79; 90	no catalog
Swift XRT	0.2–2 (soft) / 2–10 (hard) / 0.3–10 (total)	12.3′ rad.	18″ HEW	28″	2SXPS (20″)	1091058	Y	Y	Y	Y	PC	Instr.: 8; 15 / Cat.: 11	48931 imgs., 206335 srcs., 3790 deg²

4. Summary

The high-energy lightcurve generator (HILIGT) is a simple and fast tool that produces long-term lightcurves by combining archival data and upper limit estimates. Already by providing a unified access to most of the relevant X-ray catalogs, HILIGT is of excellent use for X-ray and multi-wavelength researchers to quickly get an overview of existing data, and study the past history of the source. Through the addition of upper limits, valuable information about periods of decreased source activity are added to the lightcurve. This is information that can be used to study, for instance, off-states and transient phenomena. Only through the combination of various missions, variability patterns on decade-long time scales can be resolved, which opens a new discovery space as the data coverage of X-ray sources constantly increases.

This paper, which describes the back-end of HILIGT, is complementary to Paper I where we describe the front end together with an overview of the server structure and science use-cases. Here, we described the back-end. Firstly, we showed how upper limits are calculated in HILIGT and which database implementation we use. Upper limits from image data are available for the missions *Einstein*, *EXOSAT*, *ROSAT*, *Swift*, *INTEGRAL*, and *XMM-Newton*, and we described their footprints, catalog calls, vignetting and encircled energy fraction. Besides calculating upper limits of these missions, HILIGT provides archival catalog data for formerly mentioned missions, as well as for *Uhuru*, *Ariel V*, *HEAO-1*, *GINGA*, and *ASCA*. With the inclusion of these historical catalogs – notably the Fourth Uhuru and *HEAO-1* Piccinotti catalog – HILIGT is able to calculate lightcurves as long as 50 years, covering the greater part of space-based X-ray astronomy. Additionally, all-sky monitor lightcurves of *Vela 5B* and *Ariel V* are included, which provide the opportunity to directly compare data from some of the earliest X-ray satellites.

Due to the different effective areas of the satellites, count rates cannot be directly compared among the instruments. HILIGT therefore transforms the count rates to a physical flux using a selection of spectral models as an approximation, such as an absorbed power-law or a black body. We cautioned the user about the importance of the correct choice of the spectral model (see Sect. 2.2), which can otherwise lead to systematic offsets in the derived fluxes.

Finally, we emphasize that this paper comprises a detailed and universally researched composition of many current and past X-ray satellites. As the extraction of calibration data from old mission papers can be time-consuming, this paper can serve as a look-up reference to easily access the most relevant information.

Future plans on HILIGT are the inclusion of additional missions such as *Chandra*, the ASM of *RXTE* and *GINGA*, and *NuSTAR*. We also plan to add new spectral models such as APEC and thermal Bremsstrahlung, which are included in PIMMS but not yet in HILIGT. To give the user increased control over spectral models and output energy ranges it is also planned to implement an on-the-fly computation of the flux conversion factors.

References

Arida, M., 1998. ASCA Technical Description. Technical Report. Laboratory of High Energy Astrophysics, NASA GSFC, Greenbelt. https://heasarc.gsfc.nasa.gov/docs/asca/ao7/appendix_e/ao7_appendix_e.html.

Arnaud, K., Smith, R., Siemiginowska, A., 2011. Handbook of X-ray Astronomy. Cambridge University Press.

Aschenbach, B., 1988. Design, construction, and performance of the ROSAT high- resolution x-ray mirror assembly. Appl. Opt. 27, 1404–1413. doi:10.1364/AO.27.001404.

Astropy Collaboration, Robitaille, T.P., Tollerud, E.J., Greenfield, P., Droettboom, M., Bray, E., Aldcroft, T., Davis, M., Ginsburg, A., Price-Whelan, A.M., 2013. Astropy: A community Python package for astronomy. A&A 558, A33. doi:10.1051/0004-6361/201322068, arXiv:1307.6212.

Belloni, T.M., Motta, S.E., Muñoz-Darias, T., 2011. Black hole transients. Bulletin of the Astronomical Society of India 39, 409–428. arXiv:1109.3388.

Boller, T., Freyberg, M.J., Trümper, J., Haberl, F., Voges, W., Nandra, K., 2016. Second ROSAT all-sky survey (2RXS) source catalogue. A&A 588, A103. doi:10.1051/0004-6361/201525648, arXiv:1609.09244.

Briel, U., Aschenbach, B., Hasinger, G., Hippmann, H., Pfeffermann, E., Predehl, P., Schmitt, J., Schwentker, O., Voges, W., Zimmermann, U. (Eds.), 1996. ROSAT User's Handbook, Max-Planck-Institut für Extraterrestrische Physik, 85740 Garching bei München, Germany. https://heasarc.gsfc.nasa.gov/docs/rosat/ruh/handbook/handbook.html.

Burrows, D.N., Hill, J.E., Nousek, J.A., Kennea, J.A., Wells, A., Osborne, J.P., Abbey, A.F., Beardmore, A., Mukerjee, K., Short, A.D.T., Chincarini, G., Campana, S., Citterio, O., Moretti, A., Pagani, C., Tagliaferri, G., Giommi, P., Capalbi, M., Tamburelli, F., Angelini, L., Cusumano, G., Bräuninger, H.W., Burkert, W., Hartner, G.D., 2005. The Swift X-Ray Telescope. Space Sci. Rev. 120, 165–195. doi:10.1007/s11214-005-5097-2, arXiv:arXiv:astro-ph/0508071.

D.E. Harris, D.I., 1984. Einstein Observatory Revised User's Manual. Technical Report 2. Harvard-Smithonian Center for Astrophysics. https://heasarc.gsfc.nasa.gov/docs/einstein/.

de Korte, P.A.J., Bleeker, J.A.M., den Boggende, A.J.F., Branduardi-Raymont, G., Brinkman, A.C., Culhane, J.L., Gronenschild, E.H.B.M., Mason, I., McKechnie, S.P., 1981. The X-ray imaging telescopes on EXOSAT. Space Sci. Rev. 30, 495–511. doi:10.1007/BF01246070.

Evans, P.A., Page, K.L., Osborne, J.P., Beardmore, A.P., Willingale, R., Burrows, D.N., Kennea, J.A., Perri, M., Capalbi, M., Tagliaferri, G., Cenko, S.B., 2020. 2SXPS: An Improved and Expanded Swift X-Ray Telescope Point-source Catalog. ApJS 247, 54. doi:10.3847/1538-4365/ab7db9, arXiv:1911.11710.

Forman, W., Jones, C., Cominsky, L., Julien, P., Murray, S., Peters, G., Tananbaum, H., Giacconi, R., 1978. The fourth Uhuru catalog of X-ray sources. ApJS 38, 357–412. doi:10.1086/190561.

Gabriel, C., Denby, M., Fyfe, D.J., Hoar, J., Ibarra, A., Ojero, E., Osborne, J., Saxton, R.D., Lammers, U., Vacanti, G., 2004. The XMM-Newton SAS - Distributed Development and Maintenance of a Large Science Analysis System: A Critical Analysis, in: Ochsenbein, F., Allen, M.G., Egret, D. (Eds.), Astronomical Data Analysis Software and Systems (ADASS) XIII, p. 759.

Gehrels, N., 1986. Confidence Limits for Small Numbers of Events in Astrophysical Data. ApJ 303, 336. doi:10.1086/164079.

Gehrels, N., Chincarini, G., Giommi, P., Mason, K.O., Nousek, J.A., Wells, A.A., White, N.E., Barthelmy, S.D., Burrows, D.N., Cominsky, L.R., Hurley, K.C., Marshall, F.E., Mészáros, P., Roming, P.W.A., Angelini, L., Barbier, L.M., Belloni, T., Campana, S., Caraveo, P.A., Chester, M.M., Citterio, O., Cline, T.L., Cropper, M.S., Cummings, J.R., Dean, A.J., Feigelson, E.D., Fenimore, E.E., Frail, D.A., Fruchter, A.S., Garmire, G.P., Gendreau, K., Ghisellini, G., Greiner, J., Hill, J.E., Hunsberger, S.D., Krimm, H.A., Kulkarni, S.R., Kumar, P., Lebrun, F., Lloyd-Ronning, N.M., Markwardt, C.B., Mattson, B.J., Mushotzky, R.F., Norris, J.P., Osborne, J., Paczynski, B., Palmer, D.M., Park, H.S., Parsons, A.M., Paul, J., Rees, M.J., Reynolds, C.S., Rhoads, J.E., Sasseen, T.P., Schaefer, B.E., Short, A.T., Smale, A.P., Smith, I.A., Stella, L., Tagliaferri, G., Takahashi, T., Tashiro, M., Townsley, L.K., Tueller, J., Turner, M.J.L., Vietri, M., Voges, W., Ward, M.J., Willingale, R., Zerbi, F.M., Zhang, W.W., 2004. The Swift Gamma-Ray Burst Mission. ApJ 611, 1005–1020. doi:10.1086/422091.

Gendreau, K.C., 1995. X-Ray Ccds for Space Applications: Calibration, Radiation Hardness, and Use for Measuring the Spectrum of the Cosmic X-Ray Background. Ph.D. thesis. MASSACHUSETTS INSTITUTE OF TECHNOLOGY.

Giacconi, R., Branduardi, G., Briel, U., Epstein, A., Fabricant, D., Feigelson, E., Forman, W., Gorenstein, P., Grindlay, J., Gursky, H., Harnden, F.R., Henry, J.P., Jones, C., Kellogg, E., Koch, D., Murray, S., Schreier, E., Seward, F., Tananbaum, H., Topka, K., Van Speybroeck, L., Holt, S.S., Becker, R.H., Boldt, E.A., Serlemitsos, P.J., Clark, G., Canizares, C., Markert, T., Novick, R., Helfand, D., Long, K., 1979. The Einstein /HEAO 2/ X-ray Observatory. ApJ 230, 540–550. doi:10.1086/157110.

Giacconi, R., Kellogg, E., Gorenstein, P., Gursky, H., Tananbaum, H., 1971. An X-Ray Scan of the Galactic Plane from UHURU. ApJ 165, L27. doi:10.1086/180711.

Gioia, I.M., Maccacaro, T., Schild, R.E., Wolter, A., Stocke, J.T., Morris, S.L., Henry, J.P., 1990. The Einstein Observatory Extended Medium-Sensitivity Survey. I - X-ray data and analysis. ApJS 72, 567–619. doi:10.1086/191426.

Gokus, A., Rau, A., Wilms, J., Ducci, L., Koenig, O., Weber, P., Boller, T., Malyali, A., 2020. SRGt J071522.1-191609: SRG/eROSITA discovery of a bright transient X-ray source. The Astronomer's Telegram 13657, 1.

Goldwurm, A., David, P., Foschini, L., Gros, A., Laurent, P., Sauvageon, A., Bird, A.J., Lerusse, L., Produit, N., 2003. The INTEGRAL/IBIS scientific data analysis. A&A 411, L223–L229. doi:10.1051/0004-6361:20031395, arXiv:astro-ph/0311172.

Gorenstein, P., Harnden, Jr., F.R., Fabricant, D.G., 1981. In orbit performance of the Einstein Observatory/HEAO-2 Imaging Proportional Counter. IEEE Transactions on Nuclear Science 28, 869–874. doi:10.1109/TNS.1981.4331295.

Gotthelf, E.V., White, N.E., 1997. The ASCA SIS Source Catalog, in: Makino, F., Mitsuda, K. (Eds.), X-Ray Imaging and Spectroscopy of Cosmic Hot Plasmas, p. 31.

Grindlay, J., Gursky, H., Schnopper, H., Parsignault, D.R., Heise, J., Brinkman, A.C., Schrijver, J., 1976. Discovery of intense X-ray bursts from the globular cluster NGC 6624. ApJ 205, L127–L130. doi:10.1086/182105.

Harnden, Jr., F.R., Fabricant, D.G., Harris, D.E., Schwarz, J., 1984. Scientific Specification of the Data Analysis System for the EINSTEIN Observatory (HEAO-2) Imaging Proportional Counter. SAO Special Report 393.

Harris, D.E., 1990. The Einstein Observatory Catalog of IPC X-ray Sources. Smithsonian Institution, Astrophysical Observatory.

Hartman, J.M., Patruno, A., Chakrabarty, D., Kaplan, D.L., Markwardt, C.B., Morgan, E.H., Ray, P.S., van der Klis, M., Wijnands, R., 2008. The Long-Term Evolution of the Spin, Pulse Shape, and Orbit of the Accretion-powered Millisecond Pulsar SAX J1808.4-3658. ApJ 675, 1468–1486. doi:10.1086/527461, arXiv:0708.0211.

Hasinger, G., van der Klis, M., 1989. Two patterns of correlated X-ray timing and spectral behaviour in low-mass X-ray binaries. A&A 225, 79–96.

Hayashida, K., Inoue, H., Koyama, K., Awaki, H., Takano, S., 1989. The origin and behavior of the background in the large area counters on GINGA and its effect on the sensitivity. PASJ 41, 373–389.

Henry, J.P., Kellogg, E.M., Murray, S.S., van Speybroeck, L.P., Bjorkholm, P.J., Briel, U.G., 1977. High resolution imaging X-ray detector for astronomical measurements, in: Chase, R.C., Kuswa, G.W. (Eds.), X-ray imaging, pp. 196–205. doi:10.1117/12.955472.

Holt, S.S., 1976. Temporal X-Ray Astronomy with a Pinhole Camera. Ap&SS 42, 123–141. doi:10.1007/BF00645534.

Houck, J.C., 2002. ISIS: The Interactive Spectral Interpretation System, in: Branduardi-Raymont, G. (Ed.), High Resolution X-ray Spectroscopy with XMM-Newton and Chandra, p. 17.

Jansen, F., Lumb, D., Altieri, B., Clavel, J., Ehle, M., Erd, C., Gabriel, C., Guainazzi, M., Gondoin, P., Much, R., Munoz, R., Santos, M., Schartel, N., Texier, D., Vacanti, G., 2001. XMM-Newton observatory. I. The spacecraft and operations. A&A 365, L1–L6. doi:10.1051/0004-6361:20000036.

Joye, W.A., Mandel, E., 2003. New Features of SAOImage DS9, in: Payne, H.E., Jedrzejewski, R.I., Hook, R.N. (Eds.), Astronomical Data Analysis Software and Systems XII, p. 489.

Kaluzienski, L.J., 1977. Studies of Transient X-Ray Sources with the Ariel 5 All-Sky Monitor. Ph.D. thesis. National Aeronautics and Space Administration. Goddard Space Flight Center, Greenbelt, MD.

Komossa, S., Bade, N., 1999. The giant X-ray outbursts in NGC 5905 and IC 3599:() hfill Follow-up observations and outburst scenarios. A&A 343, 775–787. arXiv:astro-ph/9901141.

König, O., 2019. Extension of Upper Limit Servers and spectral analysis of

the X-ray binary GRO J1744-28. Master's thesis. Friedrich-Alexander-Universität Erlangen-Nürnberg. Germany. https://www.sternwarte.uni-erlangen.de/docs/theses/2019-07_Koenig.pdf.

Kraft, R.P., Burrows, D.N., Nousek, J.A., 1991. Determination of confidence limits for experiments with low numbers of counts. ApJ 374, 344–355. doi:10.1086/170124.

Krivonos, R., Revnivtsev, M., Lutovinov, A., Sazonov, S., Churazov, E., Sunyaev, R., 2007. INTEGRAL/IBIS all-sky survey in hard X-rays. A&A 475, 775–784. doi:10.1051/0004-6361:20077191, arXiv:astro-ph/0701836.

Kuulkers, E., in't Zand, J.J.M., Lasota, J.P., 2009. Restless quiescence: thermonuclear flashes between transient X-ray outbursts. A&A 503, 889–897. doi:10.1051/0004-6361/200810981, arXiv:0809.3323.

Lampton, M., Margon, B., Bowyer, S., 1976. Parameter estimation in X-ray astronomy. ApJ 208, 177–190. doi:10.1086/154592.

Lebrun, F., Leray, J.P., Lavocat, P., Crétolle, J., Arquès, M., Blondel, C., Bonnin, C., Bouère, A., Cara, C., Chaleil, T., Daly, F., Desages, F., Dzitko, H., Horeau, B., Laurent, P., Limousin, O., Mathy, F., Mauguen, V., Meignier, F., Molinié, F., Poindron, E., Rouger, M., Sauvageon, A., Tourrette, T., 2003. ISGRI: The INTEGRAL Soft Gamma-Ray Imager. A&A 411, L141–L148. doi:10.1051/0004-6361:20031367, arXiv:astro-ph/0310362.

Levine, A.M., Lang, F.L., Lewin, W.H.G., Primini, F.A., Dobson, C.A., Doty, J.P., Hoffman, J.A., Howe, S.K., Scheepmaker, A., Wheaton, W.A., Matteson, J.L., Baity, W.A., Gruber, D.E., Knight, F.K., Nolan, P.L., Pelling, R.M., Rothschild, R.E., Peterson, L.E., 1984. The HEAO1 A-4 catalog of high-energy X-ray sources. ApJS 54, 581–617. doi:10.1086/190944.

Lin, D., Guillochon, J., Komossa, S., Ramirez-Ruiz, E., Irwin, J.A., Maksym, W.P., Grupe, D., Godet, O., Webb, N.A., Barret, D., Zauderer, B.A., Duc, P.A., Carrasco, E.R., Gwyn, S.D.J., 2017. A likely decade-long sustained tidal disruption event. Nature Astronomy 1, 0033. doi:10.1038/s41550-016-0033, arXiv:1702.00792.

Loiseau, N., Baines, D., Colomo, E., Giordano, F., Merín, B., Racero, E., Rodríguez, P., Salgado, J., Sarmiento, M., 2017. The XMM-Newton Science Archive and its integration into ESASky, in: Revista Mexicana de Astronomia y Astrofisica Conference Series, pp. 146–146. https://www.cosmos.esa.int/web/xmm-newton/xsa.

Makino, F., ASTRO-C Team, 1987. The X-ray astronomy satellite Astro-C. Astrophys. Lett. 25, 223–233.

Makishima, K., Tashiro, M., Ebisawa, K., Ezawa, H., Fukazawa, Y., Gunji, S., Hirayama, M., Idesawa, E., Ikebe, Y., Ishida, M., 1996. In-Orbit Performance of the Gas Imaging Spectrometer onboard ASCA. PASJ 48, 171–189. doi:10.1093/pasj/48.2.171.

Malyali, A., Rau, A., Arcodia, R., Boller, T., Carpano, S., Haberl, F., Merloni, A., Nandra, K., Buchner, J., Liu, T., Salvato, M., Wilms, J., Koenig, O., Krumpe, M., Lamer, G., 2020. eRASSt J082337+042303: A bright, ultra-soft, high-amplitude transient in the direction of 2MASX J08233674+042300. The Astronomer's Telegram 13712, 1.

McHardy, I.M., Lawrence, A., Pye, J.P., Pounds, K.A., 1981. The Ariel V (3A) catalogue of X-ray sources. II. MNRAS 197, 893–919. doi:10.1093/mnras/197.4.893.

Menou, K., Esin, A.A., Narayan, R., Garcia, M.R., Lasota, J.P., McClintock, J.E., 1999. Black Hole and Neutron Star Transients in Quiescence. ApJ 520, 276–291. doi:10.1086/307443, arXiv:astro-ph/9810323.

Mukai, K., 1993. PIMMS and Viewing: proposal preparation tools. Legacy 3. URL: https://heasarc.gsfc.nasa.gov/docs/journal/pimms3.html.

Nugent, J.J., Jensen, K.A., Nousek, J.A., Garmire, G.P., Mason, K.O., Walter, F.M., Bowyer, C.S., Stern, R.A., Riegler, G.R., 1983. HEAO A-2 soft X-ray source catalog. ApJS 51, 1–28. doi:10.1086/190838.

Ohashi, T., Ebisawa, K., Fukazawa, Y., Hiyoshi, K., Horii, M., Ikebe, Y., Ikeda, H., Inoue, H., Ishida, M., Ishisaki, Y., 1996. The Gas Imaging Spectrometer on Board ASCA. PASJ 48, 157–170. doi:10.1093/pasj/48.2.157.

Peacock, A., Andresen, R.D., Manzo, G., Taylor, B.G., Villa, G., Re, S., Ives, J.C., Kellock, S., 1981. The gas scintillation proportional counter on EXOSAT. Space Sci. Rev. 30, 525–534. doi:10.1007/BF01246072.

Pfeffermann, E., Briel, U.G., Hippmann, H., Kettenring, G., Metzner, G., Predehl, P., Reger, G., Stephan, K.H., Zombeck, M., Chappell, J., Murray, S.S., 1987. The focal plane instrumentation of the ROSAT Telescope, in: Soft X-ray optics and technology, p. 519.

Piccinotti, G., Mushotzky, R.F., Boldt, E.A., Holt, S.S., Marshall, F.E., Serlemitsos, P.J., Shafer, R.A., 1982. A complete X-ray sample of the high-latitude /absolute value of B greater than 20 deg/ sky from HEAO 1 A-2 - Log N-log S and luminosity functions. ApJ 253, 485–503. doi:10.1086/159651.

Pierre, M., Chiappetti, L., Pacaud, F., Gueguen, A., Libbrecht, C., Altieri, B., Aussel, H., Gandhi, P., Garcet, O., Gosset, E., Paioro, L., Ponman, T.J., Read, A.M., Refregier, A., Starck, J.L., Surdej, J., Valtchanov, I., Adami, C., Alloin, D., Alshino, A., Andreon, S., Birkinshaw, M., Bremer, M., Detal, A., Duc, P.A., Galaz, G., Jones, L., Le Fèvre, J.P., Le Fèvre, O., Maccagni, D., Mazure, A., Quintana, H., Röttgering, H.J.A., Sprimont, P.G., Tasse, C., Trinchieri, G., Willis, J.P., 2007. The XMM-Large Scale Structure catalogue: X-ray sources and associated optical data. Version I. MNRAS 382, 279–290. doi:10.1111/j.1365-2966.2007.12354.x, arXiv:0708.3299.

Pounds, K.A., Allan, D.J., Barber, C., Barstow, M.A., Bertram, D., Branduardi-Raymont, G., Brebner, G.E.C., Buckley, D., Bromage, G.E., Cole, R.E., Courtier, M., Cruise, A.M., Culhane, J.L., Denby, M., Donoghue, D.O., Dunford, E., Georgantopoulos, I., Goodall, C.V., Gondhalekar, P.M., Gourlay, J.A., Harris, A.W., Hassall, B.J.M., Hellier, C., Hodgkin, S., Jeffries, R.D., Kellett, B.J., Kent, B.J., Lieu, R., Lloyd, C., McGale, P., Mason, K.O., Matthews, L., Mittaz, J.P.D., Page, C.G., Pankiewicz, G.S., Pike, C.D., Ponman, T.J., Puchnarewicz, E.M., Pye, J.P., Quenby, J.J., Ricketts, M.J., Rosen, S.R., Sansom, A.E., Sembay, S., Sidher, S., Sims, M.R., Stewart, B.C., Sumner, T.J., Vallance, R.J., Watson, M.G., Warwick, R.S., Wells, A.A., Willingale, R., Willmore, A.P., Willoughby, G.A., Wonnacott, D., 1993. The ROSAT Wide Field Camera all-sky survey of extreme-ultraviolet sources. I. The bright source catalogue. MNRAS 260, 77–102. doi:10.1093/mnras/260.1.77.

Reeves, J.N., Turner, M.J.L., Bennie, P.J., Pounds, K.A., Short, A., O'Brien, P.T., Boller, T., Kuster, M., Tiengo, A., 2001. The first XMM-Newton spectrum of a high redshift quasar - PKS 0537-286. A&A 365, L116–L121. doi:10.1051/0004-6361:20000423, arXiv:astro-ph/0010367.

Remillard, R.A., McClintock, J.E., 2006. X-Ray Properties of Black-Hole Binaries. ARA&A 44, 49–92. doi:10.1146/annurev.astro.44.051905.092532, arXiv:astro-ph/0606352.

Reynolds, A.P., Parmar, A.N., Hakala, P.J., Pollock, A.M.T., Williams, O.R., Peacock, A., Taylor, B.G., 1999. The EXOSAT medium-energy slew survey catalog. A&AS 134, 287–300. doi:10.1051/aas:1999140, arXiv:astro-ph/9807318.

Rosenberg, F.D., Eyles, C.J., Skinner, G.K., Willmore, A.P., 1975. Observations of a transient X-ray source with a period of 104 S. Nature 256, 628–630. doi:10.1038/256628a0.

Rothschild, R., Boldt, E., Holt, S., Serlemitsos, P., Garmire, G., Agrawal, P., Riegler, G., Bowyer, S., Lampton, M., 1979. The cosmic X-ray experiment aboard HEAO-1. Space Science Instrumentation 4, 269–301.

Saxton, R.D., Read, A.M., Esquej, P., Freyberg, M.J., Altieri, B., Bermejo, D., 2008. The first XMM-Newton slew survey catalogue: XMMSL1. A&A 480, 611–622. doi:10.1051/0004-6361:20079193, arXiv:0801.3732.

Serlemitsos, P.J., Jalota, L., Soong, Y., Kunieda, H., Tawara, Y., Tsusaka, Y., Suzuki, H., Sakima, Y., Yamazaki, T., Yoshioka, H., Furuzawa, A., Yamashita, K., Awaki, H., Itoh, M., Ogasaka, Y., Honda, H., Uchibori, Y., 1995. The X-ray telescope on board ASCA. PASJ 47, 105–114.

SOC, E.X.N., 2020. Xmm-newton users handbook. URL: https://xmm-tools.cosmos.esa.int/external/xmm_user_support/documentation/uhb/. is. 2.18.

Sokolovsky, K.V., Li, K.L., Lopes de Oliveira, R., Ness, J.U., Mukai, K., Chomiuk, L., Aydi, E., Steinberg, E., Vurm, I., Metzger, B.D., Babul, A.N., Kawash, A., Linford, J.D., Nelson, T., Page, K.L., Rupen, M.P., Sokoloski, J.L., Strader, J., Kilkenny, D., 2021. The first nova eruption in a novalike variable: YZ Ret as seen in X-rays and gamma-rays. Submitted to MNRAS , arXiv:2108.03241 arXiv:2108.03241.

Strohmayer, T.E., 2001. Discovery of a 450 HZ Quasi-periodic Oscillation from the Microquasar GRO J1655-40 with the Rossi X-Ray Timing Explorer. ApJ 552, L49–L53. doi:10.1086/320258.

Strüder, L., Briel, U., Dennerl, K., Hartmann, R., Kendziorra, E., Meidinger, N., Pfeffermann, E., Reppin, C., Aschenbach, B., Bornemann, W., Bräuninger, H., Burkert, W., Elender, M., Freyberg, M., Haberl, F., Hartner, G., Heuschmann, F., Hippmann, H., Kastelic, E., Kemmer, S., Kettenring, G., Kink, W., Krause, N., Müller, S., Oppitz, A., Pietsch, W., Popp, M., Predehl, P., Read, A., Stephan, K.H., Stötter, D., Trümper, J., Holl, P., Kemmer, J., Soltau, H., Stötter, R., Weber, U., Weichert, U., von Zanthier, C., Carathanassis, D., Lutz, G., Richter, R.H., Solc, P., Böttcher,

H., Kuster, M., Staubert, R., Abbey, A., Holland, A., Turner, M., Balasini, M., Bignami, G.F., La Palombara, N., Villa, G., Buttler, W., Gianini, F., Lainé, R., Lumb, D., Dhez, P., 2001. The European Photon Imaging Camera on XMM-Newton: The pn-CCD camera. A&A 365, L18–L26. doi:10.1051/0004-6361:20000066.

Tanaka, Y., Inoue, H., Holt, S.S., 1994. The X-Ray Astronomy Satellite ASCA. PASJ 46, L37–L41.

Terrell, J., Fenimore, E.E., Klebesadel, R.W., Desai, U.D., 1982. Observation of two gamma-ray bursts by VELA X-ray detectors. ApJ 254, 279–286. doi:10.1086/159731.

Traulsen, I., Schwope, A.D., Lamer, G., Ballet, J., Carrera, F., Coriat, M., Freyberg, M.J., Michel, L., Motch, C., Rosen, S.R., Webb, N., Ceballos, M.T., Koliopanos, F., Kurpas, J., Page, M.J., Watson, M.G., 2019. The XMM-Newton serendipitous survey. VIII. The first XMM-Newton serenditous source catalogue from overlapping observations. A&A 624, A77. doi:10.1051/0004-6361/201833938, arXiv:1807.09178.

Traulsen, I., Schwope, A.D., Lamer, G., Ballet, J., Carrera, F.J., Ceballos, M.T., Coriat, M., Freyberg, M.J., Koliopanos, F., Kurpas, J., Michel, L., Motch, C., Page, M.J., Watson, M.G., Webb, N.A., 2020. The XMM-Newton serendipitous survey. X. The second source catalogue from overlapping XMM-Newton observations and its long-term variable content. A&A 641, A137. doi:10.1051/0004-6361/202037706, arXiv:2007.02932.

Trümper, J., 1982. The ROSAT mission. Advances in Space Research 2, 241–249. doi:10.1016/0273-1177(82)90070-9.

Tsusaka, Y., Suzuki, H., Yamashita, K., Kunieda, H., Tawara, Y., Ogasaka, Y., Uchibori, Y., Honda, H., Itoh, M., Awaki, H., Tsunemi, H., Hayashida, K., Nomoto, S., Wada, M., Miyata, E., Serlemitsos, P.J., Jalota, L., Soong, Y., 1995. Characterization of the Advanced Satellite for Cosmology and Astrophysics x-ray telescope: preflight calibration and ray tracing. Appl. Opt. 34, 4848–4856. doi:10.1364/AO.34.004848.

Turner, M.J.L., Abbey, A., Arnaud, M., Balasini, M., Barbera, M., Belsole, E., Bennie, P.J., Bernard, J.P., Bignami, G.F., Boer, M., Briel, U., Butler, I., Cara, C., Chabaud, C., Cole, R., Collura, A., Conte, M., Cros, A., Denby, M., Dhez, P., Di Coco, G., Dowson, J., Ferrando, P., Ghizzardi, S., Gianotti, F., Goodall, C.V., Gretton, L., Griffiths, R.G., Hainaut, O., Hochedez, J.F., Holland, A.D., Jourdain, E., Kendziorra, E., Lagostina, A., Laine, R., La Palombara, N., Lortholary, M., Lumb, D., Marty, P., Molendi, S., Pigot, C., Poindron, E., Pounds, K.A., Reeves, J.N., Reppin, C., Rothenflug, R., Salvetat, P., Sauvageot, J.L., Schmitt, D., Sembay, S., Short, A.D.T., Spragg, J., Stephen, J., Strüder, L., Tiengo, A., Trifoglio, M., Trümper, J., Vercellone, S., Vigroux, L., Villa, G., Ward, M.J., Whitehead, S., Zonca, E., 2001. The European Photon Imaging Camera on XMM-Newton: The MOS cameras. A&A 365, L27–L35. doi:10.1051/0004-6361:20000087, arXiv:astro-ph/0011498.

Turner, M.J.L., Smith, A., Zimmermann, H.U., 1981. The medium energy instrument on EXOSAT. Space Sci. Rev. 30, 513–524. doi:10.1007/BF01246071.

Turner, M.J.L., Thomas, H.D., Patchett, B.E., Reading, D.H., Makishima, K., Ohashi, T., Dotani, T., Hayashida, K., Inoue, H., Kondo, H., Koyama, K., Mitsusa, K., Ogawara, Y., Takano, S., Awaki, H., Tawara, Y., Nakamura, N., 1989. The large area counter on GINGA. PASJ 41, 345–372.

Ubertini, P., Lebrun, F., Di Cocco, G., Bazzano, A., Bird, A.J., Broenstad, K., Goldwurm, A., La Rosa, G., Labanti, C., Laurent, P., Mirabel, I.F., Quadrini, E.M., Ramsey, B., Reglero, V., Sabau, L., Sacco, B., Staubert, R., Vigroux, L., Weisskopf, M.C., Zdziarski, A.A., 2003. IBIS: The Imager on-board INTEGRAL. A&A 411, L131–L139. doi:10.1051/0004-6361:20031224.

Ueda, Y., Ishisaki, Y., Takahashi, T., Makishima, K., Ohashi, T., 2001. The ASCA Medium Sensitivity Survey (the GIS Catalog Project): Source Catalog. ApJS 133, 1–52. doi:10.1086/319189, arXiv:astro-ph/9908128.

Ueda, Y., Ishisaki, Y., Takahashi, T., Makishima, K., Ohashi, T., 2005. The ASCA Medium Sensitivity Survey (The GIS Catalog Project): Source Catalog II. ApJS 161, 185–223. doi:10.1086/468187.

Villa, G., Page, C.G., Turner, M.J.L., Cooke, B.A., Ricketts, M.J., Pounds, K.A., Adams, D.J., 1976. The Ariel V Sky Survey Instrument and new observations of the Milky Way. MNRAS 176, 609–620. doi:10.1093/mnras/176.3.609.

Warwick, R.S., Marshall, N., Fraser, G.W., Watson, M.G., Lawrence, A., Page, C.G., Pounds, K.A., Ricketts, M.J., Sims, M.R., Smith, A., 1981. The Ariel V /3 A/ catalogue of X-ray sources. I - Sources at low galactic latitude /absolute value of B less than 10 deg/. MNRAS 197, 865–891. doi:10.1093/mnras/197.4.865.

Webb, N.A., Coriat, M., Traulsen, I., Ballet, J., Motch, C., Carrera, F.J., Koliopanos, F., Authier, J., de la Calle, I., Ceballos, M.T., Colomo, E., Chuard, D., Freyberg, M., Garcia, T., Kolehmainen, M., Lamer, G., Lin, D., Maggi, P., Michel, L., Page, C.G., Page, M.J., Perea-Calderon, J.V., Pineau, F.X., Rodriguez, P., Rosen, S.R., Santos Lleo, M., Saxton, R.D., Schwope, A., Tomás, L., Watson, M.G., Zakardjian, A., 2020. The XMM-Newton serendipitous survey. IX. The fourth XMM-Newton serendipitous source catalogue. A&A 641, A136. doi:10.1051/0004-6361/201937353, arXiv:2007.02899.

Wells, D.C., Greisen, E.W., Harten, R.H., 1981. FITS - a Flexible Image Transport System. A&AS 44, 363.

White, N.E., Peacock, A., 1988. The EXOSAT observatory. Mem. S.A.It. 59, 7–31.

Whitlock, L., Lochner, J., Rhode, K., 1992a. The Ariel 5 and Vela 5B All-Sky Monitor Databases. Legacy 2. URL: https://heasarc.gsfc.nasa.gov/docs/journal/ariel2.html.

Whitlock, L., Lochner, J., Rhode, K., 1992b. Vela 5B ASM Calibration Guide. Technical Report. Laboratory of High Energy Astrophysics, Office of Guest Observer Programmes, NASA GSFC, Greenbelt. https://heasarc.gsfc.nasa.gov/FTP/vela5b/doc/doctex/.

Wilson, C.A., Finger, M.H., Coe, M.J., Laycock, S., Fabregat, J., 2002. A Decade in the Life of EXO 2030+375: A Multiwavelength Study of an Accreting X-Ray Pulsar. ApJ 570, 287–302. doi:10.1086/339739, arXiv:astro-ph/0201227.

Winkler, C., Courvoisier, T.J.L., Di Cocco, G., Gehrels, N., Giménez, A., Grebenev, S., Hermsen, W., Mas-Hesse, J.M., Lebrun, F., Lund, N., Palumbo, G.G.C., Paul, J., Roques, J.P., Schnopper, H., Schönfelder, V., Sunyaev, R., Teegarden, B., Ubertini, P., Vedrenne, G., Dean, A.J., 2003. The INTEGRAL mission. A&A 411, L1–L6. doi:10.1051/0004-6361:20031288.

Wood, K.S., Meekins, J.F., Yentis, D.J., Smathers, H.W., McNutt, D.P., Bleach, R.D., Byram, E.T., Chupp, T.A., Friedman, H., Meidav, M., 1984. The HEAO A-1 X-ray source catalog. ApJS 56, 507–649. doi:10.1086/190992.

Zimmermann, U., Boese, G., Becker, W., Belloni, T., Döbereiner, S., Izzo, C., Kahabka, P., Schwentker, O., 1998. EXSAS User's Guide. Technical Report 1. Max-Planck-Institut für Extraterrestrische Physik. 85740 Garching bei München, Germany. ftp://ftp.xray.mpe.mpg.de/people/mjf/2RXS/exsas_guide-980708.pdf.

Appendix A. Appendix

Table A.2: Pixel positions for the footprint definition of the *EXOSAT* LE CMA1 and CMA2 images that have an octagonal shape. The images have a size of 2048×2048 pixels.

Shape	Pixel position of the footprint (RAWX/RAWY)				Number of images
CMA1	124/902	149/1278	921/2048	1181/2013	1479/2037	81.1%
(e.g., Fig. 9a)	2048/1464	2048/773	1435/226	886/112		
CMA2	1/512	1/1427	590/2048	1452/2048		10.9%
(e.g., Fig. 9b)	2048/1520	2048/547	1530/1	537/1		

Table A.3: Conversion factors (CFs) in $\mathrm{erg\,cm^{-2}cnt^{-1}}$, computed with PIMMS version 4.11a (Mukai, 1993) or, in case of *Vela 5B*, *Uhuru*, *Ariel V* and *HEAO-1*, inferred from the lightcurve FITS files (Sect. 3.1), Forman et al. (1978, see also Sect. 3.2), Kaluzienski (1977, Sect. 3.3), and Wood et al. (1984); Nugent et al. (1983, Sect. 3.4), respectively. These conversion factors were extrapolated to the HILIGT energy bands using Eq. 5. Note that for the hard band of *HEAO-1* A2 the conversion factors do not have a unit as HILIGT receives already converted fluxes (Piccinotti et al., 1982) and only extrapolated to the 2–12 keV band. In the case of *Ariel V* ASM the error is only the systematic error of Kaluzienski (1977, p. 106), while an additional statistical error on each lightcurve point is added in quadrature. "plaw" denotes a powerlaw with a slope specified in the index column. "bbody" denotes a black body model with a temperature defined in units of keV in the index column.

Mission	Filter	Model	Index	N_H [cm^{-2}]	CF for 0.2–2 keV	CF for 2–12 keV	CF for 0.2–12 keV
ROSAT-PSPC	Open	plaw	0.5	$1 \cdot 10^{20}$	$1.166 \cdot 10^{-11}$	–	–
ROSAT-PSPC	Open	plaw	1.0	$1 \cdot 10^{20}$	$1.044 \cdot 10^{-11}$	–	–
ROSAT-PSPC	Open	plaw	1.5	$1 \cdot 10^{20}$	$8.863 \cdot 10^{-12}$	–	–
ROSAT-PSPC	Open	plaw	1.7	$1 \cdot 10^{20}$	$8.158 \cdot 10^{-12}$	–	–
ROSAT-PSPC	Open	plaw	2.0	$1 \cdot 10^{20}$	$7.076 \cdot 10^{-12}$	–	–
ROSAT-PSPC	Open	plaw	2.5	$1 \cdot 10^{20}$	$5.391 \cdot 10^{-12}$	–	–
ROSAT-PSPC	Open	plaw	3.0	$1 \cdot 10^{20}$	$4.045 \cdot 10^{-12}$	–	–
ROSAT-PSPC	Open	plaw	3.5	$1 \cdot 10^{20}$	$3.068 \cdot 10^{-12}$	–	–
ROSAT-PSPC	Open	bbody	0.06	$1 \cdot 10^{20}$	$3.340 \cdot 10^{-12}$	–	–
ROSAT-PSPC	Open	bbody	0.1	$1 \cdot 10^{20}$	$6.976 \cdot 10^{-12}$	–	–
ROSAT-PSPC	Open	bbody	0.3	$1 \cdot 10^{20}$	$1.059 \cdot 10^{-11}$	–	–
ROSAT-PSPC	Open	bbody	1.0	$1 \cdot 10^{20}$	$1.302 \cdot 10^{-11}$	–	–
ROSAT-PSPC	Open	plaw	0.5	$3 \cdot 10^{20}$	$1.239 \cdot 10^{-11}$	–	–
ROSAT-PSPC	Open	plaw	1.0	$3 \cdot 10^{20}$	$1.179 \cdot 10^{-11}$	–	–
ROSAT-PSPC	Open	plaw	1.5	$3 \cdot 10^{20}$	$1.111 \cdot 10^{-11}$	–	–
ROSAT-PSPC	Open	plaw	1.7	$3 \cdot 10^{20}$	$1.079 \cdot 10^{-11}$	–	–
ROSAT-PSPC	Open	plaw	2.0	$3 \cdot 10^{20}$	$1.024 \cdot 10^{-11}$	–	–
ROSAT-PSPC	Open	plaw	2.5	$3 \cdot 10^{20}$	$9.100 \cdot 10^{-12}$	–	–
ROSAT-PSPC	Open	plaw	3.0	$3 \cdot 10^{20}$	$7.783 \cdot 10^{-12}$	–	–
ROSAT-PSPC	Open	plaw	3.5	$3 \cdot 10^{20}$	$6.475 \cdot 10^{-12}$	–	–
ROSAT-PSPC	Open	bbody	0.06	$3 \cdot 10^{20}$	$6.099 \cdot 10^{-12}$	–	–
ROSAT-PSPC	Open	bbody	0.1	$3 \cdot 10^{20}$	$1.096 \cdot 10^{-11}$	–	–
ROSAT-PSPC	Open	bbody	0.3	$3 \cdot 10^{20}$	$1.096 \cdot 10^{-11}$	–	–
ROSAT-PSPC	Open	bbody	1.0	$3 \cdot 10^{20}$	$1.318 \cdot 10^{-11}$	–	–
ROSAT-PSPC	Open	plaw	0.5	$1 \cdot 10^{21}$	$1.271 \cdot 10^{-11}$	–	–
ROSAT-PSPC	Open	plaw	1.0	$1 \cdot 10^{21}$	$1.232 \cdot 10^{-11}$	–	–
ROSAT-PSPC	Open	plaw	1.5	$1 \cdot 10^{21}$	$1.210 \cdot 10^{-11}$	–	–
ROSAT-PSPC	Open	plaw	1.7	$1 \cdot 10^{21}$	$1.207 \cdot 10^{-11}$	–	–
ROSAT-PSPC	Open	plaw	2.0	$1 \cdot 10^{21}$	$1.208 \cdot 10^{-11}$	–	–
ROSAT-PSPC	Open	plaw	2.5	$1 \cdot 10^{21}$	$1.228 \cdot 10^{-11}$	–	–
ROSAT-PSPC	Open	plaw	3.0	$1 \cdot 10^{21}$	$1.267 \cdot 10^{-11}$	–	–
ROSAT-PSPC	Open	plaw	3.5	$1 \cdot 10^{21}$	$1.315 \cdot 10^{-11}$	–	–
ROSAT-PSPC	Open	bbody	0.06	$1 \cdot 10^{21}$	$1.946 \cdot 10^{-11}$	–	–
ROSAT-PSPC	Open	bbody	0.1	$1 \cdot 10^{21}$	$1.571 \cdot 10^{-11}$	–	–
ROSAT-PSPC	Open	bbody	0.3	$1 \cdot 10^{21}$	$1.095 \cdot 10^{-11}$	–	–
ROSAT-PSPC	Open	bbody	1.0	$1 \cdot 10^{21}$	$1.337 \cdot 10^{-11}$	–	–
ROSAT-HRI	–	plaw	0.5	$1 \cdot 10^{20}$	$3.382 \cdot 10^{-11}$	–	–
ROSAT-HRI	–	plaw	1.0	$1 \cdot 10^{20}$	$3.201 \cdot 10^{-11}$	–	–
ROSAT-HRI	–	plaw	1.5	$1 \cdot 10^{20}$	$3.019 \cdot 10^{-11}$	–	–
ROSAT-HRI	–	plaw	1.7	$1 \cdot 10^{20}$	$2.939 \cdot 10^{-11}$	–	–
ROSAT-HRI	–	plaw	2.0	$1 \cdot 10^{20}$	$2.802 \cdot 10^{-11}$	–	–
ROSAT-HRI	–	plaw	2.5	$1 \cdot 10^{20}$	$2.525 \cdot 10^{-11}$	–	–
ROSAT-HRI	–	plaw	3.0	$1 \cdot 10^{20}$	$2.206 \cdot 10^{-11}$	–	–
ROSAT-HRI	–	plaw	3.5	$1 \cdot 10^{20}$	$1.884 \cdot 10^{-11}$	–	–
ROSAT-HRI	–	bbody	0.06	$1 \cdot 10^{20}$	$2.059 \cdot 10^{-11}$	–	–
ROSAT-HRI	–	bbody	0.1	$1 \cdot 10^{20}$	$3.165 \cdot 10^{-11}$	–	–

ROSAT-HRI	–	bbody	0.3	$1 \cdot 10^{20}$	$2.905 \cdot 10^{-11}$	–	–
ROSAT-HRI	–	bbody	1.0	$1 \cdot 10^{20}$	$3.648 \cdot 10^{-11}$	–	–
ROSAT-HRI	–	plaw	0.5	$3 \cdot 10^{20}$	$3.442 \cdot 10^{-11}$	–	–
ROSAT-HRI	–	plaw	1.0	$3 \cdot 10^{20}$	$3.309 \cdot 10^{-11}$	–	–
ROSAT-HRI	–	plaw	1.5	$3 \cdot 10^{20}$	$3.224 \cdot 10^{-11}$	–	–
ROSAT-HRI	–	plaw	1.7	$3 \cdot 10^{20}$	$3.200 \cdot 10^{-11}$	–	–
ROSAT-HRI	–	plaw	2.0	$3 \cdot 10^{20}$	$3.171 \cdot 10^{-11}$	–	–
ROSAT-HRI	–	plaw	2.5	$3 \cdot 10^{20}$	$3.115 \cdot 10^{-11}$	–	–
ROSAT-HRI	–	plaw	3.0	$3 \cdot 10^{20}$	$3.018 \cdot 10^{-11}$	–	–
ROSAT-HRI	–	plaw	3.5	$3 \cdot 10^{20}$	$2.855 \cdot 10^{-11}$	–	–
ROSAT-HRI	–	bbody	0.06	$3 \cdot 10^{20}$	$2.997 \cdot 10^{-11}$	–	–
ROSAT-HRI	–	bbody	0.1	$3 \cdot 10^{20}$	$3.857 \cdot 10^{-11}$	–	–
ROSAT-HRI	–	bbody	0.3	$3 \cdot 10^{20}$	$2.911 \cdot 10^{-11}$	–	–
ROSAT-HRI	–	bbody	1.0	$3 \cdot 10^{20}$	$3.672 \cdot 10^{-11}$	–	–
ROSAT-HRI	–	plaw	0.5	$1 \cdot 10^{21}$	$3.480 \cdot 10^{-11}$	–	–
ROSAT-HRI	–	plaw	1.0	$1 \cdot 10^{21}$	$3.329 \cdot 10^{-11}$	–	–
ROSAT-HRI	–	plaw	1.5	$1 \cdot 10^{21}$	$3.239 \cdot 10^{-11}$	–	–
ROSAT-HRI	–	plaw	1.7	$1 \cdot 10^{21}$	$3.222 \cdot 10^{-11}$	–	–
ROSAT-HRI	–	plaw	2.0	$1 \cdot 10^{21}$	$3.217 \cdot 10^{-11}$	–	–
ROSAT-HRI	–	plaw	2.5	$1 \cdot 10^{21}$	$3.266 \cdot 10^{-11}$	–	–
ROSAT-HRI	–	plaw	3.0	$1 \cdot 10^{21}$	$3.383 \cdot 10^{-11}$	–	–
ROSAT-HRI	–	plaw	3.5	$1 \cdot 10^{21}$	$3.552 \cdot 10^{-11}$	–	–
ROSAT-HRI	–	bbody	0.06	$1 \cdot 10^{21}$	$5.120 \cdot 10^{-11}$	–	–
ROSAT-HRI	–	bbody	0.1	$1 \cdot 10^{21}$	$4.226 \cdot 10^{-11}$	–	–
ROSAT-HRI	–	bbody	0.3	$1 \cdot 10^{21}$	$2.863 \cdot 10^{-11}$	–	–
ROSAT-HRI	–	bbody	1.0	$1 \cdot 10^{21}$	$3.734 \cdot 10^{-11}$	–	–
EXOSAT-LE	3Lx	plaw	0.5	$1 \cdot 10^{20}$	$6.393 \cdot 10^{-10}$	–	–
EXOSAT-LE	3Lx	plaw	1.0	$1 \cdot 10^{20}$	$4.390 \cdot 10^{-10}$	–	–
EXOSAT-LE	3Lx	plaw	1.5	$1 \cdot 10^{20}$	$2.863 \cdot 10^{-10}$	–	–
EXOSAT-LE	3Lx	plaw	1.7	$1 \cdot 10^{20}$	$2.396 \cdot 10^{-10}$	–	–
EXOSAT-LE	3Lx	plaw	2.0	$1 \cdot 10^{20}$	$1.834 \cdot 10^{-10}$	–	–
EXOSAT-LE	3Lx	plaw	2.5	$1 \cdot 10^{20}$	$1.193 \cdot 10^{-10}$	–	–
EXOSAT-LE	3Lx	plaw	3.0	$1 \cdot 10^{20}$	$8.038 \cdot 10^{-11}$	–	–
EXOSAT-LE	3Lx	plaw	3.5	$1 \cdot 10^{20}$	$5.645 \cdot 10^{-11}$	–	–
EXOSAT-LE	3Lx	bbody	0.06	$1 \cdot 10^{20}$	$6.816 \cdot 10^{-11}$	–	–
EXOSAT-LE	3Lx	bbody	0.1	$1 \cdot 10^{20}$	$1.412 \cdot 10^{-10}$	–	–
EXOSAT-LE	3Lx	bbody	0.3	$1 \cdot 10^{20}$	$5.368 \cdot 10^{-10}$	–	–
EXOSAT-LE	3Lx	bbody	1.0	$1 \cdot 10^{20}$	$1.069 \cdot 10^{-9}$	–	–
EXOSAT-LE	3Lx	plaw	0.5	$3 \cdot 10^{20}$	$8.053 \cdot 10^{-10}$	–	–
EXOSAT-LE	3Lx	plaw	1.0	$3 \cdot 10^{20}$	$6.268 \cdot 10^{-10}$	–	–
EXOSAT-LE	3Lx	plaw	1.5	$3 \cdot 10^{20}$	$4.733 \cdot 10^{-10}$	–	–
EXOSAT-LE	3Lx	plaw	1.7	$3 \cdot 10^{20}$	$4.207 \cdot 10^{-10}$	–	–
EXOSAT-LE	3Lx	plaw	2.0	$3 \cdot 10^{20}$	$3.518 \cdot 10^{-10}$	–	–
EXOSAT-LE	3Lx	plaw	2.5	$3 \cdot 10^{20}$	$2.620 \cdot 10^{-10}$	–	–
EXOSAT-LE	3Lx	plaw	3.0	$3 \cdot 10^{20}$	$1.984 \cdot 10^{-10}$	–	–
EXOSAT-LE	3Lx	plaw	3.5	$3 \cdot 10^{20}$	$1.542 \cdot 10^{-10}$	–	–
EXOSAT-LE	3Lx	bbody	0.06	$3 \cdot 10^{20}$	$1.267 \cdot 10^{-10}$	–	–
EXOSAT-LE	3Lx	bbody	0.1	$3 \cdot 10^{20}$	$2.159 \cdot 10^{-10}$	–	–
EXOSAT-LE	3Lx	bbody	0.3	$3 \cdot 10^{20}$	$6.249 \cdot 10^{-10}$	–	–
EXOSAT-LE	3Lx	bbody	1.0	$3 \cdot 10^{20}$	$1.143 \cdot 10^{-9}$	–	–
EXOSAT-LE	3Lx	plaw	0.5	$1 \cdot 10^{21}$	$1.002 \cdot 10^{-9}$	–	–
EXOSAT-LE	3Lx	plaw	1.0	$1 \cdot 10^{21}$	$8.504 \cdot 10^{-10}$	–	–
EXOSAT-LE	3Lx	plaw	1.5	$1 \cdot 10^{21}$	$7.126 \cdot 10^{-10}$	–	–
EXOSAT-LE	3Lx	plaw	1.7	$1 \cdot 10^{21}$	$6.626 \cdot 10^{-10}$	–	–
EXOSAT-LE	3Lx	plaw	2.0	$1 \cdot 10^{21}$	$5.937 \cdot 10^{-10}$	–	–
EXOSAT-LE	3Lx	plaw	2.5	$1 \cdot 10^{21}$	$4.958 \cdot 10^{-10}$	–	–
EXOSAT-LE	3Lx	plaw	3.0	$1 \cdot 10^{21}$	$4.182 \cdot 10^{-10}$	–	–
EXOSAT-LE	3Lx	plaw	3.5	$1 \cdot 10^{21}$	$3.581 \cdot 10^{-10}$	–	–
EXOSAT-LE	3Lx	bbody	0.06	$1 \cdot 10^{21}$	$2.326 \cdot 10^{-10}$	–	–
EXOSAT-LE	3Lx	bbody	0.1	$1 \cdot 10^{21}$	$3.129 \cdot 10^{-10}$	–	–
EXOSAT-LE	3Lx	bbody	0.3	$1 \cdot 10^{21}$	$7.473 \cdot 10^{-10}$	–	–
EXOSAT-LE	3Lx	bbody	1.0	$1 \cdot 10^{21}$	$1.262 \cdot 10^{-9}$	–	–
EXOSAT-LE	4LX	plaw	0.5	$1 \cdot 10^{20}$	$7.102 \cdot 10^{-10}$	–	–
EXOSAT-LE	4LX	plaw	1.0	$1 \cdot 10^{20}$	$4.960 \cdot 10^{-10}$	–	–
EXOSAT-LE	4LX	plaw	1.5	$1 \cdot 10^{20}$	$3.270 \cdot 10^{-10}$	–	–
EXOSAT-LE	4LX	plaw	1.7	$1 \cdot 10^{20}$	$2.745 \cdot 10^{-10}$	–	–
EXOSAT-LE	4LX	plaw	2.0	$1 \cdot 10^{20}$	$2.107 \cdot 10^{-10}$	–	–
EXOSAT-LE	4LX	plaw	2.5	$1 \cdot 10^{20}$	$1.373 \cdot 10^{-10}$	–	–
EXOSAT-LE	4LX	plaw	3.0	$1 \cdot 10^{20}$	$9.270 \cdot 10^{-11}$	–	–

EXOSAT-LE	4LX	plaw	3.5	$1 \cdot 10^{20}$	$6.523 \cdot 10^{-11}$	–	–
EXOSAT-LE	4LX	bbody	0.06	$1 \cdot 10^{20}$	$7.804 \cdot 10^{-11}$	–	–
EXOSAT-LE	4LX	bbody	0.1	$1 \cdot 10^{20}$	$1.651 \cdot 10^{-10}$	–	–
EXOSAT-LE	4LX	bbody	0.3	$1 \cdot 10^{20}$	$6.023 \cdot 10^{-10}$	–	–
EXOSAT-LE	4LX	bbody	1.0	$1 \cdot 10^{20}$	$1.142 \cdot 10^{-9}$	–	–
EXOSAT-LE	4LX	plaw	0.5	$3 \cdot 10^{20}$	$8.860 \cdot 10^{-10}$	–	–
EXOSAT-LE	4LX	plaw	1.0	$3 \cdot 10^{20}$	$7.033 \cdot 10^{-10}$	–	–
EXOSAT-LE	4LX	plaw	1.5	$3 \cdot 10^{20}$	$5.400 \cdot 10^{-10}$	–	–
EXOSAT-LE	4LX	plaw	1.7	$3 \cdot 10^{20}$	$4.825 \cdot 10^{-10}$	–	–
EXOSAT-LE	4LX	plaw	2.0	$3 \cdot 10^{20}$	$4.058 \cdot 10^{-10}$	–	–
EXOSAT-LE	4LX	plaw	2.5	$3 \cdot 10^{20}$	$3.037 \cdot 10^{-10}$	–	–
EXOSAT-LE	4LX	plaw	3.0	$3 \cdot 10^{20}$	$2.299 \cdot 10^{-10}$	–	–
EXOSAT-LE	4LX	plaw	3.5	$3 \cdot 10^{20}$	$1.779 \cdot 10^{-10}$	–	–
EXOSAT-LE	4LX	bbody	0.06	$3 \cdot 10^{20}$	$1.484 \cdot 10^{-10}$	–	–
EXOSAT-LE	4LX	bbody	0.1	$3 \cdot 10^{20}$	$2.588 \cdot 10^{-10}$	–	–
EXOSAT-LE	4LX	bbody	0.3	$3 \cdot 10^{20}$	$6.965 \cdot 10^{-10}$	–	–
EXOSAT-LE	4LX	bbody	1.0	$3 \cdot 10^{20}$	$1.214 \cdot 10^{-9}$	–	–
EXOSAT-LE	4LX	plaw	0.5	$1 \cdot 10^{21}$	$1.077 \cdot 10^{-9}$	–	–
EXOSAT-LE	4LX	plaw	1.0	$1 \cdot 10^{21}$	$9.300 \cdot 10^{-10}$	–	–
EXOSAT-LE	4LX	plaw	1.5	$1 \cdot 10^{21}$	$7.944 \cdot 10^{-10}$	–	–
EXOSAT-LE	4LX	plaw	1.7	$1 \cdot 10^{21}$	$7.446 \cdot 10^{-10}$	–	–
EXOSAT-LE	4LX	plaw	2.0	$1 \cdot 10^{21}$	$6.752 \cdot 10^{-10}$	–	–
EXOSAT-LE	4LX	plaw	2.5	$1 \cdot 10^{21}$	$5.750 \cdot 10^{-10}$	–	–
EXOSAT-LE	4LX	plaw	3.0	$1 \cdot 10^{21}$	$4.937 \cdot 10^{-10}$	–	–
EXOSAT-LE	4LX	plaw	3.5	$1 \cdot 10^{21}$	$4.292 \cdot 10^{-10}$	–	–
EXOSAT-LE	4LX	bbody	0.06	$1 \cdot 10^{21}$	$2.943 \cdot 10^{-10}$	–	–
EXOSAT-LE	4LX	bbody	0.1	$1 \cdot 10^{21}$	$3.796 \cdot 10^{-10}$	–	–
EXOSAT-LE	4LX	bbody	0.3	$1 \cdot 10^{21}$	$8.153 \cdot 10^{-10}$	–	–
EXOSAT-LE	4LX	bbody	1.0	$1 \cdot 10^{21}$	$1.322 \cdot 10^{-9}$	–	–
EXOSAT-LE	Al/p	plaw	0.5	$1 \cdot 10^{20}$	$1.014 \cdot 10^{-9}$	–	–
EXOSAT-LE	Al/p	plaw	1.0	$1 \cdot 10^{20}$	$7.893 \cdot 10^{-10}$	–	–
EXOSAT-LE	Al/p	plaw	1.5	$1 \cdot 10^{20}$	$6.034 \cdot 10^{-10}$	–	–
EXOSAT-LE	Al/p	plaw	1.7	$1 \cdot 10^{20}$	$5.412 \cdot 10^{-10}$	–	–
EXOSAT-LE	Al/p	plaw	2.0	$1 \cdot 10^{20}$	$4.606 \cdot 10^{-10}$	–	–
EXOSAT-LE	Al/p	plaw	2.5	$1 \cdot 10^{20}$	$3.567 \cdot 10^{-10}$	–	–
EXOSAT-LE	Al/p	plaw	3.0	$1 \cdot 10^{20}$	$2.830 \cdot 10^{-10}$	–	–
EXOSAT-LE	Al/p	plaw	3.5	$1 \cdot 10^{20}$	$2.301 \cdot 10^{-10}$	–	–
EXOSAT-LE	Al/p	bbody	0.06	$1 \cdot 10^{20}$	$2.290 \cdot 10^{-10}$	–	–
EXOSAT-LE	Al/p	bbody	0.1	$1 \cdot 10^{20}$	$3.207 \cdot 10^{-10}$	–	–
EXOSAT-LE	Al/p	bbody	0.3	$1 \cdot 10^{20}$	$7.871 \cdot 10^{-10}$	–	–
EXOSAT-LE	Al/p	bbody	1.0	$1 \cdot 10^{20}$	$1.464 \cdot 10^{-9}$	–	–
EXOSAT-LE	Al/p	plaw	0.5	$3 \cdot 10^{20}$	$1.120 \cdot 10^{-9}$	–	–
EXOSAT-LE	Al/p	plaw	1.0	$3 \cdot 10^{20}$	$9.101 \cdot 10^{-10}$	–	–
EXOSAT-LE	Al/p	plaw	1.5	$3 \cdot 10^{20}$	$7.321 \cdot 10^{-10}$	–	–
EXOSAT-LE	Al/p	plaw	1.7	$3 \cdot 10^{20}$	$6.710 \cdot 10^{-10}$	–	–
EXOSAT-LE	Al/p	plaw	2.0	$3 \cdot 10^{20}$	$5.905 \cdot 10^{-10}$	–	–
EXOSAT-LE	Al/p	plaw	2.5	$3 \cdot 10^{20}$	$4.838 \cdot 10^{-10}$	–	–
EXOSAT-LE	Al/p	plaw	3.0	$3 \cdot 10^{20}$	$4.061 \cdot 10^{-10}$	–	–
EXOSAT-LE	Al/p	plaw	3.5	$3 \cdot 10^{20}$	$3.501 \cdot 10^{-10}$	–	–
EXOSAT-LE	Al/p	bbody	0.06	$3 \cdot 10^{20}$	$2.885 \cdot 10^{-10}$	–	–
EXOSAT-LE	Al/p	bbody	0.1	$3 \cdot 10^{20}$	$3.669 \cdot 10^{-10}$	–	–
EXOSAT-LE	Al/p	bbody	0.3	$3 \cdot 10^{20}$	$8.451 \cdot 10^{-10}$	–	–
EXOSAT-LE	Al/p	bbody	1.0	$3 \cdot 10^{20}$	$1.525 \cdot 10^{-9}$	–	–
EXOSAT-LE	Al/p	plaw	0.5	$1 \cdot 10^{21}$	$1.316 \cdot 10^{-9}$	–	–
EXOSAT-LE	Al/p	plaw	1.0	$1 \cdot 10^{21}$	$1.117 \cdot 10^{-9}$	–	–
EXOSAT-LE	Al/p	plaw	1.5	$1 \cdot 10^{21}$	$9.399 \cdot 10^{-10}$	–	–
EXOSAT-LE	Al/p	plaw	1.7	$1 \cdot 10^{21}$	$8.764 \cdot 10^{-10}$	–	–
EXOSAT-LE	Al/p	plaw	2.0	$1 \cdot 10^{21}$	$7.899 \cdot 10^{-10}$	–	–
EXOSAT-LE	Al/p	plaw	2.5	$1 \cdot 10^{21}$	$6.688 \cdot 10^{-10}$	–	–
EXOSAT-LE	Al/p	plaw	3.0	$1 \cdot 10^{21}$	$5.749 \cdot 10^{-10}$	–	–
EXOSAT-LE	Al/p	plaw	3.5	$1 \cdot 10^{21}$	$5.042 \cdot 10^{-10}$	–	–
EXOSAT-LE	Al/p	bbody	0.06	$1 \cdot 10^{21}$	$3.473 \cdot 10^{-10}$	–	–
EXOSAT-LE	Al/p	bbody	0.1	$1 \cdot 10^{21}$	$4.238 \cdot 10^{-10}$	–	–
EXOSAT-LE	Al/p	bbody	0.3	$1 \cdot 10^{21}$	$9.689 \cdot 10^{-10}$	–	–
EXOSAT-LE	Al/p	bbody	1.0	$1 \cdot 10^{21}$	$1.666 \cdot 10^{-9}$	–	–
EXOSAT-LE	Bor	plaw	0.5	$1 \cdot 10^{20}$	$1.909 \cdot 10^{-9}$	–	–
EXOSAT-LE	Bor	plaw	1.0	$1 \cdot 10^{20}$	$1.882 \cdot 10^{-9}$	–	–
EXOSAT-LE	Bor	plaw	1.5	$1 \cdot 10^{20}$	$1.837 \cdot 10^{-9}$	–	–
EXOSAT-LE	Bor	plaw	1.7	$1 \cdot 10^{20}$	$1.801 \cdot 10^{-9}$	–	–

EXOSAT-LE	Bor	plaw	2.0	$1 \cdot 10^{20}$	$1.716 \cdot 10^{-9}$	–	–
EXOSAT-LE	Bor	plaw	2.5	$1 \cdot 10^{20}$	$1.479 \cdot 10^{-9}$	–	–
EXOSAT-LE	Bor	plaw	3.0	$1 \cdot 10^{20}$	$1.165 \cdot 10^{-9}$	–	–
EXOSAT-LE	Bor	plaw	3.5	$1 \cdot 10^{20}$	$8.660 \cdot 10^{-10}$	–	–
EXOSAT-LE	Bor	bbody	0.06	$1 \cdot 10^{20}$	$1.574 \cdot 10^{-9}$	–	–
EXOSAT-LE	Bor	bbody	0.1	$1 \cdot 10^{20}$	$2.688 \cdot 10^{-9}$	–	–
EXOSAT-LE	Bor	bbody	0.3	$1 \cdot 10^{20}$	$1.757 \cdot 10^{-9}$	–	–
EXOSAT-LE	Bor	bbody	1.0	$1 \cdot 10^{20}$	$1.945 \cdot 10^{-9}$	–	–
EXOSAT-LE	Bor	plaw	0.5	$3 \cdot 10^{20}$	$1.923 \cdot 10^{-9}$	–	–
EXOSAT-LE	Bor	plaw	1.0	$3 \cdot 10^{20}$	$1.934 \cdot 10^{-9}$	–	–
EXOSAT-LE	Bor	plaw	1.5	$3 \cdot 10^{20}$	$1.998 \cdot 10^{-9}$	–	–
EXOSAT-LE	Bor	plaw	1.7	$3 \cdot 10^{20}$	$2.042 \cdot 10^{-9}$	–	–
EXOSAT-LE	Bor	plaw	2.0	$3 \cdot 10^{20}$	$2.130 \cdot 10^{-9}$	–	–
EXOSAT-LE	Bor	plaw	2.5	$3 \cdot 10^{20}$	$2.333 \cdot 10^{-9}$	–	–
EXOSAT-LE	Bor	plaw	3.0	$3 \cdot 10^{20}$	$2.578 \cdot 10^{-9}$	–	–
EXOSAT-LE	Bor	plaw	3.5	$3 \cdot 10^{20}$	$2.778 \cdot 10^{-9}$	–	–
EXOSAT-LE	Bor	bbody	0.06	$3 \cdot 10^{20}$	$6.247 \cdot 10^{-9}$	–	–
EXOSAT-LE	Bor	bbody	0.1	$3 \cdot 10^{20}$	$3.571 \cdot 10^{-9}$	–	–
EXOSAT-LE	Bor	bbody	0.3	$3 \cdot 10^{20}$	$1.740 \cdot 10^{-9}$	–	–
EXOSAT-LE	Bor	bbody	1.0	$3 \cdot 10^{20}$	$1.947 \cdot 10^{-9}$	–	–
EXOSAT-LE	Bor	plaw	0.5	$1 \cdot 10^{21}$	$1.888 \cdot 10^{-9}$	–	–
EXOSAT-LE	Bor	plaw	1.0	$1 \cdot 10^{21}$	$1.854 \cdot 10^{-9}$	–	–
EXOSAT-LE	Bor	plaw	1.5	$1 \cdot 10^{21}$	$1.849 \cdot 10^{-9}$	–	–
EXOSAT-LE	Bor	plaw	1.7	$1 \cdot 10^{21}$	$1.857 \cdot 10^{-9}$	–	–
EXOSAT-LE	Bor	plaw	2.0	$1 \cdot 10^{21}$	$1.883 \cdot 10^{-9}$	–	–
EXOSAT-LE	Bor	plaw	2.5	$1 \cdot 10^{21}$	$1.970 \cdot 10^{-9}$	–	–
EXOSAT-LE	Bor	plaw	3.0	$1 \cdot 10^{21}$	$2.122 \cdot 10^{-9}$	–	–
EXOSAT-LE	Bor	plaw	3.5	$1 \cdot 10^{21}$	$2.356 \cdot 10^{-9}$	–	–
EXOSAT-LE	Bor	bbody	0.06	$1 \cdot 10^{21}$	$5.867 \cdot 10^{-9}$	–	–
EXOSAT-LE	Bor	bbody	0.1	$1 \cdot 10^{21}$	$2.692 \cdot 10^{-9}$	–	–
EXOSAT-LE	Bor	bbody	0.3	$1 \cdot 10^{21}$	$1.677 \cdot 10^{-9}$	–	–
EXOSAT-LE	Bor	bbody	1.0	$1 \cdot 10^{21}$	$1.954 \cdot 10^{-9}$	–	–
EXOSAT-ME-SLEW	–	plaw	0.5	$1 \cdot 10^{20}$	–	$2.763 \cdot 10^{-11}$	–
EXOSAT-ME-SLEW	–	plaw	1.0	$1 \cdot 10^{20}$	–	$2.161 \cdot 10^{-11}$	–
EXOSAT-ME-SLEW	–	plaw	1.5	$1 \cdot 10^{20}$	–	$1.711 \cdot 10^{-11}$	–
EXOSAT-ME-SLEW	–	plaw	1.7	$1 \cdot 10^{20}$	–	$1.566 \cdot 10^{-11}$	–
EXOSAT-ME-SLEW	–	plaw	2.0	$1 \cdot 10^{20}$	–	$1.378 \cdot 10^{-11}$	–
EXOSAT-ME-SLEW	–	plaw	2.5	$1 \cdot 10^{20}$	–	$1.130 \cdot 10^{-11}$	–
EXOSAT-ME-SLEW	–	plaw	3.0	$1 \cdot 10^{20}$	–	$9.433 \cdot 10^{-12}$	–
EXOSAT-ME-SLEW	–	plaw	3.5	$1 \cdot 10^{20}$	–	$7.975 \cdot 10^{-12}$	–
EXOSAT-ME-SLEW	–	bbody	0.06	$1 \cdot 10^{20}$	–	$2.432 \cdot 10^{-16}$	–
EXOSAT-ME-SLEW	–	bbody	0.1	$1 \cdot 10^{20}$	–	$7.184 \cdot 10^{-14}$	–
EXOSAT-ME-SLEW	–	bbody	0.3	$1 \cdot 10^{20}$	–	$4.724 \cdot 10^{-12}$	–
EXOSAT-ME-SLEW	–	bbody	1.0	$1 \cdot 10^{20}$	–	$1.151 \cdot 10^{-11}$	–
EXOSAT-ME-SLEW	–	plaw	0.5	$3 \cdot 10^{20}$	–	$2.766 \cdot 10^{-11}$	–
EXOSAT-ME-SLEW	–	plaw	1.0	$3 \cdot 10^{20}$	–	$2.163 \cdot 10^{-11}$	–
EXOSAT-ME-SLEW	–	plaw	1.5	$3 \cdot 10^{20}$	–	$1.713 \cdot 10^{-11}$	–
EXOSAT-ME-SLEW	–	plaw	1.7	$3 \cdot 10^{20}$	–	$1.568 \cdot 10^{-11}$	–
EXOSAT-ME-SLEW	–	plaw	2.0	$3 \cdot 10^{20}$	–	$1.380 \cdot 10^{-11}$	–
EXOSAT-ME-SLEW	–	plaw	2.5	$3 \cdot 10^{20}$	–	$1.133 \cdot 10^{-11}$	–
EXOSAT-ME-SLEW	–	plaw	3.0	$3 \cdot 10^{20}$	–	$9.456 \cdot 10^{-12}$	–
EXOSAT-ME-SLEW	–	plaw	3.5	$3 \cdot 10^{20}$	–	$7.999 \cdot 10^{-12}$	–
EXOSAT-ME-SLEW	–	bbody	0.06	$3 \cdot 10^{20}$	–	$2.480 \cdot 10^{-16}$	–
EXOSAT-ME-SLEW	–	bbody	0.1	$3 \cdot 10^{20}$	–	$7.277 \cdot 10^{-14}$	–
EXOSAT-ME-SLEW	–	bbody	0.3	$3 \cdot 10^{20}$	–	$4.741 \cdot 10^{-12}$	–
EXOSAT-ME-SLEW	–	bbody	1.0	$3 \cdot 10^{20}$	–	$1.152 \cdot 10^{-11}$	–
EXOSAT-ME-SLEW	–	plaw	0.5	$1 \cdot 10^{21}$	–	$2.775 \cdot 10^{-11}$	–
EXOSAT-ME-SLEW	–	plaw	1.0	$1 \cdot 10^{21}$	–	$2.172 \cdot 10^{-11}$	–
EXOSAT-ME-SLEW	–	plaw	1.5	$1 \cdot 10^{21}$	–	$1.722 \cdot 10^{-11}$	–
EXOSAT-ME-SLEW	–	plaw	1.7	$1 \cdot 10^{21}$	–	$1.576 \cdot 10^{-11}$	–
EXOSAT-ME-SLEW	–	plaw	2.0	$1 \cdot 10^{21}$	–	$1.389 \cdot 10^{-11}$	–
EXOSAT-ME-SLEW	–	plaw	2.5	$1 \cdot 10^{21}$	–	$1.141 \cdot 10^{-11}$	–
EXOSAT-ME-SLEW	–	plaw	3.0	$1 \cdot 10^{21}$	–	$9.537 \cdot 10^{-12}$	–
EXOSAT-ME-SLEW	–	plaw	3.5	$1 \cdot 10^{21}$	–	$8.080 \cdot 10^{-12}$	–
EXOSAT-ME-SLEW	–	bbody	0.06	$1 \cdot 10^{21}$	–	$2.655 \cdot 10^{-16}$	–
EXOSAT-ME-SLEW	–	bbody	0.1	$1 \cdot 10^{21}$	–	$7.609 \cdot 10^{-14}$	–
EXOSAT-ME-SLEW	–	bbody	0.3	$1 \cdot 10^{21}$	–	$4.799 \cdot 10^{-12}$	–
EXOSAT-ME-SLEW	–	bbody	1.0	$1 \cdot 10^{21}$	–	$1.155 \cdot 10^{-11}$	–
EXOSAT-ME-PNT	–	plaw	0.5	$1 \cdot 10^{20}$	–	$2.214 \cdot 10^{-11}$	–

EXOSAT-ME-PNT	–	plaw	1.0	$1 \cdot 10^{20}$	–	$1.867 \cdot 10^{-11}$	–
EXOSAT-ME-PNT	–	plaw	1.5	$1 \cdot 10^{20}$	–	$1.562 \cdot 10^{-11}$	–
EXOSAT-ME-PNT	–	plaw	1.7	$1 \cdot 10^{20}$	–	$1.453 \cdot 10^{-11}$	–
EXOSAT-ME-PNT	–	plaw	2.0	$1 \cdot 10^{20}$	–	$1.305 \cdot 10^{-11}$	–
EXOSAT-ME-PNT	–	plaw	2.5	$1 \cdot 10^{20}$	–	$1.096 \cdot 10^{-11}$	–
EXOSAT-ME-PNT	–	plaw	3.0	$1 \cdot 10^{20}$	–	$9.275 \cdot 10^{-12}$	–
EXOSAT-ME-PNT	–	plaw	3.5	$1 \cdot 10^{20}$	–	$7.906 \cdot 10^{-12}$	–
EXOSAT-ME-PNT	–	bbody	0.06	$1 \cdot 10^{20}$	–	$2.432 \cdot 10^{-16}$	–
EXOSAT-ME-PNT	–	bbody	0.1	$1 \cdot 10^{20}$	–	$7.184 \cdot 10^{-14}$	–
EXOSAT-ME-PNT	–	bbody	0.3	$1 \cdot 10^{20}$	–	$4.724 \cdot 10^{-12}$	–
EXOSAT-ME-PNT	–	bbody	1.0	$1 \cdot 10^{20}$	–	$1.139 \cdot 10^{-11}$	–
EXOSAT-ME-PNT	–	plaw	0.5	$3 \cdot 10^{20}$	–	$2.216 \cdot 10^{-11}$	–
EXOSAT-ME-PNT	–	plaw	1.0	$3 \cdot 10^{20}$	–	$1.869 \cdot 10^{-11}$	–
EXOSAT-ME-PNT	–	plaw	1.5	$3 \cdot 10^{20}$	–	$1.563 \cdot 10^{-11}$	–
EXOSAT-ME-PNT	–	plaw	1.7	$3 \cdot 10^{20}$	–	$1.455 \cdot 10^{-11}$	–
EXOSAT-ME-PNT	–	plaw	2.0	$3 \cdot 10^{20}$	–	$1.307 \cdot 10^{-11}$	–
EXOSAT-ME-PNT	–	plaw	2.5	$3 \cdot 10^{20}$	–	$1.098 \cdot 10^{-11}$	–
EXOSAT-ME-PNT	–	plaw	3.0	$3 \cdot 10^{20}$	–	$9.297 \cdot 10^{-12}$	–
EXOSAT-ME-PNT	–	plaw	3.5	$3 \cdot 10^{20}$	–	$7.928 \cdot 10^{-12}$	–
EXOSAT-ME-PNT	–	bbody	0.06	$3 \cdot 10^{20}$	–	$2.480 \cdot 10^{-16}$	–
EXOSAT-ME-PNT	–	bbody	0.1	$3 \cdot 10^{20}$	–	$7.277 \cdot 10^{-14}$	–
EXOSAT-ME-PNT	–	bbody	0.3	$3 \cdot 10^{20}$	–	$4.741 \cdot 10^{-12}$	–
EXOSAT-ME-PNT	–	bbody	1.0	$3 \cdot 10^{20}$	–	$1.140 \cdot 10^{-11}$	–
EXOSAT-ME-PNT	–	plaw	0.5	$1 \cdot 10^{21}$	–	$2.221 \cdot 10^{-11}$	–
EXOSAT-ME-PNT	–	plaw	1.0	$1 \cdot 10^{21}$	–	$1.875 \cdot 10^{-11}$	–
EXOSAT-ME-PNT	–	plaw	1.5	$1 \cdot 10^{21}$	–	$1.570 \cdot 10^{-11}$	–
EXOSAT-ME-PNT	–	plaw	1.7	$1 \cdot 10^{21}$	–	$1.462 \cdot 10^{-11}$	–
EXOSAT-ME-PNT	–	plaw	2.0	$1 \cdot 10^{21}$	–	$1.314 \cdot 10^{-11}$	–
EXOSAT-ME-PNT	–	plaw	2.5	$1 \cdot 10^{21}$	–	$1.105 \cdot 10^{-11}$	–
EXOSAT-ME-PNT	–	plaw	3.0	$1 \cdot 10^{21}$	–	$9.375 \cdot 10^{-12}$	–
EXOSAT-ME-PNT	–	plaw	3.5	$1 \cdot 10^{21}$	–	$8.008 \cdot 10^{-12}$	–
EXOSAT-ME-PNT	–	bbody	0.06	$1 \cdot 10^{21}$	–	$2.655 \cdot 10^{-16}$	–
EXOSAT-ME-PNT	–	bbody	0.1	$1 \cdot 10^{21}$	–	$7.609 \cdot 10^{-14}$	–
EXOSAT-ME-PNT	–	bbody	0.3	$1 \cdot 10^{21}$	–	$4.799 \cdot 10^{-12}$	–
EXOSAT-ME-PNT	–	bbody	1.0	$1 \cdot 10^{21}$	–	$1.143 \cdot 10^{-11}$	–
EPIC-pn	Thin1	plaw	0.5	$1 \cdot 10^{20}$	$1.496 \cdot 10^{-12}$	$1.524 \cdot 10^{-11}$	$9.588 \cdot 10^{-12}$
EPIC-pn	Thin1	plaw	1.0	$1 \cdot 10^{20}$	$1.375 \cdot 10^{-12}$	$1.231 \cdot 10^{-11}$	$5.688 \cdot 10^{-12}$
EPIC-pn	Thin1	plaw	1.5	$1 \cdot 10^{20}$	$1.251 \cdot 10^{-12}$	$9.994 \cdot 10^{-12}$	$3.199 \cdot 10^{-12}$
EPIC-pn	Thin1	plaw	1.7	$1 \cdot 10^{20}$	$1.203 \cdot 10^{-12}$	$9.231 \cdot 10^{-12}$	$2.563 \cdot 10^{-12}$
EPIC-pn	Thin1	plaw	2.0	$1 \cdot 10^{20}$	$1.136 \cdot 10^{-12}$	$8.244 \cdot 10^{-12}$	$1.900 \cdot 10^{-12}$
EPIC-pn	Thin1	plaw	2.5	$1 \cdot 10^{20}$	$1.037 \cdot 10^{-12}$	$6.962 \cdot 10^{-12}$	$1.309 \cdot 10^{-12}$
EPIC-pn	Thin1	plaw	3.0	$1 \cdot 10^{20}$	$9.586 \cdot 10^{-13}$	$6.039 \cdot 10^{-12}$	$1.050 \cdot 10^{-12}$
EPIC-pn	Thin1	plaw	3.5	$1 \cdot 10^{20}$	$8.993 \cdot 10^{-13}$	$5.379 \cdot 10^{-12}$	$9.291 \cdot 10^{-13}$
EPIC-pn	Thin1	bbody	0.06	$1 \cdot 10^{20}$	$8.448 \cdot 10^{-13}$	$2.594 \cdot 10^{-12}$	$8.449 \cdot 10^{-13}$
EPIC-pn	Thin1	bbody	0.1	$1 \cdot 10^{20}$	$9.379 \cdot 10^{-13}$	$2.762 \cdot 10^{-12}$	$9.379 \cdot 10^{-13}$
EPIC-pn	Thin1	bbody	0.3	$1 \cdot 10^{20}$	$1.321 \cdot 10^{-12}$	$3.720 \cdot 10^{-12}$	$1.409 \cdot 10^{-12}$
EPIC-pn	Thin1	bbody	1.0	$1 \cdot 10^{20}$	$1.674 \cdot 10^{-12}$	$6.803 \cdot 10^{-12}$	$4.392 \cdot 10^{-12}$
EPIC-pn	Thin1	plaw	0.5	$3 \cdot 10^{20}$	$1.533 \cdot 10^{-12}$	$1.525 \cdot 10^{-11}$	$9.853 \cdot 10^{-12}$
EPIC-pn	Thin1	plaw	1.0	$3 \cdot 10^{20}$	$1.424 \cdot 10^{-12}$	$1.232 \cdot 10^{-11}$	$6.010 \cdot 10^{-12}$
EPIC-pn	Thin1	plaw	1.5	$3 \cdot 10^{20}$	$1.314 \cdot 10^{-12}$	$1.000 \cdot 10^{-11}$	$3.501 \cdot 10^{-12}$
EPIC-pn	Thin1	plaw	1.7	$3 \cdot 10^{20}$	$1.271 \cdot 10^{-12}$	$9.240 \cdot 10^{-12}$	$2.840 \cdot 10^{-12}$
EPIC-pn	Thin1	plaw	2.0	$3 \cdot 10^{20}$	$1.208 \cdot 10^{-12}$	$8.253 \cdot 10^{-12}$	$2.133 \cdot 10^{-12}$
EPIC-pn	Thin1	plaw	2.5	$3 \cdot 10^{20}$	$1.115 \cdot 10^{-12}$	$6.969 \cdot 10^{-12}$	$1.474 \cdot 10^{-12}$
EPIC-pn	Thin1	plaw	3.0	$3 \cdot 10^{20}$	$1.037 \cdot 10^{-12}$	$6.045 \cdot 10^{-12}$	$1.169 \cdot 10^{-12}$
EPIC-pn	Thin1	plaw	3.5	$3 \cdot 10^{20}$	$9.753 \cdot 10^{-13}$	$5.384 \cdot 10^{-12}$	$1.023 \cdot 10^{-12}$
EPIC-pn	Thin1	bbody	0.06	$3 \cdot 10^{20}$	$8.925 \cdot 10^{-13}$	$2.594 \cdot 10^{-12}$	$8.927 \cdot 10^{-13}$
EPIC-pn	Thin1	bbody	0.1	$3 \cdot 10^{20}$	$9.716 \cdot 10^{-13}$	$2.763 \cdot 10^{-12}$	$9.716 \cdot 10^{-13}$
EPIC-pn	Thin1	bbody	0.3	$3 \cdot 10^{20}$	$1.347 \cdot 10^{-12}$	$3.722 \cdot 10^{-12}$	$1.442 \cdot 10^{-12}$
EPIC-pn	Thin1	bbody	1.0	$3 \cdot 10^{20}$	$1.691 \cdot 10^{-12}$	$6.808 \cdot 10^{-12}$	$4.446 \cdot 10^{-12}$
EPIC-pn	Thin1	plaw	0.5	$1 \cdot 10^{21}$	$1.607 \cdot 10^{-12}$	$1.529 \cdot 10^{-11}$	$1.044 \cdot 10^{-11}$
EPIC-pn	Thin1	plaw	1.0	$1 \cdot 10^{21}$	$1.516 \cdot 10^{-12}$	$1.235 \cdot 10^{-11}$	$6.680 \cdot 10^{-12}$
EPIC-pn	Thin1	plaw	1.5	$1 \cdot 10^{21}$	$1.422 \cdot 10^{-12}$	$1.004 \cdot 10^{-11}$	$4.119 \cdot 10^{-12}$
EPIC-pn	Thin1	plaw	1.7	$1 \cdot 10^{21}$	$1.385 \cdot 10^{-12}$	$9.272 \cdot 10^{-12}$	$3.408 \cdot 10^{-12}$
EPIC-pn	Thin1	plaw	2.0	$1 \cdot 10^{21}$	$1.331 \cdot 10^{-12}$	$8.282 \cdot 10^{-12}$	$2.615 \cdot 10^{-12}$
EPIC-pn	Thin1	plaw	2.5	$1 \cdot 10^{21}$	$1.246 \cdot 10^{-12}$	$6.993 \cdot 10^{-12}$	$1.821 \cdot 10^{-12}$
EPIC-pn	Thin1	plaw	3.0	$1 \cdot 10^{21}$	$1.172 \cdot 10^{-12}$	$6.065 \cdot 10^{-12}$	$1.421 \cdot 10^{-12}$
EPIC-pn	Thin1	plaw	3.5	$1 \cdot 10^{21}$	$1.112 \cdot 10^{-12}$	$5.400 \cdot 10^{-12}$	$1.217 \cdot 10^{-12}$
EPIC-pn	Thin1	bbody	0.06	$1 \cdot 10^{21}$	$9.587 \cdot 10^{-13}$	$2.594 \cdot 10^{-12}$	$9.587 \cdot 10^{-13}$
EPIC-pn	Thin1	bbody	0.1	$1 \cdot 10^{21}$	$1.015 \cdot 10^{-12}$	$2.764 \cdot 10^{-12}$	$1.015 \cdot 10^{-12}$

EPIC-pn	Thin1	bbody	0.3	$1 \cdot 10^{21}$	$1.407 \cdot 10^{-12}$	$3.727 \cdot 10^{-12}$	$1.520 \cdot 10^{-12}$
EPIC-pn	Thin1	bbody	1.0	$1 \cdot 10^{21}$	$1.734 \cdot 10^{-12}$	$6.823 \cdot 10^{-12}$	$4.597 \cdot 10^{-12}$
EPIC-pn	Medium	plaw	0.5	$1 \cdot 10^{20}$	$1.516 \cdot 10^{-12}$	$1.463 \cdot 10^{-11}$	$9.410 \cdot 10^{-12}$
EPIC-pn	Medium	plaw	1.0	$1 \cdot 10^{20}$	$1.420 \cdot 10^{-12}$	$1.186 \cdot 10^{-11}$	$5.713 \cdot 10^{-12}$
EPIC-pn	Medium	plaw	1.5	$1 \cdot 10^{20}$	$1.329 \cdot 10^{-12}$	$9.664 \cdot 10^{-12}$	$3.325 \cdot 10^{-12}$
EPIC-pn	Medium	plaw	1.7	$1 \cdot 10^{20}$	$1.295 \cdot 10^{-12}$	$8.939 \cdot 10^{-12}$	$2.708 \cdot 10^{-12}$
EPIC-pn	Medium	plaw	2.0	$1 \cdot 10^{20}$	$1.251 \cdot 10^{-12}$	$7.997 \cdot 10^{-12}$	$2.062 \cdot 10^{-12}$
EPIC-pn	Medium	plaw	2.5	$1 \cdot 10^{20}$	$1.192 \cdot 10^{-12}$	$6.772 \cdot 10^{-12}$	$1.492 \cdot 10^{-12}$
EPIC-pn	Medium	plaw	3.0	$1 \cdot 10^{20}$	$1.153 \cdot 10^{-12}$	$5.888 \cdot 10^{-12}$	$1.258 \cdot 10^{-12}$
EPIC-pn	Medium	plaw	3.5	$1 \cdot 10^{20}$	$1.131 \cdot 10^{-12}$	$5.255 \cdot 10^{-12}$	$1.167 \cdot 10^{-12}$
EPIC-pn	Medium	bbody	0.06	$1 \cdot 10^{20}$	$1.109 \cdot 10^{-12}$	$2.567 \cdot 10^{-12}$	$1.109 \cdot 10^{-12}$
EPIC-pn	Medium	bbody	0.1	$1 \cdot 10^{20}$	$1.088 \cdot 10^{-12}$	$2.730 \cdot 10^{-12}$	$1.088 \cdot 10^{-12}$
EPIC-pn	Medium	bbody	0.3	$1 \cdot 10^{20}$	$1.339 \cdot 10^{-12}$	$3.658 \cdot 10^{-12}$	$1.428 \cdot 10^{-12}$
EPIC-pn	Medium	bbody	1.0	$1 \cdot 10^{20}$	$1.664 \cdot 10^{-12}$	$6.603 \cdot 10^{-12}$	$4.311 \cdot 10^{-12}$
EPIC-pn	Medium	plaw	0.5	$3 \cdot 10^{20}$	$1.539 \cdot 10^{-12}$	$1.464 \cdot 10^{-11}$	$9.625 \cdot 10^{-12}$
EPIC-pn	Medium	plaw	1.0	$3 \cdot 10^{20}$	$1.447 \cdot 10^{-12}$	$1.187 \cdot 10^{-11}$	$5.968 \cdot 10^{-12}$
EPIC-pn	Medium	plaw	1.5	$3 \cdot 10^{20}$	$1.357 \cdot 10^{-12}$	$9.674 \cdot 10^{-12}$	$3.555 \cdot 10^{-12}$
EPIC-pn	Medium	plaw	1.7	$3 \cdot 10^{20}$	$1.324 \cdot 10^{-12}$	$8.947 \cdot 10^{-12}$	$2.915 \cdot 10^{-12}$
EPIC-pn	Medium	plaw	2.0	$3 \cdot 10^{20}$	$1.278 \cdot 10^{-12}$	$8.005 \cdot 10^{-12}$	$2.229 \cdot 10^{-12}$
EPIC-pn	Medium	plaw	2.5	$3 \cdot 10^{20}$	$1.214 \cdot 10^{-12}$	$6.778 \cdot 10^{-12}$	$1.593 \cdot 10^{-12}$
EPIC-pn	Medium	plaw	3.0	$3 \cdot 10^{20}$	$1.167 \cdot 10^{-12}$	$5.893 \cdot 10^{-12}$	$1.311 \cdot 10^{-12}$
EPIC-pn	Medium	plaw	3.5	$3 \cdot 10^{20}$	$1.137 \cdot 10^{-12}$	$5.259 \cdot 10^{-12}$	$1.190 \cdot 10^{-12}$
EPIC-pn	Medium	bbody	0.06	$3 \cdot 10^{20}$	$1.103 \cdot 10^{-12}$	$2.567 \cdot 10^{-12}$	$1.103 \cdot 10^{-12}$
EPIC-pn	Medium	bbody	0.1	$3 \cdot 10^{20}$	$1.081 \cdot 10^{-12}$	$2.730 \cdot 10^{-12}$	$1.081 \cdot 10^{-12}$
EPIC-pn	Medium	bbody	0.3	$3 \cdot 10^{20}$	$1.355 \cdot 10^{-12}$	$3.659 \cdot 10^{-12}$	$1.449 \cdot 10^{-12}$
EPIC-pn	Medium	bbody	1.0	$3 \cdot 10^{20}$	$1.678 \cdot 10^{-12}$	$6.607 \cdot 10^{-12}$	$4.359 \cdot 10^{-12}$
EPIC-pn	Medium	plaw	0.5	$1 \cdot 10^{21}$	$1.596 \cdot 10^{-12}$	$1.468 \cdot 10^{-11}$	$1.014 \cdot 10^{-11}$
EPIC-pn	Medium	plaw	1.0	$1 \cdot 10^{21}$	$1.512 \cdot 10^{-12}$	$1.190 \cdot 10^{-11}$	$6.554 \cdot 10^{-12}$
EPIC-pn	Medium	plaw	1.5	$1 \cdot 10^{21}$	$1.427 \cdot 10^{-12}$	$9.706 \cdot 10^{-12}$	$4.084 \cdot 10^{-12}$
EPIC-pn	Medium	plaw	1.7	$1 \cdot 10^{21}$	$1.394 \cdot 10^{-12}$	$8.978 \cdot 10^{-12}$	$3.396 \cdot 10^{-12}$
EPIC-pn	Medium	plaw	2.0	$1 \cdot 10^{21}$	$1.346 \cdot 10^{-12}$	$8.033 \cdot 10^{-12}$	$2.624 \cdot 10^{-12}$
EPIC-pn	Medium	plaw	2.5	$1 \cdot 10^{21}$	$1.274 \cdot 10^{-12}$	$6.801 \cdot 10^{-12}$	$1.852 \cdot 10^{-12}$
EPIC-pn	Medium	plaw	3.0	$1 \cdot 10^{21}$	$1.214 \cdot 10^{-12}$	$5.912 \cdot 10^{-12}$	$1.466 \cdot 10^{-12}$
EPIC-pn	Medium	plaw	3.5	$1 \cdot 10^{21}$	$1.167 \cdot 10^{-12}$	$5.275 \cdot 10^{-12}$	$1.275 \cdot 10^{-12}$
EPIC-pn	Medium	bbody	0.06	$1 \cdot 10^{21}$	$1.068 \cdot 10^{-12}$	$2.567 \cdot 10^{-12}$	$1.068 \cdot 10^{-12}$
EPIC-pn	Medium	bbody	0.1	$1 \cdot 10^{21}$	$1.068 \cdot 10^{-12}$	$2.731 \cdot 10^{-12}$	$1.068 \cdot 10^{-12}$
EPIC-pn	Medium	bbody	0.3	$1 \cdot 10^{21}$	$1.400 \cdot 10^{-12}$	$3.664 \cdot 10^{-12}$	$1.511 \cdot 10^{-12}$
EPIC-pn	Medium	bbody	1.0	$1 \cdot 10^{21}$	$1.715 \cdot 10^{-12}$	$6.621 \cdot 10^{-12}$	$4.499 \cdot 10^{-12}$
EPIC-pn	Thick	plaw	0.5	$1 \cdot 10^{20}$	$1.908 \cdot 10^{-12}$	$1.502 \cdot 10^{-11}$	$1.043 \cdot 10^{-11}$
EPIC-pn	Thick	plaw	1.0	$1 \cdot 10^{20}$	$1.864 \cdot 10^{-12}$	$1.224 \cdot 10^{-11}$	$6.747 \cdot 10^{-12}$
EPIC-pn	Thick	plaw	1.5	$1 \cdot 10^{20}$	$1.850 \cdot 10^{-12}$	$1.004 \cdot 10^{-11}$	$4.279 \cdot 10^{-12}$
EPIC-pn	Thick	plaw	1.7	$1 \cdot 10^{20}$	$1.856 \cdot 10^{-12}$	$9.305 \cdot 10^{-12}$	$3.627 \cdot 10^{-12}$
EPIC-pn	Thick	plaw	2.0	$1 \cdot 10^{20}$	$1.880 \cdot 10^{-12}$	$8.355 \cdot 10^{-12}$	$2.944 \cdot 10^{-12}$
EPIC-pn	Thick	plaw	2.5	$1 \cdot 10^{20}$	$1.964 \cdot 10^{-12}$	$7.115 \cdot 10^{-12}$	$2.386 \cdot 10^{-12}$
EPIC-pn	Thick	plaw	3.0	$1 \cdot 10^{20}$	$2.105 \cdot 10^{-12}$	$6.219 \cdot 10^{-12}$	$2.260 \cdot 10^{-12}$
EPIC-pn	Thick	plaw	3.5	$1 \cdot 10^{20}$	$2.296 \cdot 10^{-12}$	$5.577 \cdot 10^{-12}$	$2.349 \cdot 10^{-12}$
EPIC-pn	Thick	bbody	0.06	$1 \cdot 10^{20}$	$2.662 \cdot 10^{-12}$	$2.844 \cdot 10^{-12}$	$2.662 \cdot 10^{-12}$
EPIC-pn	Thick	bbody	0.1	$1 \cdot 10^{20}$	$1.926 \cdot 10^{-12}$	$3.012 \cdot 10^{-12}$	$1.926 \cdot 10^{-12}$
EPIC-pn	Thick	bbody	0.3	$1 \cdot 10^{20}$	$1.722 \cdot 10^{-12}$	$3.959 \cdot 10^{-12}$	$1.822 \cdot 10^{-12}$
EPIC-pn	Thick	bbody	1.0	$1 \cdot 10^{20}$	$1.998 \cdot 10^{-12}$	$6.882 \cdot 10^{-12}$	$4.786 \cdot 10^{-12}$
EPIC-pn	Thick	plaw	0.5	$3 \cdot 10^{20}$	$1.905 \cdot 10^{-12}$	$1.503 \cdot 10^{-11}$	$1.057 \cdot 10^{-11}$
EPIC-pn	Thick	plaw	1.0	$3 \cdot 10^{20}$	$1.846 \cdot 10^{-12}$	$1.225 \cdot 10^{-11}$	$6.908 \cdot 10^{-12}$
EPIC-pn	Thick	plaw	1.5	$3 \cdot 10^{20}$	$1.805 \cdot 10^{-12}$	$1.005 \cdot 10^{-11}$	$4.403 \cdot 10^{-12}$
EPIC-pn	Thick	plaw	1.7	$3 \cdot 10^{20}$	$1.797 \cdot 10^{-12}$	$9.314 \cdot 10^{-12}$	$3.721 \cdot 10^{-12}$
EPIC-pn	Thick	plaw	2.0	$3 \cdot 10^{20}$	$1.793 \cdot 10^{-12}$	$8.363 \cdot 10^{-12}$	$2.984 \cdot 10^{-12}$
EPIC-pn	Thick	plaw	2.5	$3 \cdot 10^{20}$	$1.819 \cdot 10^{-12}$	$7.121 \cdot 10^{-12}$	$2.319 \cdot 10^{-12}$
EPIC-pn	Thick	plaw	3.0	$3 \cdot 10^{20}$	$1.886 \cdot 10^{-12}$	$6.224 \cdot 10^{-12}$	$2.084 \cdot 10^{-12}$
EPIC-pn	Thick	plaw	3.5	$3 \cdot 10^{20}$	$1.994 \cdot 10^{-12}$	$5.581 \cdot 10^{-12}$	$2.069 \cdot 10^{-12}$
EPIC-pn	Thick	bbody	0.06	$3 \cdot 10^{20}$	$2.330 \cdot 10^{-12}$	$2.844 \cdot 10^{-12}$	$2.331 \cdot 10^{-12}$
EPIC-pn	Thick	bbody	0.1	$3 \cdot 10^{20}$	$1.774 \cdot 10^{-12}$	$3.012 \cdot 10^{-12}$	$1.774 \cdot 10^{-12}$
EPIC-pn	Thick	bbody	0.3	$3 \cdot 10^{20}$	$1.715 \cdot 10^{-12}$	$3.960 \cdot 10^{-12}$	$1.822 \cdot 10^{-12}$
EPIC-pn	Thick	bbody	1.0	$3 \cdot 10^{20}$	$2.005 \cdot 10^{-12}$	$6.886 \cdot 10^{-12}$	$4.824 \cdot 10^{-12}$
EPIC-pn	Thick	plaw	0.5	$1 \cdot 10^{21}$	$1.928 \cdot 10^{-12}$	$1.507 \cdot 10^{-11}$	$1.099 \cdot 10^{-11}$
EPIC-pn	Thick	plaw	1.0	$1 \cdot 10^{21}$	$1.857 \cdot 10^{-12}$	$1.229 \cdot 10^{-11}$	$7.370 \cdot 10^{-12}$
EPIC-pn	Thick	plaw	1.5	$1 \cdot 10^{21}$	$1.790 \cdot 10^{-12}$	$1.008 \cdot 10^{-11}$	$4.803 \cdot 10^{-12}$
EPIC-pn	Thick	plaw	1.7	$1 \cdot 10^{21}$	$1.766 \cdot 10^{-12}$	$9.344 \cdot 10^{-12}$	$4.069 \cdot 10^{-12}$
EPIC-pn	Thick	plaw	2.0	$1 \cdot 10^{21}$	$1.734 \cdot 10^{-12}$	$8.390 \cdot 10^{-12}$	$3.236 \cdot 10^{-12}$
EPIC-pn	Thick	plaw	2.5	$1 \cdot 10^{21}$	$1.693 \cdot 10^{-12}$	$7.144 \cdot 10^{-12}$	$2.395 \cdot 10^{-12}$
EPIC-pn	Thick	plaw	3.0	$1 \cdot 10^{21}$	$1.671 \cdot 10^{-12}$	$6.243 \cdot 10^{-12}$	$1.986 \cdot 10^{-12}$

EPIC-pn	Thick	plaw	3.5	$1 \cdot 10^{21}$	$1.670 \cdot 10^{-12}$	$5.597 \cdot 10^{-12}$	$1.808 \cdot 10^{-12}$
EPIC-pn	Thick	bbody	0.06	$1 \cdot 10^{21}$	$1.812 \cdot 10^{-12}$	$2.844 \cdot 10^{-12}$	$1.812 \cdot 10^{-12}$
EPIC-pn	Thick	bbody	0.1	$1 \cdot 10^{21}$	$1.569 \cdot 10^{-12}$	$3.013 \cdot 10^{-12}$	$1.569 \cdot 10^{-12}$
EPIC-pn	Thick	bbody	0.3	$1 \cdot 10^{21}$	$1.727 \cdot 10^{-12}$	$3.965 \cdot 10^{-12}$	$1.851 \cdot 10^{-12}$
EPIC-pn	Thick	bbody	1.0	$1 \cdot 10^{21}$	$2.032 \cdot 10^{-12}$	$6.900 \cdot 10^{-12}$	$4.945 \cdot 10^{-12}$
EINSTEIN	IPC	plaw	0.5	$1 \cdot 10^{20}$	$1.353 \cdot 10^{-11}$	–	–
EINSTEIN	IPC	plaw	1.0	$1 \cdot 10^{20}$	$1.557 \cdot 10^{-11}$	–	–
EINSTEIN	IPC	plaw	1.5	$1 \cdot 10^{20}$	$1.690 \cdot 10^{-11}$	–	–
EINSTEIN	IPC	plaw	1.7	$1 \cdot 10^{20}$	$1.707 \cdot 10^{-11}$	–	–
EINSTEIN	IPC	plaw	2.0	$1 \cdot 10^{20}$	$1.687 \cdot 10^{-11}$	–	–
EINSTEIN	IPC	plaw	2.5	$1 \cdot 10^{20}$	$1.536 \cdot 10^{-11}$	–	–
EINSTEIN	IPC	plaw	3.0	$1 \cdot 10^{20}$	$1.308 \cdot 10^{-11}$	–	–
EINSTEIN	IPC	plaw	3.5	$1 \cdot 10^{20}$	$1.081 \cdot 10^{-11}$	–	–
EINSTEIN	IPC	bbody	0.06	$1 \cdot 10^{20}$	$1.151 \cdot 10^{-11}$	–	–
EINSTEIN	IPC	bbody	0.1	$1 \cdot 10^{20}$	$2.040 \cdot 10^{-11}$	–	–
EINSTEIN	IPC	bbody	0.3	$1 \cdot 10^{20}$	$2.118 \cdot 10^{-11}$	–	–
EINSTEIN	IPC	bbody	1.0	$1 \cdot 10^{20}$	$1.232 \cdot 10^{-11}$	–	–
EINSTEIN	IPC	plaw	0.5	$3 \cdot 10^{20}$	$1.344 \cdot 10^{-11}$	–	–
EINSTEIN	IPC	plaw	1.0	$3 \cdot 10^{20}$	$1.577 \cdot 10^{-11}$	–	–
EINSTEIN	IPC	plaw	1.5	$3 \cdot 10^{20}$	$1.799 \cdot 10^{-11}$	–	–
EINSTEIN	IPC	plaw	1.7	$3 \cdot 10^{20}$	$1.876 \cdot 10^{-11}$	–	–
EINSTEIN	IPC	plaw	2.0	$3 \cdot 10^{20}$	$1.969 \cdot 10^{-11}$	–	–
EINSTEIN	IPC	plaw	2.5	$3 \cdot 10^{20}$	$2.038 \cdot 10^{-11}$	–	–
EINSTEIN	IPC	plaw	3.0	$3 \cdot 10^{20}$	$1.977 \cdot 10^{-11}$	–	–
EINSTEIN	IPC	plaw	3.5	$3 \cdot 10^{20}$	$1.811 \cdot 10^{-11}$	–	–
EINSTEIN	IPC	bbody	0.06	$3 \cdot 10^{20}$	$1.866 \cdot 10^{-11}$	–	–
EINSTEIN	IPC	bbody	0.1	$3 \cdot 10^{20}$	$2.767 \cdot 10^{-11}$	–	–
EINSTEIN	IPC	bbody	0.3	$3 \cdot 10^{20}$	$2.133 \cdot 10^{-11}$	–	–
EINSTEIN	IPC	bbody	1.0	$3 \cdot 10^{20}$	$1.220 \cdot 10^{-11}$	–	–
EINSTEIN	IPC	plaw	0.5	$1 \cdot 10^{21}$	$1.276 \cdot 10^{-11}$	–	–
EINSTEIN	IPC	plaw	1.0	$1 \cdot 10^{21}$	$1.495 \cdot 10^{-11}$	–	–
EINSTEIN	IPC	plaw	1.5	$1 \cdot 10^{21}$	$1.721 \cdot 10^{-11}$	–	–
EINSTEIN	IPC	plaw	1.7	$1 \cdot 10^{21}$	$1.814 \cdot 10^{-11}$	–	–
EINSTEIN	IPC	plaw	2.0	$1 \cdot 10^{21}$	$1.956 \cdot 10^{-11}$	–	–
EINSTEIN	IPC	plaw	2.5	$1 \cdot 10^{21}$	$2.200 \cdot 10^{-11}$	–	–
EINSTEIN	IPC	plaw	3.0	$1 \cdot 10^{21}$	$2.454 \cdot 10^{-11}$	–	–
EINSTEIN	IPC	plaw	3.5	$1 \cdot 10^{21}$	$2.710 \cdot 10^{-11}$	–	–
EINSTEIN	IPC	bbody	0.06	$1 \cdot 10^{21}$	$4.857 \cdot 10^{-11}$	–	–
EINSTEIN	IPC	bbody	0.1	$1 \cdot 10^{21}$	$3.304 \cdot 10^{-11}$	–	–
EINSTEIN	IPC	bbody	0.3	$1 \cdot 10^{21}$	$2.078 \cdot 10^{-11}$	–	–
EINSTEIN	IPC	bbody	1.0	$1 \cdot 10^{21}$	$1.180 \cdot 10^{-11}$	–	–
EINSTEIN	HRI	plaw	0.5	$1 \cdot 10^{20}$	$7.523 \cdot 10^{-11}$	–	–
EINSTEIN	HRI	plaw	1.0	$1 \cdot 10^{20}$	$6.841 \cdot 10^{-11}$	–	–
EINSTEIN	HRI	plaw	1.5	$1 \cdot 10^{20}$	$5.823 \cdot 10^{-11}$	–	–
EINSTEIN	HRI	plaw	1.7	$1 \cdot 10^{20}$	$5.382 \cdot 10^{-11}$	–	–
EINSTEIN	HRI	plaw	2.0	$1 \cdot 10^{20}$	$4.732 \cdot 10^{-11}$	–	–
EINSTEIN	HRI	plaw	2.5	$1 \cdot 10^{20}$	$3.761 \cdot 10^{-11}$	–	–
EINSTEIN	HRI	plaw	3.0	$1 \cdot 10^{20}$	$2.984 \cdot 10^{-11}$	–	–
EINSTEIN	HRI	plaw	3.5	$1 \cdot 10^{20}$	$2.394 \cdot 10^{-11}$	–	–
EINSTEIN	HRI	bbody	0.06	$1 \cdot 10^{20}$	$2.561 \cdot 10^{-11}$	–	–
EINSTEIN	HRI	bbody	0.1	$1 \cdot 10^{20}$	$3.867 \cdot 10^{-11}$	–	–
EINSTEIN	HRI	bbody	0.3	$1 \cdot 10^{20}$	$7.347 \cdot 10^{-11}$	–	–
EINSTEIN	HRI	bbody	1.0	$1 \cdot 10^{20}$	$8.799 \cdot 10^{-11}$	–	–
EINSTEIN	HRI	plaw	0.5	$3 \cdot 10^{20}$	$7.928 \cdot 10^{-11}$	–	–
EINSTEIN	HRI	plaw	1.0	$3 \cdot 10^{20}$	$7.561 \cdot 10^{-11}$	–	–
EINSTEIN	HRI	plaw	1.5	$3 \cdot 10^{20}$	$6.893 \cdot 10^{-11}$	–	–
EINSTEIN	HRI	plaw	1.7	$3 \cdot 10^{20}$	$6.584 \cdot 10^{-11}$	–	–
EINSTEIN	HRI	plaw	2.0	$3 \cdot 10^{20}$	$6.107 \cdot 10^{-11}$	–	–
EINSTEIN	HRI	plaw	2.5	$3 \cdot 10^{20}$	$5.335 \cdot 10^{-11}$	–	–
EINSTEIN	HRI	plaw	3.0	$3 \cdot 10^{20}$	$4.644 \cdot 10^{-11}$	–	–
EINSTEIN	HRI	plaw	3.5	$3 \cdot 10^{20}$	$4.048 \cdot 10^{-11}$	–	–
EINSTEIN	HRI	bbody	0.06	$3 \cdot 10^{20}$	$3.848 \cdot 10^{-11}$	–	–
EINSTEIN	HRI	bbody	0.1	$3 \cdot 10^{20}$	$4.682 \cdot 10^{-11}$	–	–
EINSTEIN	HRI	bbody	0.3	$3 \cdot 10^{20}$	$7.722 \cdot 10^{-11}$	–	–
EINSTEIN	HRI	bbody	1.0	$3 \cdot 10^{20}$	$8.915 \cdot 10^{-11}$	–	–
EINSTEIN	HRI	plaw	0.5	$1 \cdot 10^{21}$	$8.339 \cdot 10^{-11}$	–	–
EINSTEIN	HRI	plaw	1.0	$1 \cdot 10^{21}$	$8.237 \cdot 10^{-11}$	–	–
EINSTEIN	HRI	plaw	1.5	$1 \cdot 10^{21}$	$7.827 \cdot 10^{-11}$	–	–
EINSTEIN	HRI	plaw	1.7	$1 \cdot 10^{21}$	$7.614 \cdot 10^{-11}$	–	–

EINSTEIN	HRI	plaw	2.0	$1 \cdot 10^{21}$	$7.273 \cdot 10^{-11}$	–	–
EINSTEIN	HRI	plaw	2.5	$1 \cdot 10^{21}$	$6.719 \cdot 10^{-11}$	–	–
EINSTEIN	HRI	plaw	3.0	$1 \cdot 10^{21}$	$6.250 \cdot 10^{-11}$	–	–
EINSTEIN	HRI	plaw	3.5	$1 \cdot 10^{21}$	$5.898 \cdot 10^{-11}$	–	–
EINSTEIN	HRI	bbody	0.06	$1 \cdot 10^{21}$	$5.643 \cdot 10^{-11}$	–	–
EINSTEIN	HRI	bbody	0.1	$1 \cdot 10^{21}$	$5.001 \cdot 10^{-11}$	–	–
EINSTEIN	HRI	bbody	0.3	$1 \cdot 10^{21}$	$8.351 \cdot 10^{-11}$	–	–
EINSTEIN	HRI	bbody	1.0	$1 \cdot 10^{21}$	$9.099 \cdot 10^{-11}$	–	–
Swift-XRT	PC	plaw	0.5	$1 \cdot 10^{20}$	$2.262 \cdot 10^{-11}$	$1.754 \cdot 10^{-10}$	$1.224 \cdot 10^{-10}$
Swift-XRT	PC	plaw	1.0	$1 \cdot 10^{20}$	$2.314 \cdot 10^{-11}$	$1.343 \cdot 10^{-10}$	$7.887 \cdot 10^{-11}$
Swift-XRT	PC	plaw	1.5	$1 \cdot 10^{20}$	$2.429 \cdot 10^{-11}$	$1.049 \cdot 10^{-10}$	$5.223 \cdot 10^{-11}$
Swift-XRT	PC	plaw	1.7	$1 \cdot 10^{20}$	$2.500 \cdot 10^{-11}$	$9.575 \cdot 10^{-11}$	$4.551 \cdot 10^{-11}$
Swift-XRT	PC	plaw	2.0	$1 \cdot 10^{20}$	$2.638 \cdot 10^{-11}$	$8.433 \cdot 10^{-11}$	$3.883 \cdot 10^{-11}$
Swift-XRT	PC	plaw	2.5	$1 \cdot 10^{20}$	$2.974 \cdot 10^{-11}$	$7.017 \cdot 10^{-11}$	$3.460 \cdot 10^{-11}$
Swift-XRT	PC	plaw	3.0	$1 \cdot 10^{20}$	$3.471 \cdot 10^{-11}$	$6.048 \cdot 10^{-11}$	$3.631 \cdot 10^{-11}$
Swift-XRT	PC	plaw	3.5	$1 \cdot 10^{20}$	$4.161 \cdot 10^{-11}$	$5.383 \cdot 10^{-11}$	$4.198 \cdot 10^{-11}$
Swift-XRT	PC	bbody	0.06	$1 \cdot 10^{20}$	$5.643 \cdot 10^{-11}$	$2.984 \cdot 10^{-11}$	$5.643 \cdot 10^{-11}$
Swift-XRT	PC	bbody	0.1	$1 \cdot 10^{20}$	$3.283 \cdot 10^{-11}$	$3.104 \cdot 10^{-11}$	$3.283 \cdot 10^{-11}$
Swift-XRT	PC	bbody	0.3	$1 \cdot 10^{20}$	$2.189 \cdot 10^{-11}$	$3.848 \cdot 10^{-11}$	$2.286 \cdot 10^{-11}$
Swift-XRT	PC	bbody	1.0	$1 \cdot 10^{20}$	$2.231 \cdot 10^{-11}$	$6.632 \cdot 10^{-11}$	$4.900 \cdot 10^{-11}$
Swift-XRT	PC	plaw	0.5	$3 \cdot 10^{20}$	$2.232 \cdot 10^{-11}$	$1.755 \cdot 10^{-10}$	$1.236 \cdot 10^{-10}$
Swift-XRT	PC	plaw	1.0	$3 \cdot 10^{20}$	$2.252 \cdot 10^{-11}$	$1.344 \cdot 10^{-10}$	$7.991 \cdot 10^{-11}$
Swift-XRT	PC	plaw	1.5	$3 \cdot 10^{20}$	$2.309 \cdot 10^{-11}$	$1.050 \cdot 10^{-10}$	$5.261 \cdot 10^{-11}$
Swift-XRT	PC	plaw	1.7	$3 \cdot 10^{20}$	$2.346 \cdot 10^{-11}$	$9.585 \cdot 10^{-11}$	$4.546 \cdot 10^{-11}$
Swift-XRT	PC	plaw	2.0	$3 \cdot 10^{20}$	$2.420 \cdot 10^{-11}$	$8.442 \cdot 10^{-11}$	$3.794 \cdot 10^{-11}$
Swift-XRT	PC	plaw	2.5	$3 \cdot 10^{20}$	$2.600 \cdot 10^{-11}$	$7.024 \cdot 10^{-11}$	$3.181 \cdot 10^{-11}$
Swift-XRT	PC	plaw	3.0	$3 \cdot 10^{20}$	$2.865 \cdot 10^{-11}$	$6.053 \cdot 10^{-11}$	$3.087 \cdot 10^{-11}$
Swift-XRT	PC	plaw	3.5	$3 \cdot 10^{20}$	$3.231 \cdot 10^{-11}$	$5.387 \cdot 10^{-11}$	$3.305 \cdot 10^{-11}$
Swift-XRT	PC	bbody	0.06	$3 \cdot 10^{20}$	$4.312 \cdot 10^{-11}$	$2.984 \cdot 10^{-11}$	$4.313 \cdot 10^{-11}$
Swift-XRT	PC	bbody	0.1	$3 \cdot 10^{20}$	$2.899 \cdot 10^{-11}$	$3.105 \cdot 10^{-11}$	$2.899 \cdot 10^{-11}$
Swift-XRT	PC	bbody	0.3	$3 \cdot 10^{20}$	$2.156 \cdot 10^{-11}$	$3.849 \cdot 10^{-11}$	$2.259 \cdot 10^{-11}$
Swift-XRT	PC	bbody	1.0	$3 \cdot 10^{20}$	$2.227 \cdot 10^{-11}$	$6.636 \cdot 10^{-11}$	$4.925 \cdot 10^{-11}$
Swift-XRT	PC	plaw	0.5	$1 \cdot 10^{21}$	$2.204 \cdot 10^{-11}$	$1.761 \cdot 10^{-10}$	$1.275 \cdot 10^{-10}$
Swift-XRT	PC	plaw	1.0	$1 \cdot 10^{21}$	$2.191 \cdot 10^{-11}$	$1.349 \cdot 10^{-10}$	$8.365 \cdot 10^{-11}$
Swift-XRT	PC	plaw	1.5	$1 \cdot 10^{21}$	$2.192 \cdot 10^{-11}$	$1.054 \cdot 10^{-10}$	$5.536 \cdot 10^{-11}$
Swift-XRT	PC	plaw	1.7	$1 \cdot 10^{21}$	$2.197 \cdot 10^{-11}$	$9.621 \cdot 10^{-11}$	$4.760 \cdot 10^{-11}$
Swift-XRT	PC	plaw	2.0	$1 \cdot 10^{21}$	$2.210 \cdot 10^{-11}$	$8.472 \cdot 10^{-11}$	$3.894 \cdot 10^{-11}$
Swift-XRT	PC	plaw	2.5	$1 \cdot 10^{21}$	$2.250 \cdot 10^{-11}$	$7.048 \cdot 10^{-11}$	$3.047 \cdot 10^{-11}$
Swift-XRT	PC	plaw	3.0	$1 \cdot 10^{21}$	$2.313 \cdot 10^{-11}$	$6.072 \cdot 10^{-11}$	$2.672 \cdot 10^{-11}$
Swift-XRT	PC	plaw	3.5	$1 \cdot 10^{21}$	$2.401 \cdot 10^{-11}$	$5.402 \cdot 10^{-11}$	$2.556 \cdot 10^{-11}$
Swift-XRT	PC	bbody	0.06	$1 \cdot 10^{21}$	$2.912 \cdot 10^{-11}$	$2.984 \cdot 10^{-11}$	$2.912 \cdot 10^{-11}$
Swift-XRT	PC	bbody	0.1	$1 \cdot 10^{21}$	$2.463 \cdot 10^{-11}$	$3.105 \cdot 10^{-11}$	$2.463 \cdot 10^{-11}$
Swift-XRT	PC	bbody	0.3	$1 \cdot 10^{21}$	$2.113 \cdot 10^{-11}$	$3.853 \cdot 10^{-11}$	$2.233 \cdot 10^{-11}$
Swift-XRT	PC	bbody	1.0	$1 \cdot 10^{21}$	$2.227 \cdot 10^{-11}$	$6.650 \cdot 10^{-11}$	$5.009 \cdot 10^{-11}$
GINGA-LAC	Top	plaw	0.5	$1 \cdot 10^{20}$	–	$4.200 \cdot 10^{-12}$	–
GINGA-LAC	Top	plaw	1.0	$1 \cdot 10^{20}$	–	$3.586 \cdot 10^{-12}$	–
GINGA-LAC	Top	plaw	1.5	$1 \cdot 10^{20}$	–	$3.087 \cdot 10^{-12}$	–
GINGA-LAC	Top	plaw	1.7	$1 \cdot 10^{20}$	–	$2.917 \cdot 10^{-12}$	–
GINGA-LAC	Top	plaw	2.0	$1 \cdot 10^{20}$	–	$2.692 \cdot 10^{-12}$	–
GINGA-LAC	Top	plaw	2.5	$1 \cdot 10^{20}$	–	$2.386 \cdot 10^{-12}$	–
GINGA-LAC	Top	plaw	3.0	$1 \cdot 10^{20}$	–	$2.147 \cdot 10^{-12}$	–
GINGA-LAC	Top	plaw	3.5	$1 \cdot 10^{20}$	–	$1.956 \cdot 10^{-12}$	–
GINGA-LAC	Top	bbody	0.06	$1 \cdot 10^{20}$	–	$5.084 \cdot 10^{-16}$	–
GINGA-LAC	Top	bbody	0.1	$1 \cdot 10^{20}$	–	$6.192 \cdot 10^{-14}$	–
GINGA-LAC	Top	bbody	0.3	$1 \cdot 10^{20}$	–	$1.460 \cdot 10^{-12}$	–
GINGA-LAC	Top	bbody	1.0	$1 \cdot 10^{20}$	–	$2.258 \cdot 10^{-12}$	–
GINGA-LAC	Top	plaw	0.5	$3 \cdot 10^{20}$	–	$4.202 \cdot 10^{-12}$	–
GINGA-LAC	Top	plaw	1.0	$3 \cdot 10^{20}$	–	$3.588 \cdot 10^{-12}$	–
GINGA-LAC	Top	plaw	1.5	$3 \cdot 10^{20}$	–	$3.089 \cdot 10^{-12}$	–
GINGA-LAC	Top	plaw	1.7	$3 \cdot 10^{20}$	–	$2.919 \cdot 10^{-12}$	–
GINGA-LAC	Top	plaw	2.0	$3 \cdot 10^{20}$	–	$2.694 \cdot 10^{-12}$	–
GINGA-LAC	Top	plaw	2.5	$3 \cdot 10^{20}$	–	$2.388 \cdot 10^{-12}$	–
GINGA-LAC	Top	plaw	3.0	$3 \cdot 10^{20}$	–	$2.149 \cdot 10^{-12}$	–
GINGA-LAC	Top	plaw	3.5	$3 \cdot 10^{20}$	–	$1.958 \cdot 10^{-12}$	–
GINGA-LAC	Top	bbody	0.06	$3 \cdot 10^{20}$	–	$5.155 \cdot 10^{-16}$	–
GINGA-LAC	Top	bbody	0.1	$3 \cdot 10^{20}$	–	$6.245 \cdot 10^{-14}$	–
GINGA-LAC	Top	bbody	0.3	$3 \cdot 10^{20}$	–	$1.462 \cdot 10^{-12}$	–
GINGA-LAC	Top	bbody	1.0	$3 \cdot 10^{20}$	–	$2.258 \cdot 10^{-12}$	–
GINGA-LAC	Top	plaw	0.5	$1 \cdot 10^{21}$	–	$4.209 \cdot 10^{-12}$	–

GINGA-LAC	Top	plaw	1.0	$1 \cdot 10^{21}$	–	$3.595 \cdot 10^{-12}$	–
GINGA-LAC	Top	plaw	1.5	$1 \cdot 10^{21}$	–	$3.096 \cdot 10^{-12}$	–
GINGA-LAC	Top	plaw	1.7	$1 \cdot 10^{21}$	–	$2.926 \cdot 10^{-12}$	–
GINGA-LAC	Top	plaw	2.0	$1 \cdot 10^{21}$	–	$2.702 \cdot 10^{-12}$	–
GINGA-LAC	Top	plaw	2.5	$1 \cdot 10^{21}$	–	$2.395 \cdot 10^{-12}$	–
GINGA-LAC	Top	plaw	3.0	$1 \cdot 10^{21}$	–	$2.157 \cdot 10^{-12}$	–
GINGA-LAC	Top	plaw	3.5	$1 \cdot 10^{21}$	–	$1.967 \cdot 10^{-12}$	–
GINGA-LAC	Top	bbody	0.06	$1 \cdot 10^{21}$	–	$5.410 \cdot 10^{-16}$	–
GINGA-LAC	Top	bbody	0.1	$1 \cdot 10^{21}$	–	$6.433 \cdot 10^{-14}$	–
GINGA-LAC	Top	bbody	0.3	$1 \cdot 10^{21}$	–	$1.472 \cdot 10^{-12}$	–
GINGA-LAC	Top	bbody	1.0	$1 \cdot 10^{21}$	–	$2.261 \cdot 10^{-12}$	–
ASCA	SIS	plaw	0.5	$1 \cdot 10^{20}$	–	–	$1.058 \cdot 10^{-10}$
ASCA	SIS	plaw	1.0	$1 \cdot 10^{20}$	–	–	$6.898 \cdot 10^{-11}$
ASCA	SIS	plaw	1.5	$1 \cdot 10^{20}$	–	–	$4.778 \cdot 10^{-11}$
ASCA	SIS	plaw	1.7	$1 \cdot 10^{20}$	–	–	$4.285 \cdot 10^{-11}$
ASCA	SIS	plaw	2.0	$1 \cdot 10^{20}$	–	–	$3.864 \cdot 10^{-11}$
ASCA	SIS	plaw	2.5	$1 \cdot 10^{20}$	–	–	$3.887 \cdot 10^{-11}$
ASCA	SIS	plaw	3.0	$1 \cdot 10^{20}$	–	–	$4.730 \cdot 10^{-11}$
ASCA	SIS	plaw	3.5	$1 \cdot 10^{20}$	–	–	$6.440 \cdot 10^{-11}$
ASCA	SIS	bbody	0.06	$1 \cdot 10^{20}$	–	–	$1.833 \cdot 10^{-10}$
ASCA	SIS	bbody	0.1	$1 \cdot 10^{20}$	–	–	$6.461 \cdot 10^{-11}$
ASCA	SIS	bbody	0.3	$1 \cdot 10^{20}$	–	–	$2.022 \cdot 10^{-11}$
ASCA	SIS	bbody	1.0	$1 \cdot 10^{20}$	–	–	$4.026 \cdot 10^{-11}$
ASCA	SIS	plaw	0.5	$3 \cdot 10^{20}$	–	–	$1.064 \cdot 10^{-10}$
ASCA	SIS	plaw	1.0	$3 \cdot 10^{20}$	–	–	$6.927 \cdot 10^{-11}$
ASCA	SIS	plaw	1.5	$3 \cdot 10^{20}$	–	–	$4.727 \cdot 10^{-11}$
ASCA	SIS	plaw	1.7	$3 \cdot 10^{20}$	–	–	$4.185 \cdot 10^{-11}$
ASCA	SIS	plaw	2.0	$3 \cdot 10^{20}$	–	–	$3.663 \cdot 10^{-11}$
ASCA	SIS	plaw	2.5	$3 \cdot 10^{20}$	–	–	$3.414 \cdot 10^{-11}$
ASCA	SIS	plaw	3.0	$3 \cdot 10^{20}$	–	–	$3.786 \cdot 10^{-11}$
ASCA	SIS	plaw	3.5	$3 \cdot 10^{20}$	–	–	$4.707 \cdot 10^{-11}$
ASCA	SIS	bbody	0.06	$3 \cdot 10^{20}$	–	–	$1.291 \cdot 10^{-10}$
ASCA	SIS	bbody	0.1	$3 \cdot 10^{20}$	–	–	$5.401 \cdot 10^{-11}$
ASCA	SIS	bbody	0.3	$3 \cdot 10^{20}$	–	–	$1.968 \cdot 10^{-11}$
ASCA	SIS	bbody	1.0	$3 \cdot 10^{20}$	–	–	$4.040 \cdot 10^{-11}$
ASCA	SIS	plaw	0.5	$1 \cdot 10^{21}$	–	–	$1.089 \cdot 10^{-10}$
ASCA	SIS	plaw	1.0	$1 \cdot 10^{21}$	–	–	$7.106 \cdot 10^{-11}$
ASCA	SIS	plaw	1.5	$1 \cdot 10^{21}$	–	–	$4.774 \cdot 10^{-11}$
ASCA	SIS	plaw	1.7	$1 \cdot 10^{21}$	–	–	$4.159 \cdot 10^{-11}$
ASCA	SIS	plaw	2.0	$1 \cdot 10^{21}$	–	–	$3.500 \cdot 10^{-11}$
ASCA	SIS	plaw	2.5	$1 \cdot 10^{21}$	–	–	$2.933 \cdot 10^{-11}$
ASCA	SIS	plaw	3.0	$1 \cdot 10^{21}$	–	–	$2.823 \cdot 10^{-11}$
ASCA	SIS	plaw	3.5	$1 \cdot 10^{21}$	–	–	$3.017 \cdot 10^{-11}$
ASCA	SIS	bbody	0.06	$1 \cdot 10^{21}$	–	–	$7.002 \cdot 10^{-11}$
ASCA	SIS	bbody	0.1	$1 \cdot 10^{21}$	–	–	$3.969 \cdot 10^{-11}$
ASCA	SIS	bbody	0.3	$1 \cdot 10^{21}$	–	–	$1.868 \cdot 10^{-11}$
ASCA	SIS	bbody	1.0	$1 \cdot 10^{21}$	–	–	$4.095 \cdot 10^{-11}$
ASCA	GIS	plaw	0.5	$1 \cdot 10^{20}$	$5.850 \cdot 10^{-12}$	$8.537 \cdot 10^{-11}$	$9.122 \cdot 10^{-11}$
ASCA	GIS	plaw	1.0	$1 \cdot 10^{20}$	$1.012 \cdot 10^{-11}$	$5.907 \cdot 10^{-11}$	$6.919 \cdot 10^{-11}$
ASCA	GIS	plaw	1.5	$1 \cdot 10^{20}$	$1.717 \cdot 10^{-11}$	$3.932 \cdot 10^{-11}$	$5.648 \cdot 10^{-11}$
ASCA	GIS	plaw	1.7	$1 \cdot 10^{20}$	$2.119 \cdot 10^{-11}$	$3.314 \cdot 10^{-11}$	$5.432 \cdot 10^{-11}$
ASCA	GIS	plaw	2.0	$1 \cdot 10^{20}$	$2.915 \cdot 10^{-11}$	$2.549 \cdot 10^{-11}$	$5.464 \cdot 10^{-11}$
ASCA	GIS	plaw	2.5	$1 \cdot 10^{20}$	$5.055 \cdot 10^{-11}$	$1.632 \cdot 10^{-11}$	$6.688 \cdot 10^{-11}$
ASCA	GIS	plaw	3.0	$1 \cdot 10^{20}$	$9.057 \cdot 10^{-11}$	$1.044 \cdot 10^{-11}$	$1.010 \cdot 10^{-10}$
ASCA	GIS	plaw	3.5	$1 \cdot 10^{20}$	$1.677 \cdot 10^{-10}$	$6.701 \cdot 10^{-12}$	$1.744 \cdot 10^{-10}$
ASCA	GIS	bbody	0.06	$1 \cdot 10^{20}$	$1.143 \cdot 10^{-8}$	$6.090 \cdot 10^{-19}$	$1.143 \cdot 10^{-8}$
ASCA	GIS	bbody	0.1	$1 \cdot 10^{20}$	$5.757 \cdot 10^{-10}$	$2.491 \cdot 10^{-15}$	$5.758 \cdot 10^{-10}$
ASCA	GIS	bbody	0.3	$1 \cdot 10^{20}$	$3.030 \cdot 10^{-11}$	$3.275 \cdot 10^{-12}$	$3.358 \cdot 10^{-11}$
ASCA	GIS	bbody	1.0	$1 \cdot 10^{20}$	$7.099 \cdot 10^{-12}$	$3.252 \cdot 10^{-11}$	$3.962 \cdot 10^{-11}$
ASCA	GIS	plaw	0.5	$3 \cdot 10^{20}$	$5.586 \cdot 10^{-12}$	$8.570 \cdot 10^{-11}$	$9.128 \cdot 10^{-11}$
ASCA	GIS	plaw	1.0	$3 \cdot 10^{20}$	$9.450 \cdot 10^{-12}$	$5.941 \cdot 10^{-11}$	$6.886 \cdot 10^{-11}$
ASCA	GIS	plaw	1.5	$3 \cdot 10^{20}$	$1.547 \cdot 10^{-11}$	$3.963 \cdot 10^{-11}$	$5.510 \cdot 10^{-11}$
ASCA	GIS	plaw	1.7	$3 \cdot 10^{20}$	$1.875 \cdot 10^{-11}$	$3.343 \cdot 10^{-11}$	$5.218 \cdot 10^{-11}$
ASCA	GIS	plaw	2.0	$3 \cdot 10^{20}$	$2.497 \cdot 10^{-11}$	$2.576 \cdot 10^{-11}$	$5.073 \cdot 10^{-11}$
ASCA	GIS	plaw	2.5	$3 \cdot 10^{20}$	$4.051 \cdot 10^{-11}$	$1.654 \cdot 10^{-11}$	$5.706 \cdot 10^{-11}$
ASCA	GIS	plaw	3.0	$3 \cdot 10^{20}$	$6.712 \cdot 10^{-11}$	$1.061 \cdot 10^{-11}$	$7.773 \cdot 10^{-11}$
ASCA	GIS	plaw	3.5	$3 \cdot 10^{20}$	$1.144 \cdot 10^{-10}$	$6.829 \cdot 10^{-12}$	$1.212 \cdot 10^{-10}$
ASCA	GIS	bbody	0.06	$3 \cdot 10^{20}$	$7.305 \cdot 10^{-9}$	$6.488 \cdot 10^{-19}$	$7.307 \cdot 10^{-9}$
ASCA	GIS	bbody	0.1	$3 \cdot 10^{20}$	$4.510 \cdot 10^{-10}$	$2.595 \cdot 10^{-15}$	$4.510 \cdot 10^{-10}$

Mission	Filter	Model	Index	N_H [cm^{-2}]			
ASCA	GIS	bbody	0.3	$3 \cdot 10^{20}$	$2.890 \cdot 10^{-11}$	$3.322 \cdot 10^{-12}$	$3.222 \cdot 10^{-11}$
ASCA	GIS	bbody	1.0	$3 \cdot 10^{20}$	$6.952 \cdot 10^{-12}$	$3.266 \cdot 10^{-11}$	$3.962 \cdot 10^{-11}$
ASCA	GIS	plaw	0.5	$1 \cdot 10^{21}$	$5.004 \cdot 10^{-12}$	$8.680 \cdot 10^{-12}$	$9.181 \cdot 10^{-11}$
ASCA	GIS	plaw	1.0	$1 \cdot 10^{21}$	$8.162 \cdot 10^{-12}$	$6.055 \cdot 10^{-11}$	$6.871 \cdot 10^{-11}$
ASCA	GIS	plaw	1.5	$1 \cdot 10^{21}$	$1.266 \cdot 10^{-11}$	$4.071 \cdot 10^{-11}$	$5.337 \cdot 10^{-11}$
ASCA	GIS	plaw	1.7	$1 \cdot 10^{21}$	$1.492 \cdot 10^{-11}$	$3.446 \cdot 10^{-11}$	$4.939 \cdot 10^{-11}$
ASCA	GIS	plaw	2.0	$1 \cdot 10^{21}$	$1.892 \cdot 10^{-11}$	$2.669 \cdot 10^{-11}$	$4.561 \cdot 10^{-11}$
ASCA	GIS	plaw	2.5	$1 \cdot 10^{21}$	$2.772 \cdot 10^{-11}$	$1.730 \cdot 10^{-11}$	$4.502 \cdot 10^{-11}$
ASCA	GIS	plaw	3.0	$1 \cdot 10^{21}$	$4.049 \cdot 10^{-11}$	$1.120 \cdot 10^{-11}$	$5.170 \cdot 10^{-11}$
ASCA	GIS	plaw	3.5	$1 \cdot 10^{21}$	$5.969 \cdot 10^{-11}$	$7.277 \cdot 10^{-12}$	$6.697 \cdot 10^{-11}$
ASCA	GIS	bbody	0.06	$1 \cdot 10^{21}$	$2.904 \cdot 10^{-9}$	$8.057 \cdot 10^{-19}$	$2.904 \cdot 10^{-9}$
ASCA	GIS	bbody	0.1	$1 \cdot 10^{21}$	$2.708 \cdot 10^{-10}$	$2.983 \cdot 10^{-15}$	$2.708 \cdot 10^{-10}$
ASCA	GIS	bbody	0.3	$1 \cdot 10^{21}$	$2.582 \cdot 10^{-11}$	$3.487 \cdot 10^{-12}$	$2.931 \cdot 10^{-11}$
ASCA	GIS	bbody	1.0	$1 \cdot 10^{21}$	$6.547 \cdot 10^{-12}$	$3.314 \cdot 10^{-11}$	$3.969 \cdot 10^{-11}$
HEAO-1-A2	–	bbody	0.06	$1 \cdot 10^{20}$	$(10.27 \pm 2.05) \times 10^{-11}$	(1.00 ± 0.20)	-
HEAO-1-A2	–	bbody	0.06	$3 \cdot 10^{20}$	$(9.33 \pm 1.87) \times 10^{-11}$	(1.00 ± 0.20)	-
HEAO-1-A2	–	bbody	0.06	$10 \cdot 10^{20}$	$(4.62 \pm 0.92) \times 10^{-11}$	(1.00 ± 0.20)	-
HEAO-1-A2	–	bbody	0.10	$1 \cdot 10^{20}$	$(4.32 \pm 0.86) \times 10^{-11}$	(1.00 ± 0.20)	-
HEAO-1-A2	–	bbody	0.10	$3 \cdot 10^{20}$	$(3.60 \pm 0.72) \times 10^{-11}$	(1.00 ± 0.20)	-
HEAO-1-A2	–	bbody	0.10	$10 \cdot 10^{20}$	$(2.66 \pm 0.53) \times 10^{-11}$	(1.00 ± 0.20)	-
HEAO-1-A2	–	bbody	0.30	$1 \cdot 10^{20}$	$(2.21 \pm 0.44) \times 10^{-11}$	(1.00 ± 0.20)	-
HEAO-1-A2	–	bbody	0.30	$3 \cdot 10^{20}$	$(2.87 \pm 0.57) \times 10^{-11}$	(1.00 ± 0.20)	-
HEAO-1-A2	–	bbody	0.30	$10 \cdot 10^{20}$	$(2.29 \pm 0.46) \times 10^{-11}$	(1.00 ± 0.20)	-
HEAO-1-A2	–	bbody	1.00	$1 \cdot 10^{20}$	$(2.85 \pm 0.57) \times 10^{-11}$	(1.01 ± 0.20)	-
HEAO-1-A2	–	bbody	1.00	$3 \cdot 10^{20}$	$(2.92 \pm 0.58) \times 10^{-11}$	(1.01 ± 0.20)	-
HEAO-1-A2	–	bbody	1.00	$10 \cdot 10^{20}$	$(2.96 \pm 0.59) \times 10^{-11}$	(1.01 ± 0.20)	-
HEAO-1-A2	–	plaw	1.00	$10 \cdot 10^{20}$	$(2.56 \pm 0.51) \times 10^{-11}$	(1.25 ± 0.25)	-
HEAO-1-A2	–	plaw	1.50	$1 \cdot 10^{20}$	$(2.61 \pm 0.52) \times 10^{-11}$	(1.17 ± 0.23)	-
HEAO-1-A2	–	plaw	1.50	$3 \cdot 10^{20}$	$(2.42 \pm 0.48) \times 10^{-11}$	(1.17 ± 0.23)	-
HEAO-1-A2	–	plaw	1.50	$10 \cdot 10^{20}$	$(2.21 \pm 0.44) \times 10^{-11}$	(1.17 ± 0.23)	-
HEAO-1-A2	–	plaw	1.70	$1 \cdot 10^{20}$	$(2.56 \pm 0.51) \times 10^{-11}$	(1.15 ± 0.23)	-
HEAO-1-A2	–	plaw	1.70	$3 \cdot 10^{20}$	$(2.33 \pm 0.47) \times 10^{-11}$	(1.15 ± 0.23)	-
HEAO-1-A2	–	plaw	1.70	$10 \cdot 10^{20}$	$(2.10 \pm 0.42) \times 10^{-11}$	(1.15 ± 0.23)	-
HEAO-1-A2	–	plaw	2.00	$1 \cdot 10^{20}$	$(2.83 \pm 0.57) \times 10^{-11}$	(1.11 ± 0.22)	-
HEAO-1-A2	–	plaw	2.00	$3 \cdot 10^{20}$	$(2.51 \pm 0.50) \times 10^{-11}$	(1.11 ± 0.22)	-
HEAO-1-A2	–	plaw	2.00	$10 \cdot 10^{20}$	$(2.10 \pm 0.42) \times 10^{-11}$	(1.11 ± 0.22)	-
HEAO-1-A2	–	plaw	2.50	$1 \cdot 10^{20}$	$(2.78 \pm 0.56) \times 10^{-11}$	(1.07 ± 0.21)	-
HEAO-1-A2	–	plaw	2.50	$3 \cdot 10^{20}$	$(2.33 \pm 0.47) \times 10^{-11}$	(1.07 ± 0.21)	-
HEAO-1-A2	–	plaw	2.50	$10 \cdot 10^{20}$	$(2.29 \pm 0.46) \times 10^{-11}$	(1.07 ± 0.21)	-
HEAO-1-A2	–	plaw	3.00	$1 \cdot 10^{20}$	$(3.52 \pm 0.70) \times 10^{-11}$	(1.04 ± 0.21)	-
HEAO-1-A2	–	plaw	3.00	$3 \cdot 10^{20}$	$(2.74 \pm 0.55) \times 10^{-11}$	(1.04 ± 0.21)	-
HEAO-1-A2	–	plaw	3.00	$10 \cdot 10^{20}$	$(2.15 \pm 0.43) \times 10^{-11}$	(1.04 ± 0.21)	-
HEAO-1-A2	–	plaw	3.50	$1 \cdot 10^{20}$	$(4.54 \pm 0.91) \times 10^{-11}$	(1.02 ± 0.20)	-
HEAO-1-A2	–	plaw	3.50	$3 \cdot 10^{20}$	$(3.29 \pm 0.66) \times 10^{-11}$	(1.02 ± 0.20)	-
HEAO-1-A2	–	plaw	3.50	$10 \cdot 10^{20}$	$(2.44 \pm 0.49) \times 10^{-11}$	(1.02 ± 0.20)	-
HEAO-1-A1	–	plaw	2.1	$1 \cdot 10^{20}$	-	$(5.28 \pm 1.06) \times 10^{-9}$	-
HEAO-1-A1	–	plaw	2.1	$3 \cdot 10^{20}$	-	$(5.28 \pm 1.06) \times 10^{-9}$	-
HEAO-1-A1	–	plaw	2.1	$1 \cdot 10^{21}$	-	$(5.28 \pm 1.06) \times 10^{-9}$	-
Vela5B	–	plaw	2.1	1×10^{20}	-	$(5.94 \pm 1.50) \times 10^{-10}$	-
Vela5B	–	plaw	2.1	3×10^{20}	-	$(5.93 \pm 1.50) \times 10^{-10}$	-
Vela5B	–	plaw	2.1	1×10^{21}	-	$(5.92 \pm 1.50) \times 10^{-10}$	-
Uhuru	–	plaw	2.1	1×10^{20}	-	$(2.68 \pm 0.54) \times 10^{-11}$	-
Uhuru	–	plaw	2.1	3×10^{20}	-	$(2.68 \pm 0.54) \times 10^{-11}$	-
Uhuru	–	plaw	2.1	1×10^{21}	-	$(2.69 \pm 0.54) \times 10^{-11}$	-
Ariel V	ASM	plaw	2.1	1×10^{20}	-	$(1787.5 \pm 0.9) \times 10^{-11}$	-
Ariel V	ASM	plaw	2.1	3×10^{20}	-	$(1788.6 \pm 0.9) \times 10^{-11}$	-
Ariel V	ASM	plaw	2.1	1×10^{21}	-	$(1792.5 \pm 0.9) \times 10^{-11}$	-
Ariel V	SSI	plaw	2.1	1×10^{20}	-	$(5.85 \pm 0.88) \times 10^{-11}$	-
Ariel V	SSI	plaw	2.1	3×10^{20}	-	$(5.85 \pm 0.88) \times 10^{-11}$	-
Ariel V	SSI	plaw	2.1	1×10^{21}	-	$(5.86 \pm 0.88) \times 10^{-11}$	-

Table A.4: Conversion factors (CFs) for *INTEGRAL* computed for an unabsorbed powerlaw (plaw) using the OSA 10 software.

Mission	Filter	Model	Index	N_H [cm^{-2}]	CF 20–40 keV	CF 40–60 keV	CF 60–100 keV
INTEGRAL	–	plaw	1.5	–	$5.959 \cdot 10^{-11}$	$1.411 \cdot 10^{-11}$	$2.237 \cdot 10^{-11}$
INTEGRAL	–	plaw	2.0	–	$1.844 \cdot 10^{-11}$	$1.29 \cdot 10^{-11}$	$1.624 \cdot 10^{-11}$
INTEGRAL	–	plaw	2.5	–	$2.583 \cdot 10^{-11}$	$1.068 \cdot 10^{-11}$	$1.116 \cdot 10^{-11}$

| INTEGRAL | – | plaw | 3.0 | – | $2.024 \cdot 10^{-11}$ | $8.36 \cdot 10^{-12}$ | $6.34 \cdot 10^{-12}$ |
| INTEGRAL | – | plaw | 3.5 | – | $1.115 \cdot 10^{-11}$ | $3.73 \cdot 10^{-12}$ | $3.61 \cdot 10^{-12}$ |